Probing Reaction Dynamics in Complex Gas-Phase Systems Using Guided-Ion-Beam Scattering and Computational Methods

by

Yigang Fang

A dissertation submitted to the Graduate Faculty in Chemistry
in partial fulfillment of the requirements
for the degree of Doctor of Philosophy,
The City University of New York.
2013

This manuscript has been read and accepted by the Graduate Faculty in Chemistry in satisfaction of the dissertation requirement for the degree of Doctor of Philosophy.

Date	Dr. Jianbo Liu Chair of Examining Committee
Date	Dr. Maria Tamargo Executive Officer

Dr. John R. Lombardi

Dr. Cherice M. Evans
Supervisory Committee

THE CITY UNIVERSITY OF NEW YORK

Abstract

Probing Reaction Dynamics in Complex Gas-Phase Systems Using Guided-Ion-Beam Scattering and Computational Methods

by

Yigang Fang

Advisor: Dr. Jianbo Liu

An electrospray ionization (ESI) guided-ion-beam tandem mass spectrometer was developed in our research lab, including vacuum systems, electronics and instrument control and data acquisition (DAQ) systems using LabVIEW programming. Capitalizing on this instrument, two experimental projects have been accomplished as described below.

In project 1, formation and characterization of multiply positively and negatively charged sodium bis(2-ethylhexyl)sulfosuccinate (NaAOT) aggregates were studied in the gas phase. Mass spectra show the compositions of $[(\text{NaAOT})_n\text{Na}_z]^{z+}$ for positively charged aggregates and $[\text{Na}_{n-z}\text{AOT}_n]^{z-}$ for negatively charged aggregates, with various aggregation numbers (n) and charges (z). Collision-induced dissociation (CID) of mass-selected micellar ions with Xe was performed to probe structures of gas-phase micellar assemblies, identify effects of charge states, solute-surfactant interactions, and determine preferential incorporation sites of different amino acids. Gas-phase NaAOT surfactants are able to assemble into a reverse micelle-like structure in positive ion mode and a direct micelle-like structure in negative ion mode, respectively. Both direct and reverse micelles are able to incorporate amino acids. Driving forces for amino acid solubilization in gas-phase micelles

come from hydrophobic and/or electrostatic interactions, which strongly depend on amino acid hydrophobicity and charge states.

In project 2, the reaction of deprotonated cysteine ([Cys-H]$^-$) with singlet molecular oxygen ($O_2[a^1\Delta_g]$) has been studied, including the measurement of effects of collision energy (E_{col}) on reaction cross sections. [Cys-H]$^-$ has a carboxylate anionic structure ($HSCH_2CH(NH_2)CO_2^-$) in the gas phase. Density functional theory (DFT) calculations were employed to examine the properties of various complexes, transition states and products. Three product channels were observed, corresponding to the formation of $NH_2CH_2CO_2^-$ with remaining neutral products, $OSCH_2CH(NH_2)CO_2^-$ via elimination of OH from an intermediate complex, and $HSCH_2C(NH)CO_2^-$ + H_2O_2 via abstraction of two hydrogen atoms from $HSCH_2CH(NH_2)CO_2^-$ by $^1O_2$, respectively. Quasi-classical direct dynamics trajectory simulations were carried out at E_{col} = 0.2 eV using B3LYP/4-31G(d) level of theory. Trajectory results were used to guide the construction of the reaction coordinate, discriminate between different mechanisms, and provide additional mechanistic insights. Analysis of trajectories highlights the importance of complex mediation at the early stage of all reactions, and suggests a partially concerted mechanism for the H_2O_2 elimination reaction.

Dedicated to my parents, my wife and my daughter

Acknowledgements

First and foremost, I owe my most sincere thanks to my advisor and mentor, Dr. Jianbo Liu, for his supervision, guidance and support throughout this work. In my graduate study, he has always been a kind and helpful mentor, giving me many generous help and valuable support, both in project design and in reviewing my reports and papers. His enthusiasm and persistence to science has influenced and helped me devoting to become a competitive researcher.

I want to thank my dissertation committee members, Dr. John Lombardi and Dr. Cherice Evans, for many invaluable discussions and suggestions on my research and career development.

In addition, I would like to thank all my coworkers and colleagues in Liu lab for their assistance and help. Particularly I would like to thank Fangwei Liu, Yun Chen and Andrew Bennett for their constant help and stimulating discussions in my experimental and theoretical work.

This work would not have been possible without the financial supports from the American Chemical Society Petroleum Research Fund, CUNY Collaborative Grant, PSC-CUNY Research awards, Queens College Research Enhancement Funds and the National Science Foundation CAREER Award. I also must acknowledge the Graduate Center of CUNY for awarding me a Doctoral Student Research Grant, Research Excellence Awards and travel grants to support this work.

Finally, special thanks to my wife and best friend, Dr. Chunling Wang. During the past years, she has been giving me consistent encouragement, advice and support. I am deeply grateful to my parents, my mother-in-law and my younger sister in China for their love and

being supportive of my seemingly unending graduate career. I would not be here without their support.

Table of Contents

Chapters

List of Tables

List of Figures

FIGURE PAGE

Chapter 1

ESI Guided-Ion-Beam Tandem Mass Spectrometer

1.1 Introduction

An electrospray ionization (ESI) guided-ion-beam tandem mass spectrometer was developed in our research lab for performing gas-phase ion-molecule reactions. The apparatus, as shown in Figure 1.1, can be divided into five sections: (1) ion source; (2) hexapole ion guide;[1] (3) quadrupole mass filter; (4) octopole ion guide and scattering cell; and (5) second quadrupole mass filter and detector. Briefly, ions are generated in an ESI source, thermalized in a hexapole ion guide and mass-selected using a quadrupole mass filter, and then interact with neutral reactant gas in an octopole ion guide. Ionic reactants and products are collected by the octopole and mass analyzed by a second quadrupole mass filter, and detected.

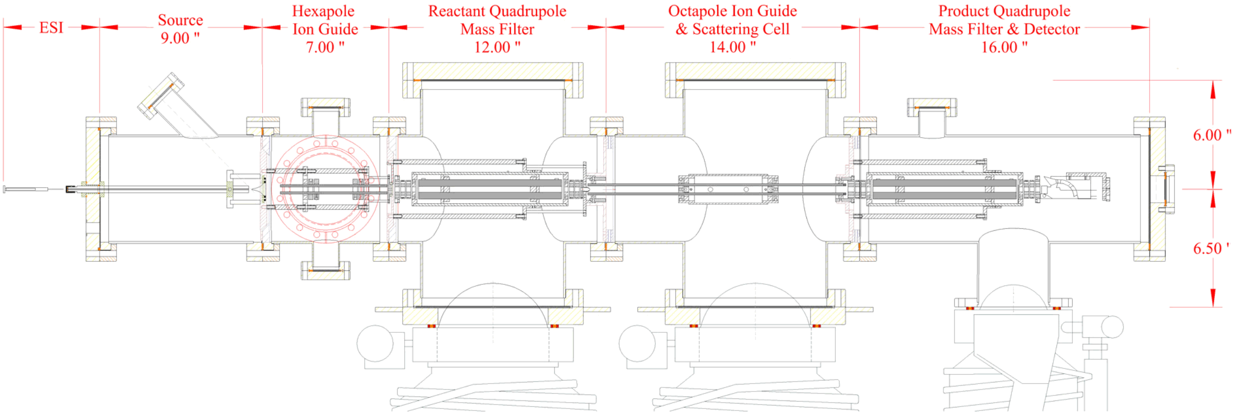

Figure 1.1 Schematic diagram of the electrospray ionization guided-ion-beam tandem mass spectrometer

Electrospray Ionization Source ESI is an important technique for the transfer of biomolecular ions from solution to the gas phase. Prior to ESI, multiple techniques have been employed for ionization of biomolecules, including plasma desorption, fast atom bombardment (FAB) and matrix-assisted laser desorption ionization (MALDI). In comparison with these techniques, ESI is able to achieve ion transfer in a simpler and purer way, avoiding creating fragment ions and imparting extra internal energy to the ions.[2]

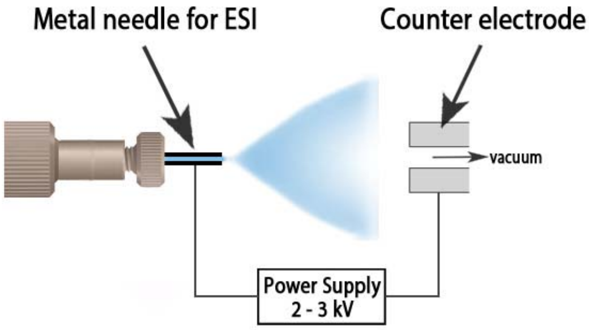

Figure 1.2 Schematic representation of ESI

From electrolyte dissolved in solvent to charged naked ions in the gas phase, ESI process consists of three successive major steps, illustrated in Figure 1.2. Firstly, the metal needle connects to a syringe (Hamilton Gastight instrument syringe), which feeds the solution through a polyether ether ketone (PEEK) tubing (i.d. 0.007 in) at a constant speed of ~0.03 ml/hr. The needle is biased at 2 – 3 kV relative to ground, with the same polarity as the ions of interest. Consequently, charged droplet forms at the ESI needle tip, and the coulombic repulsion pushes the charged droplet off the tip. Secondly, due to solvent evaporation from droplets and resulting droplet shrinkage, the surface tension of the liquid is ultimately overcome by the strong coulomb repulsion among charged ions located at the droplet surface, leading to continuous breakdown of droplets into those of smaller size. Eventually, charged droplets shrink to very small highly charged droplets and individual ions in the gas phase.

The potential required for the onset of electrospray, V_{on}, can be calculated as[3]

$$V_{on} = (\frac{r_c \gamma cos\theta}{2\varepsilon_0})^{1/2} \times \ln\left(\frac{4d}{r_c}\right) \times f_1$$

where r_c (inch) is the outer radius of ESI needle, γ (millinewton per meter) is the surface tension of the solvent, θ (radian) is the half angle of the Taylor cone, ε_0 is the relative dielectric constant of vacuum, d (mm) is the distance between ESI tip and counter electrode and f_1 is the scaling factor, which, in our case, is 0.34.

The droplet size can be estimated using the following equation: [3]

$$R = (V_f \varepsilon / K)^{1/3} \times f_2$$

where V_f (mL/hr) is the solution flow rate of through electrospray needle, ε is the permittivity of solvent relative to vacuum, K ($\Omega^{-1} \cdot cm^2/L$) is electrical conductivity of solution and f_2 is the scaling factor (equal to 0.103 in our case).

In experiments, samples were dissolved in appropriate solvent at concentrations of 10^{-3} – 10^{-4} M and, if necessary, sonicated to form a transparent and uniform solution. The solution was sprayed into the ambient atmosphere through the electrospray needle using a syringe pump (KD Scientific model 100) at a constant flow rate (0.03 – 0.05 ml/hr), optimized for a better cone-shape spray thus a higher ion intensity. The electrospray needle was prepared from 35-gauge hypodermic stainless steel tubing (0.13 mm o.d. × 0.06 mm i.d., Small Parts Inc.), and biased at ± (2.0 – 3.2) kV relative to ground (+ for positive ions and – for negative ions, respectively). The electrospray needle was mounted on an X-Y-Z stage (Newport 400 linear stage and 481-A rotation stage), so that its position could be adjusted to optimize the ESI performance. Charged droplets formed from the electrospray needle were fed into a heated desolvation capillary. The distance between the electrospray needle tip and the sampling orifice of the capillary was 5 – 15 mm.

Source chamber Charged droplets formed from ESI carried a great deal of residual solvent molecules. In the first vacuum chamber, a desolvation capillary assembly was used to desolvate and remove these solvent molecules.

The capillary assembly, similar to an arrangement used by Armentrout and co-workers,[4] consists of a stainless steel capillary tubing (1.58 mm o.d. × 0.66 mm i.d. × 25.4 cm long, VICI Precision Sampling Inc.) which fits tightly into a 9.5 mm o.d. × 1.6 mm i.d. stainless steel tubing holder (Higher Pressure Equipment Co.). The assembly was electrically isolated from the front flange using a PEEK insulator, which allowed us to bias the capillary tubing at ± (70 – 110) V (+ for positive ions and – for negative ions, respectively) relative to ground and heat it to 140 – 160 °C (using heating tape) during experiments. Charged liquid droplets and solvated ions underwent continuous desolvation as they pass through the heated capillary,[5] converting to gas-phase ions. Ions were focused toward the capillary axis by the strong gas flow and then transported through the long capillary.[5]

A skimmer with an orifice of 1.5 mm (Beam Dynamics, Inc.) was located ~5 mm from the capillary end, separating the ion source chamber and the hexapole ion guide. The distance between the capillary end and skimmer could be adjusted to control the gas throughout to the second chamber. (The second chamber pressure was maintained at 15 – 20 mTorr for efficient collisional cooling, *vide infra*.) The skimmer was biased at ± (10 – 70) V (+ for positive ions and – for negative ions) relative to ground, and the electrical field between the capillary and the skimmer removed remaining solvent molecules by collision-induced desolvation,[5] and prevented large solvent clusters from depositing downstream.[6, 7]

Hexapole ion guide chamber Ions that emerged from the skimmer were passed into a rf hexapole ion guide. The hexapole ion guide was constructed of six 3.18 mm diameter centerless-ground stainless steel rods (PIC Design), 15 cm long, equally spaced on a 9.5 mm diameter circle. Radio frequency (rf) potentials were applied to the rods using a rf generator[8] operating between 2 and 3 MHz with peak-to-peak rf amplitude up to 400 V. The dc bias voltage of the hexapole ion guide was maintained at 1 V.

The hexapole chamber was maintained at a pressure of 15 – 20 mTorr. For ions of low kinetic energies, ion velocities were dampened by collisions with background gas and ions were confined towards the center line of the hexapole. This collisional focusing[9] process could lead to the increase in ion transmission. In addition, the collisions also resulted in the relaxation of ion internal energies (both rotational and vibrational) to a Maxwell–Boltzmann distribution at ambient temperature, leading to the thermalization of internal and translational energies of ions.[4, 9, 10]

Ions subsequently passed into a set of entrance focusing lenses and were injected into the first quadrupole mass filter.

1st quadrupole mass filter Both quadrupole mass filters in the mass spectrometer used Extrel 9.5 mm diameter tri-filter rods. These highly precisely machined tri-filter quadrupole mass filters were dedicated to provide high ion transmission. Immediately before and after the four main rods, pre- and post-filters made of short stub rods were equipped to help collimate the ions going into and exiting the mass filter and improve transmission. Each set of pre- and post-filters was connected to the same DC voltage.[11]

The quadrupole mass filter operated at 880 kHz (Extrel model 150 QC) to cover the mass/charge (m/z) range from 10 to 4,000, or at 2.1 MHz for m/z range from 1 to 500 for mass analysis of light ions at a high mass resolution.

The first quadrupole mass filter was used for mass selection of reactant ions to be used for subsequent ion-molecule scattering. For conventional mass spectral measurements, the first quadrupole mass filter was operated in the rf-only mode as an ion guide, and mass scans were performed by the second quadrupole mass filter.

The octopole ion guide chamber Mass-selected ions from the first quadrupole mass filter were then injected into the rf octopole ion guide. In comparison with the quadrupole mass filter, the octopole ion guide is a rf-only device with inhomogeneous rf field, which trapped ions in the radial direction. With more rods than quadrupole, octopole has a more homogeneous trapping field, providing higher confining efficiency. Figure 1.3 shows the schematic of an octopole ion guide, composed of eight poles equally spaced on an inscribed circle with radius r_0. The effective radial trapping potential can be calculated by

$$V_{eff} = \frac{n^2 q^2 V_0^2}{4 m r_0^2 \omega^2} (\frac{r}{r_0})^{2n-2}$$

where q is the charge of given ions, V_0 is the potential, m is the mass, r_0 is the radius of the inscribed circle, ω is the rf potential frequency and $2n$ is the number of poles. For octopole, 2n is equal to 8. Thus, the equation can be re-written as shown in Figure 1.3.

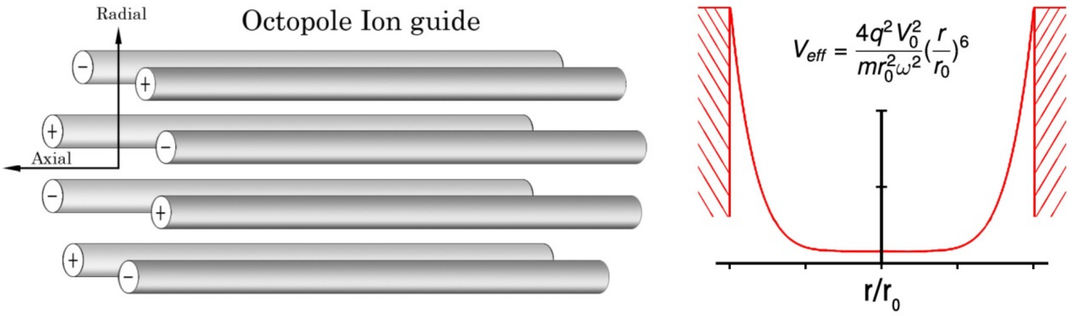

Figure 1.3 Schematic of octopole ion guide, and a plot of effective radial trapping potential

In our experiments, the octopole ion guide operated at 2.6 MHz with a peak-to-peak amplitude of 700 V. DC bias voltage was applied to the ion guide, and its amplitude was varied from –500 to +500 V. The dc bias voltage was used in the retarding potential analysis (RPA)[12] to determine the initial kinetic energy of selected ions, i.e., beam intensities of ions were measured while sweeping the octopole bias. The dc bias voltage also allowed control of the kinetic energy of ions in the laboratory frame. Ion kinetic energies in the lab frame (E_{lab}) are converted to collision energies in the center-of-mass frame (E_{col}) using $E_{col} = E_{lab} \times m_{neutral}/(M_{ion} + m_{neutral})$, where $m_{neutral}$ and M_{ion} are masses of neutral collision gas and ions, respectively. The octopole passed through a scattering cell containing the collision gas (Xe, Ar, or $^1O_2$) at various pressures.

2nd quadrupole mass filter and the electron multiplier detector Primary ions and their product ions were collected by the octopole ion guide, and directed to the second quadrupole mass filter for mass analysis. Ion signals were counted using an off-axis electron multiplier (DeTech 411, pulse width > 18 – 20 nSec, dark count < 0.05 count per second) operating in positive or negative ion pulse counting mode, depending on the charge states of ions.

An electron multiplier is a device that can amplify single charged species into a shower of electrons (i.e., a pulse within a short period), enabling the detection of single charged ions by a pulse counting device. In principle, when a charged ion hits the surface of secondary emission material, the bombardment triggers a secondary emission, leading to approximately 1 – 3 electrons off the surface. Driven by the electronic field, these secondary electrons undergo further secondary emissions repeatedly, eventually resulting in a pulse at the collector of the multiplier.

The electronic pulse was delivered to a preamplifier/discriminator (Advanced Research Instruments FT-100 for positive ions; MTS-100 for negative ions) for amplification and noise rejecting. The amplified and discriminated signal was routed to a BNC connector block (National Instruments BNC-2090A), which interfaced to a computer housing two multifunction DAQ cards (National Instruments PCI-6229 and PCI-6289) for pulse-counting in our LabVIEW program. The voltage configurations of the electron multiplier used in positive and negative ion mode are given in Figure 1.4, respectively.

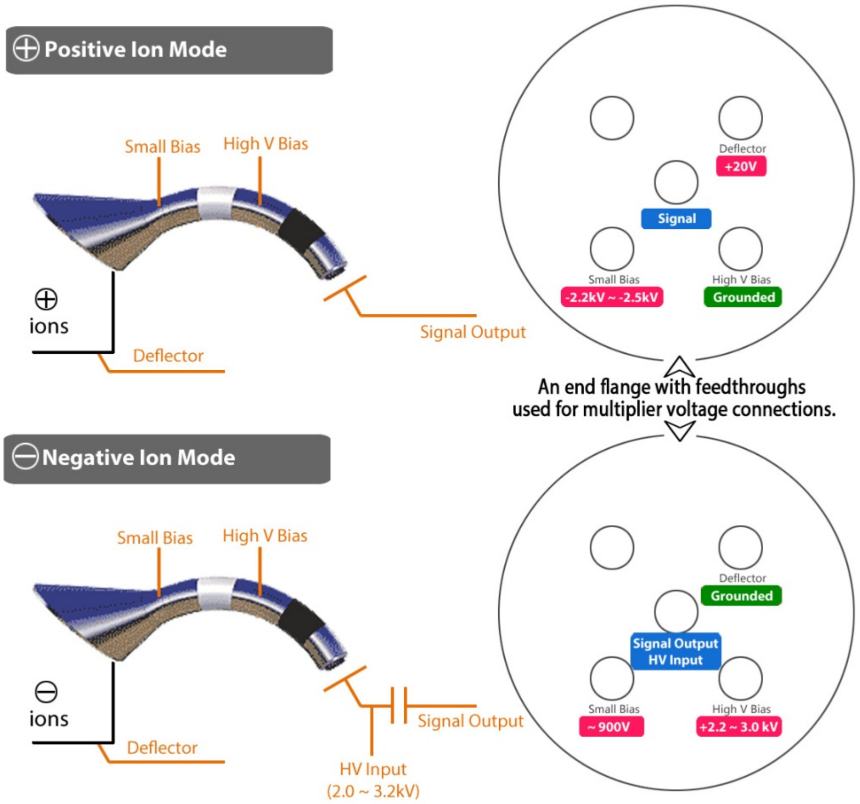

Figure 1.4 Electron multiplier voltage configurations in positive/negative ion mode

1.2 Vacuum Pumps

During experiments, pressures for the five chambers of our mass spectrometer were typically as follows:

- Chamber 1: ~2 Torr
- Chamber 2: $15\sim20 \times 10^{-3}$ Torr
- Chamber 3: 1×10^{-7} Torr
- Chamber 4: 2×10^{-6} Torr
- Chamber 5: 1×10^{-7} Torr

Based on these pressure requirements, three types of vacuum pumps were employed in our system. A rotary piston mechanical pump was chosen for chamber 1 for its rough vacuum. With this type of pump, pressure as low as 10^{-2} Torr could be obtained.[14] The turbomolecular pump (TP) could operate in pressure range of 10^{-2} Torr to below 5 x 10^{-10} Torr.[14] It was used for chamber 2, offering a reliable, clean and oil-free vacuum with little vibration. Featuring high pumping speed for all gases and relatively low cost, oil diffusion pumps (DPs) had been serving as the workhorse for high vacuum systems. Operating with an oil of low vapor pressure, it is possible to achieve pressure in the 10^{-8} Torr range. DPs with different pumping speeds were used for chamber 3, 4, and 5, respectively, to meet their vacuum needs. It should be noted that both turbomolecular pump and oil diffusion pump cannot operate at or exhaust to the atmosphere. Therefore, each of them requires a backing pump to expel gases primitively to achieve rough vacuum. Figure 1.5 illustrates pumping system of the mass spectrometer, including various pumps used for each chamber, and foreline and roughing valves in the pumping line.

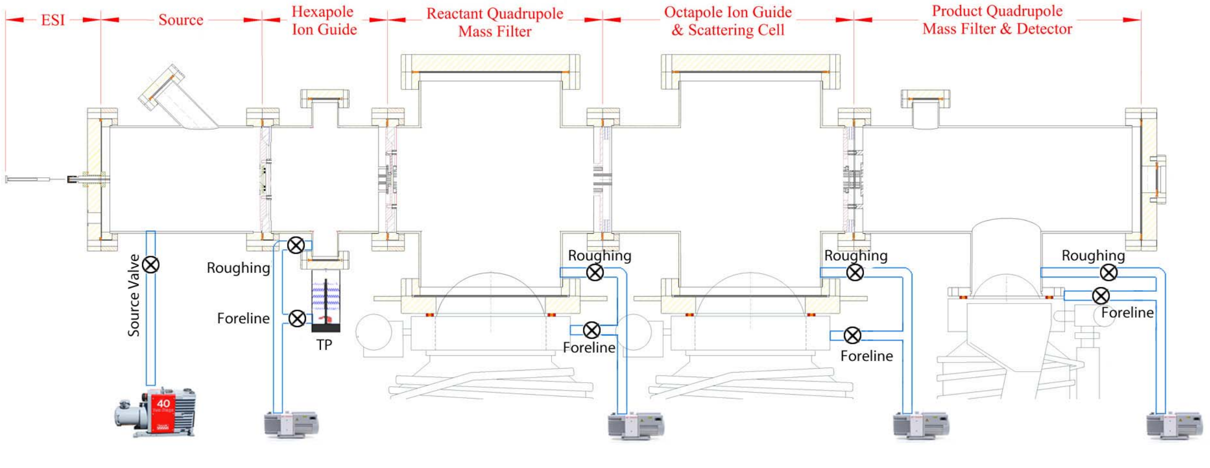

Figure 1.5 Block diagram of the pumping system for the mass spectrometer

More specifically, the source chamber was pumped by a 12 L/s rotary pump (Edwards model E2M40) to a pressure of ~1.8 Torr during experiments. The second vacuum chamber was evacuated by a turbomolecular pump (Varian model V301) backed by a 3.6 L/s rotary pump (Edwards model RV12). The pumping speed of the turbomolecular pump was adjusted to 70% of its full speed (300 L/s) to keep a pressure of 10 – 20 × 10^{-3} Torr in the second chamber. At this pressure range, the mean free path of most ions was around 1 – 2 mm. Therefore, the interaction of ions with background gas (mainly air and solvent molecules) in the hexapole ion guide led to collisional focusing, and thermalization of internal and translational energies of ions.[4, 9, 10] The third and fourth vacuum chambers were each pumped by a 700 L/s oil diffusion pump (Edwards Diffstak 160/700P), and the detector chamber was pumped by a 300 L/s oil diffusion pump (Edwards Diffstak 100/300P). Diffusion pumps were each backed by a 3.6 L/s rotary pump. The standard operating procedure (SOP) for the mass spectrometer is described in Appendix A.

MP2 to MP5 not only operated as foreline pumps for turbomolecular pump and diffusion pumps, but were also used to rough down chambers to a low vacuum (< 10 mTorr) when starting to pump down the mass spectrometer from atmospheric pressure. However, they could only be all used as foreline or roughing pumps at one time; otherwise, they would cause oil back-stream to chamber. In our interlock system (to be discussed in next section), the roughing lines (which controls the MPs to pump down chamber) and forelines 2 – 5 were controlled by the opposite terminals of the same switches, so that all MPs could operate only for foreline pumping or roughing pumping at a time. In this way, the system was protected from fault operation of turning on both roughing and the foreline simultaneously.

1.3 Interlock system

Our mass spectrometer was regularly in operating mode for experiments during work hours and was switched to standby mode during nights. All vacuum pumps were kept on

7/24 to maintain the vacuum status of the mass spectrometer. The apparatus was only shut down occasionally for pump maintenance service once every six months, or for troubleshooting should problems occurred. It is essential to protect the mass spectrometer from faulty operation in experiments and unexpected accidents particularly when the instrument was left unattended, such as electric power failure, any pump failure and pressure burst, cooling water and compressed air failure, etc. On the basis of this consideration, a set of interlock system was designed and incorporated into the instrument control panel.

In the interlock system, a powered control line was routed through various peripheral devices in series, including cooling water pressure switch, compressed air pressure switch, convectron vacuum gauges/relays monitoring foreline pressure for five mechanical pumps MP1/2/3/4/5, and three thermostatic sensors/relays monitoring cooling coil temperature of diffusion pumps DP3/4/5. This control line was able to monitor the status of these sensors/switches/relays. In case any of these devices work abnormally (i.e., reaches set points), the control line would break in one of these relays. As a consequence, a series of actions would be executed automatically; 1) all high voltage power supplies for various ion guides, lenses and mass filters would be shut off immediately; 2) the gates between vacuum chambers and diffusion pumps (or turbomolecular pump) would be closed immediately, to prevent possible oil back-streaming to the chambers; and 3) all diffusion pumps would also be shut off immediately, leaving only turbomolecular pump and mechanical pumps running. In the meantime, an alarm would be triggered and a time delay relay would start counting down. After a pre-set period of time, ~20 sec in our case, the time delay relay would be shut off and the whole system was shut off. Thus the system could be protected even if left unattended. In case the situation comes back to normal within the pre-set period, all gates would re-open, diffusion pumps would restart, and all electronics would resume working. In an emergency situation, a push-off "Kill" button could be pressed manually and the system would shut off immediately.

1.4 Calibrations

Initial kinetic energy (E_0) and energy distribution (ΔE) of primary ion beam RPA[12] was employed to determine the E_0 and ΔE of the primary ion beam, using the octopole as the retarder (i.e., primary ion beam intensity was measured while sweeping the octopole dc bias). A low pole dc bias voltage applied to the octopole would allow the majority of the selected ions to pass through the octopole mass filter. Scanning this voltage incrementally raised the potential barrier progressively, eventually hindered most ions from passing through the octopole and killed the ion intensity.

An example kinetic energy profile for Na^+(proline) is demonstrated in Figure 1.6. The first derivative of the RPA is calculated and shown in open circles. To better evaluate the E_0, a Lorentzian curve is fitted to the data points with a mean of 0.75 eV and a full-width-at-half-maximum (FWHM) of 0.31eV. As a result, the E_0 of the primary ion beam is determined to be 0.75 eV with ΔE of 0.31 eV.

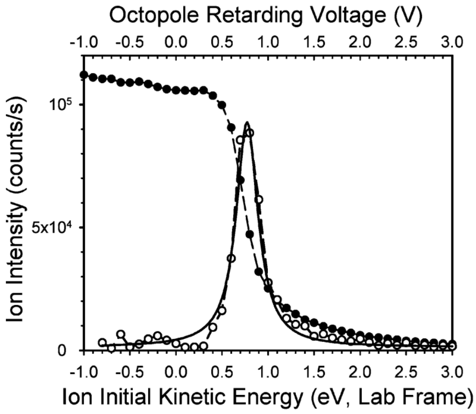

Figure 1.6 Kinetic energy profile for Na^+(proline), shown in the laboratory frame (lower x-axis). Closed circles: ion intensity versus the octopole retarding voltage (upper x-axis). Open circles: the first derivative of the RPA curve. Solid line: a Lorentzian curve fitted to the data points with a mean of 0.75 eV and a FWHM of 0.31 eV.

Cross section and cell length Integral cross sections were calculated from the ratios of reactant and product ion intensities, the scattering cell gas pressure, and the effective length of the scattering cell. Scattering cell gas pressure was measured by a capacitance manometer (MKS Baratron 690 head and 670 signal conditioner). To allow subtraction of background from the detector, and from reactions occurring in the ion guide portions outside the scattering cell, all ion signals were measured with the target gas flow directed into the scattering cell ("cell-on"), and also with the same flow directed into the vacuum chamber ("cell-off").[15] Since these two conditions only differ in the gas density inside the scattering cell, the difference in "cell-on" and "cell-off" signals provided the accurate product ion intensities due to reactions inside the scattering cell. To calibrate the effective length of the scattering cell, the cross section for CID of Na^+(proline) with Xe was measured, and the results were scaled to that of Moision and Armentrout, which was obtained using two different ion sources, a dc discharge/flow tube source[16] and an ESI ion source.[4]

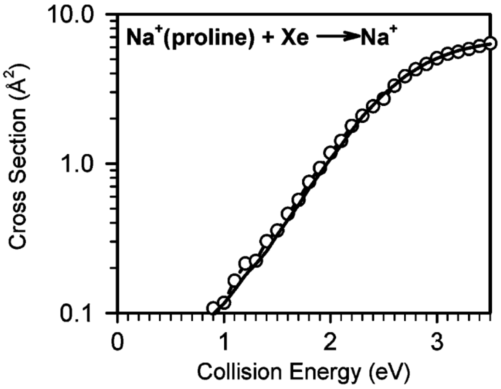

Figure 1.7 Cross sections for CID of Na^+(proline) with xenon as a function of collision energy. Open circles: experimental cross sections. Solid line: simulation based on the modified line-of-centers model.

Experimental cross sections for CID of Na^+(proline) with Xe as a function of E_{col} are shown in Figure 1.7. The calibration was performed at multiple cell pressures (0.05, 0.10, 0.15, and 0.25 mTorr), and the relative uncertainty in calibration was determined to be 10 –

15%. However, there may exist some absolute uncertainty due to the possibility of different collection efficiencies for reactant ions (Na^+(proline), m/z = 138) and product ions (Na^+, m/z = 23). The calibrated effective cell length is close to what was found for a similar guided-ion-beam scattering cells[17] calibrated using $Ar^+ + D_2 \rightarrow ArD^+ + D$.[12] Therefore, the calibration demonstrated that our collection efficiency was at least reasonably uniform for widely spread reactant and product ion masses.

Internal energy of ion beams An obvious issue regarding this ESI ion source was the internal energy distribution of the primary ions. Due to thermalization in the hexapole, the internal energy was expected to be approximately thermal. To address this issue, the energy dependence of the CID cross section of Na^+(proline) + Xe was fit using the modified line-of-centers model[17-19]

$$\sigma(E_{col}) = \sigma \frac{(E_{col}+E_{vib}+E_{rot}-E_0)^n}{E_{col}} \qquad (1)$$

for $(E_{col} + E_{vib} + E_{rot}) > E_0$, otherwise, $\sigma(E_{col}) = 0$. Here $\sigma(E_{col})$ is the cross section, σ_0 is an energy-independent normalization constant, E_{vib} and E_{rot} are the vibrational and rotational energy of reactant ions, E_0 is the threshold energy, n is a fitting parameter used to adjust the slope of $\sigma(E_{col})$ (equal to 1.0 in the canonical LOC model[20]). To fit experimental data, this model $\sigma(E_{col})$ function is convoluted with the experimental broadening functions, including those from ion beam and target gas velocities and ion rotational and vibrational energies. The fitting was done using the program developed by Anderson and coworkers.[19] It is of interest to probe the distribution of reactant ion vibrational energy. To this end, values of E_0 (=1.94 eV) and n (=1.5) determined by Armentrout et al.[4, 16] were used. For target xenon atoms, a Maxwell-Boltzmann distribution of velocities at 300 K was used. For Na^+(proline) ions, we used the RPA measured kinetic energy distribution (Figure 1.7), and assumed a

Maxwell-Boltzmann distribution of rotational energy at 300 K, leaving only E_{vib} adjustable (σ_0 is simply a scaling factor, it does not affect the threshold or curvature of the cross section). In the fitting, the vibrational energy distribution is a function of $E_{\mathrm{vib\_peak}}$,

$$P(E_{vib}) = \frac{(E_{vib})^{1/2} \times \exp(-E_{vib}/2E_{vib\_peak})}{(E_{vib\_peak})^{1/2} \times \exp(-0.5)} \qquad (2)$$

where $E_{\mathrm{vib\_peak}}$ is the most probable vibrational energy of the Boltzmann distribution by summing over the partition function. Vibrational frequencies of Na^+(proline) were calculated at the B3LYP/6-311G** level of theory and scaled by a factor of 0.9613.[21] The model $\sigma(E_{\mathrm{col}})$ was run through a Monte Carlo simulation that included all experimental broadening factors. For each experimental E_{col}, the simulation was repeated for 20,000 samples, thereby building up a simulated cross section for comparison with the experiment. Due to the large number of vibrational modes in Na^+(proline), kinetic shifts in the threshold are expected; i.e., collision energy significantly in excess of the dissociation limit was required to drive fragmentation on the experimental time scale (200 – 500 μs).[22] To correct for the kinetic shifts, RRKM lifetimes were calculated with the program of Zhu and Hase,[23] assuming orbiting transition states for dissociation. The RRKM results were then used to decide each sample would lead to detectable dissociation or not. The kinetic shift for this system was around 0.15 eV.

Figure 1.7 shows experimental cross sections for collision-induced dissociation of Na^+(proline) with Xe as a function of E_{col}, together with the corresponding convoluted model $\sigma(E_{\mathrm{col}})$ fitted to eq 1. The best fit E_{vib} is around 0.19 eV, which corresponds to a vibrational temperature of 310 K. (For comparison, the average E_{vib} at 298 K is 0.17 eV). The extracted ion vibrational temperature from simulation is slightly elevated from the ambient temperature, presumably due to rf power dissipation by the hexapole. The conclusion could be drawn that primary ions undergo complete thermalization via ion/neutral collisions in the hexapole ion guide and their internal energy can be well defined using a Maxwell-Boltzmann distribution.

References

1 D. Gerlich, 'Inhomogeneous RF fields: A versatile tool for the study of processes with slow ions', in *State-Selected and State-to-State Ion-Molecule Reaction Dynamics. Part I. Experiment*, ed. by C. Y. Ng and M. Baer (New York: John Wiley & Sons, Inc., 1992), pp. 1-176.
2 P. Kebarle, and L. Tang, *Analytical Chemistry,* 1993, 65, 972A-986A.
3 J. S. Klassen, Y. Ho, A. T. Blades, and P. Kebarle, *Adv. Gas-Phase Ion Chem.,* 1998, 3, 255-318.
4 R. M. Moision, and P. B. Armentrout, *J. Am. Soc. Mass Spectrom. ,* 2007, 18, 1124-1134.
5 S. K. Chowdhury, V. Katta, and B. T. Chait, *Rapid Commun. Mass Spectrom.,* 1990, 4, 81-87.
6 T. Kim, K. Tang, H. R. Udseth, and R. D. Smith, *Anal. Chem.,* 2001, 73, 4162-4170.
7 K. Tang, A. V. Tolmachev, E. Nikolaev, R. Zhang, M. E. Belov, H. R. Udseth, and R. D. Smith, *Anal. Chem.,* 2002, 74, 5431-5437.
8 R. M. Jones, and S. L. Anderson, *Rev. Sci. Instru.,* 2000, 71, 4335-4337.
9 D. J. Douglas, and J. B. French, *J. Am. Mass Spectrom.,* 1992, 3, 398-408.
10 A. N. Krutchinsky, I. V. Chernushevich, V. L. Spicer, W. Ens, and K. G. Standing, *J. Am. Soc. Mass Spectrom.,* 1998, 9, 569-579.
11 'Manual for 150-QC quadrupole power supply', ABB Extrel, 1997).
12 K. M. Ervin, and P. B. Armentrout, *J. Chem. Phys.,* 1985, 83, 166-189.
13 'DeTech Inc. Technical Notes', <http://www.detechinc.com/technotes.html> [Accessed 10.3 2012].
14 *Basic Vacuum Practice*. 3rd ednVarian Associates, Inc., 1992).
15 Y.-H. Chiu, H. Fu, J.-T. Huang, and S. L. Anderson, *J. Chem. Phys.,* 1995, 102, 1199 - 1216.
16 R. M. Moision, and P. B. Armentrout, *J. Phys. Chem. A,* 2006, 110, 3933-3946.
17 J. Liu, B. Van Devener, and S. L. Anderson, *J. Chem. Phys.,* 2002, 116, 5530-5543.
18 P. B. Armentrout, *Int. J. Mass Spectrom.,* 2000, 200, 219-241.
19 M. B. Sowa-Resat, P. A. Hintz, and S. L. Anderson, *J. Phys. Chem.,* 1995, 99, 10736-10741.
20 R. D. Levine, and R. B. Bernstein, *Molecular Reaction Dynamics and Chemical Reactivity* (New York: Oxford University Press, 1987).
21 J. B. Foresman, and A. Frisch, *Exploring Chemistry with Electronic Structure Methods*. 2nd edn (Pittsburgh, PA: Gaussian, Inc, 2000).
22 M. T. Rodgers, K. M. Ervin, and P. B. Armentrout, *J. Chem. Phys.,* 1997, 106, 4499-4508.
23 L. Zhu, and W. L. Hase, 'A General RRKM Program(QCPE 644), Quantum Chemistry Program Exchange', (Bloomington: Chemistry Department, University of Indiana, 1993).

Chapter 2

Instrument Control and Data Acquisition

2.1 LabVIEW

LabVIEW, short for Laboratory Virtual Instrumentation Engineering Workbench, is a design platform and development environment built specifically for engineers and scientists to create measurement and control systems for scientific apparatus.[1] It was initially developed by National Instruments, and is widely used nowadays for instrument control, data acquisition and industrial automation. Through unprecedented hardware integration, LabVIEW enables us to manipulate electronic devices and acquire signals in a precisely synchronized manner from our mass spectrometer.

Unlike other traditional programming languages, LabVIEW uses a graphical programming interface, where all data structures and algorithms are represented and carried out by wiring various function blocks, largely eliminating difficulty and complexity associated with traditional programming languages. The graphical language, also referred to as G, is a data flow programming language, originally released for the Apple Macintosh in 1986. On a graphical block diagram, blocks of various functions can be created and wire-connected graphically, which resembles the "source code" in traditional text-based programming languages. In addition to the block diagram, a front panel is provided to accommodate control and display components, as a human-computer interaction interface, enabling user inputs, live data display and hardware status feedback in a friendly way.

Each LabVIEW program designed for a specific objective is called a “virtual instrument” (VI). In the meantime, each VI can be embedded into other VIs, referred to as subVI in this scenario, working as a sub-routine for its parent VI.

My program was originally designed using LabVIEW 8.5 (released in August 2007), and updated in LabVIEW 2012 (released in Fall 2012) to utilize the most recent features and to add more functions.

2.2 Hardware for Instrument Control and Data Acquisition

Computer A Dell precision 390 personal computer with an Intel® Core 2 CPU (2.4GHz), 3GB of memory and a 1 GB hard drive was used for the instrument control and data acquisition, running Microsoft Windows XP operating system with service pack 3. With National Instruments (NI) LabVIEW and PCI device drivers installed, it acted as the I/O coordinator for various electronic devices. A LCD monitor featuring resolution of 1280px × 1024px or higher is required and was used for user inputs and data display.

Table 2.1 NI PCI devices and their connector blocks

PCI Devices	Installed in PC	Name in LabVIEW	68-pin connectors	Connector Blocks
PCI 6229	Lower PCI slot	Dev1	PCI 6229-0	BNC 2090A-1
			PCI 6229-1	SCB-68-1
PCI 6289	Upper PCI slot	Dev2	PCI 6289-0	BNC 2090A-2
			PCI 6289-1	SCB-68-2

NI DAQ devices Two NI PCI data acquisition (DAQ) cards, PCI-6229 and PCI-6289, were installed in the computer, serving as the interface between LabVIEW software and the peripheral hardware. The PCI-6229 card was installed in lower PCI slot in the computer so that it was recognized as Dev1, while the PCI-6289 card was installed in upper PCI slot, recognized as Dev2 (summarized in Table 2.1). Each PCI card was connected (via performance shielded cables NI SHC68-68-EPM) to two BNC-2090A connector blocks, or

SCB-68 connector boxes, for signal breakdown and physical wiring. Input/output (I/O) signals were dispatched from these connector blocks/boxes to respective electronic devices via BNC cables.

Each of the PCI cards features 4 analog outputs (AOs), 32 analog inputs (AIs), 48 digital I/Os (DIOs) and two 80MHz 32-bit counters/timers. In our application, PCI-6229 operated as the master card with the two counters/timers employed for pulse counting and for synchronization of multiple channels. PCI-6289 functioned as a slave card; only its AOs were employed, with all DIOs and both counters/timers idle.

Despite that the maximum clock frequency of the counters built into PCI 6229 was 80MHz, the maximum counting rate was 20MHz. As discussed in the M-series DAQmx manual,[2] connecting a signal to the counter externally limits the usable frequency by a factor of 4, rendering that the minimum detectable pulse width is 16.0 ns and the gap between rising edges of two successive pulses must be no less than 50.0 ns. The reasons are described as follows. A counter employs two load registers (load register A and B) that determine the characteristics (delay and width) of its pulse. Each load register can be configured with a minimum value of 2. In other words, each register has to have a minimum of 25 ns (2 * 12.5 ns, where 12.5 ns is the minimum detectable period of the 80MHz timebase), totaling a minimum of 50 ns for both registers. As a consequence, the maximum output frequency that can be achieved is a quarter of the timebase source frequency, i.e., 80MHz/4 = 20MHz.

The resolution of AOs for both PCI cards was 16 bits. With the voltage range of –10 V to +10 V, the minimum distinguishable voltage was $20\text{V}/2^{16} \approx 0.3\text{mV}$. In my application, 10 V command voltage corresponded to 4,000 amu, i.e., the voltage representing 1 amu was

2.5mV (10V/4,000amu). Thus, the AO voltage outputs had sufficient resolution for use as mass command voltages for two quadrupole mass filters.

Jumper wires were configured on the front panel of BNC-2090A blocks for gate signal routing and output monitoring (see Figure 2.1). Their functions are discussed as follows.

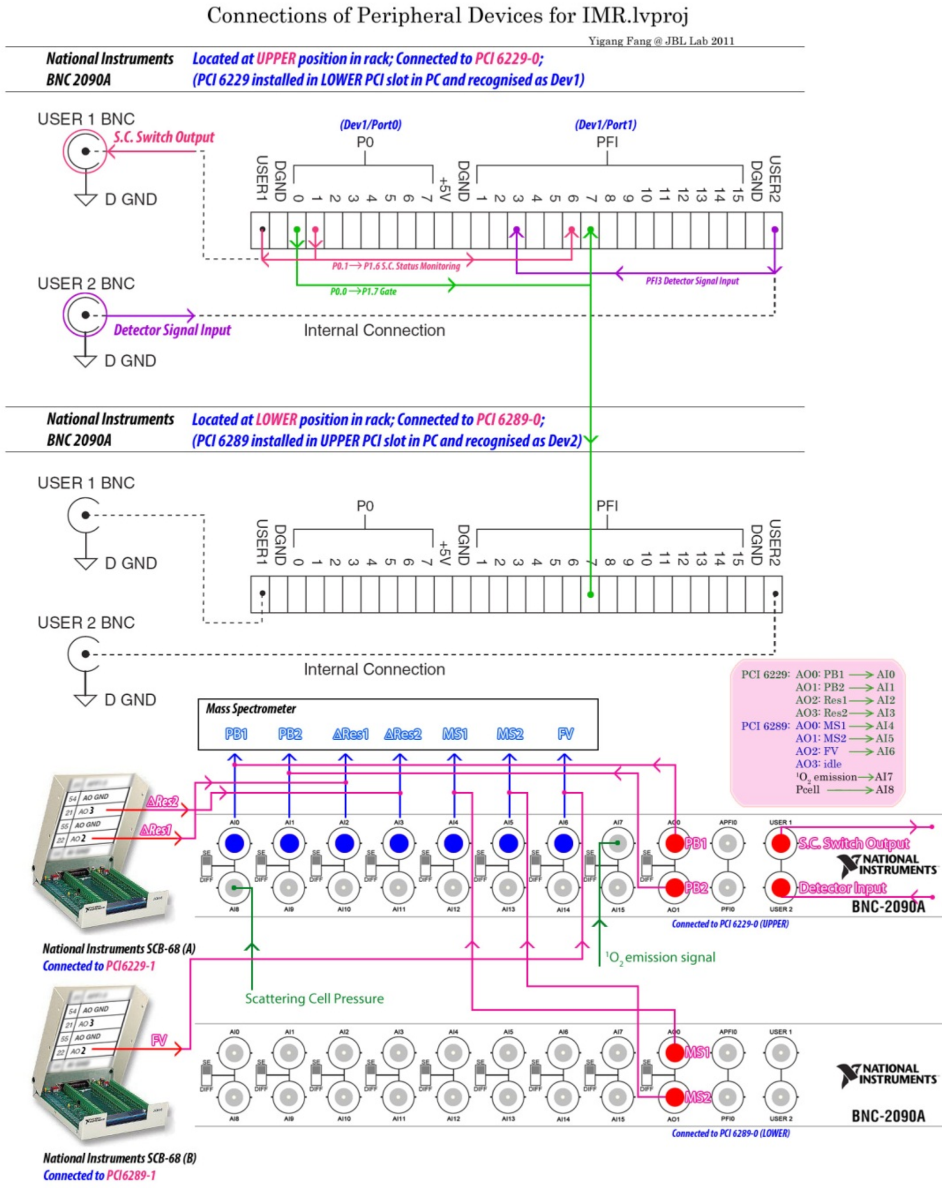

Figure 2.1 Connections of peripheral devices

In my program, a gate signal was fabricated to synchronize AOs and DOs. The gate signal was generated and outputted to Dev1/Port0.0, and physically connected to Dev1/Port1.7 and Dev2/Port1.7 with jumper wires. Two BNC 2090A boxes were bridged together with a jumper wire from Dev1/Port0.0 to Dev2/Port1.7. In this way, the AOs on PCI 6289 were able to "see" gate signals generated from PCI 6229.

To operate the scattering cell switch, a DO came out of USER 1 BNC (which was internally connected to Dev1/Port0.1), and was used to control a solid state relay, which would open the scattering cell when DO is high and close the cell when DO is low. In the meantime, it was jumper-wired to Dev1/Port1.6 for live monitoring.

The signal from the electron multiplier was amplified by a preamplifier/discriminator (Advanced Research Instruments FT-100 for positive ions; MTS-100 for negative ions), and fed to Dev1/Port1.3 (through USER 2 BNC) for pulse counting.

The AO definitions are listed in Table 2.2, along with the monitoring ports. Four AOs on PCI-6229 and three AOs on PCI-6289 were used to control resolution, pole bias and mass command of two mass filters, and floating voltage of octopole ion guide, which will be discussed in the next section.

Table 2.2 AO definitions of two PCI cards and their monitoring ports

Outputs				Inputs		
PCI Devices	AO	Definition	Connected to	Live monitoring		
PCI-6229	AO0	Pole DC Bias 1	Quad Ctrl Box 1	➔	AI0	PCI-6229
	AO1	Pole DC Bias 2	Quad Ctrl Box 2	➔	AI1	
	AO2	ΔRes 1	Quad Ctrl Box 1	➔	AI2	
	AO3	ΔRes 2	Quad Ctrl Box 2	➔	AI3	
PCI-6289	AO0	Mass Command 1	Quad Ctrl Box 1	➔	AI4	
	AO1	Mass Command 2	Quad Ctrl Box 2	➔	AI5	
	AO2	Floating Voltage	Kepco BOP500M	➔	AI6	
	AO3	–	–		–	
$^1O_2$ emission reading from Lock-in amplifier				➔	AI7	
Scattering cell pressure reading from Baratron manometer				➔	AI8	

In order to take into account the variance of $^1O_2$ emission and scattering cell pressure (P_{cell}), both signals were measured through two AIs (AI7 and AI8 on PCI6229) and recorded to data file.

2.3 Instrument Control and Data Acquisition

2.3.1 Instrument Control

Collision Energy Ion collision energies are one of the most critical parameters controlling ion-molecule reactions. In experiments, required ion kinetic energies in the Lab Frame (E_{lab}) are calculated from the collision energies in the Center-of-Mass Frame (E_{col}) to be used in reactions, using $E_{lab} = E_{col} \times (M_{ion} + m_{neutral})/m_{neutral}$, where $m_{neutral}$ and M_{ion} are masses of neutral collision gas and ions, respectively. By dividing the calculated ion kinetic energies by a unit of electric charge, the corresponding DC bias voltages applied to the octopole ion guide can be obtained, referred to as floating voltage. In other words, floating voltage in lab frame (V_{float}) is calculated by:

$$V_{float} = \frac{1}{n \times e}(E_0 - E_{col(CM)} \times \frac{m_i + M_n}{M_n})$$

where n is signed number of charges of given ions, and constant e is the elementary charge.

For instance, for deprotonated Cys ($[\text{Cys–H}]^-$) + $^1O_2$, $n = -1$; $m_i = 120$; $M_n = 32$; suppose $E_0 = 1.0$ eV and the desired $E_{col} = 0.1$ eV, then the floating voltage in lab frame can be obtained by:

$$V_{float} = \frac{1}{-1 \times e}\left(1.0 - 0.1 \times \frac{120 + 32}{32}\right) = -0.525\ V$$

In our LabVIEW program, ion collision energies were controlled by an operational power supply, whose output was precisely and rapidly controlled by an AO signal of NI DAQ card.

Floating voltages coming out of DAQ cards (–4 V to +4 V) were linearly "amplified" by a bipolar operational power supply/amplifier (Kepco BOP500M) by a factor of 50 (–200 V to +200 V). The octopole and all electronic lenses downstream were floated by the same amount.

Mass spectrometer Two quadrupole mass filters, selecting ions by mass/charge ratio (m/z), are critical components in our mass spectrometer. Thus they demand high accuracy and stability of control voltages, and could be controlled precisely by the LabVIEW program. Since the mass command voltages of the quadrupole mass filters were based on DC voltages ranging from 0 to 10 V, they could be controlled using two analog outputs on NI DAQ board, one for each mass filter.

On two home-made quadrupole control boxes, resolution (ΔM) and resolving power (ΔRes) were equipped enabling resolution adjustment for various ion masses. ΔRes is defined as $\Delta\mathrm{Res} = \frac{M}{\Delta \mathrm{M}}$, where M is the mass-over-charge of interest, and ΔM is the mass-over-charge difference between M and its closely accompanying species. The values of ΔRes for each quadrupole are hereafter designated as ΔRes1 and ΔRes2. In our applications, these two ΔRes were controlled by two AOs ranging from –5 V to +5 V, approximately equivalent to a ±1% change in the resolution voltage.[3]

A pole bias voltage was applied to each quadrupole mass filter to finely collimate ion beam. This voltage was controlled by an AO of the DAQ card, and varied from –4 V to +4 V, corresponding to -200 – +200 V actually imposed on the quadrupole mass filters. In the following, this pole dc bias voltage will be noted as PB followed by a number, i.e., PB1, PB2, indicating the quadrupole it applies on.

Scattering cell The scattering cell could be turned on/off using solid state relay controlled by a TTL high/low voltage (DO from PCI 6229). By subtracting the background signal during cell off (the target gas flow directed into the vacuum chamber) from that during cell on (the same flow directed into the scattering cell), the net product ion intensity represents an accurate count of ions produced inside the cell.

All of the AOs were connected to the two home-made quadrupole control boxes for the quadrupole mass filters, with the exception that floating voltage was connected to an operational power supply (Kepco BOP500M).

2.3.2 Data Acquisition

In addition to controlling the mass spectrometer, my LabVIEW program was also designed to acquire signal as well.

Number of ions was counted using a counter on the DAQ device. Besides, the intensity of $^1O_2$ emission measured by a lock-in amplifier and the scattering cell pressure measured by a Baratron Controller were fed to the DAQ device through two AIs for record.

2.4 Data Acquisition Software

Two sets of LabVIEW programs were designed for instrument control and data acquisition of our ESI guided-ion-beam tandem mass spectrometer, named as *MassScan.vi* and *IMR.vi*.

2.4.1 MassScan.vi

MassScan.vi was designed for auto-tuning of various instrument parameters and mass spectra measurements. Figure 2.2 depicts the front panel of the program.

A series of tasks can be executed with the program, including:

- determining initial kinetic energy (E_0) and energy distribution (ΔE) of primary ion beam;
- scanning and optimizing the pole DC bias voltages for the first and second mass filters (noted as PB1 and PB2);

- scanning and optimizing resolutions for the first and second quadrupole mass filter (noted as ΔRes1 and ΔRes2);
- conducting conventional mass scan for each quadrupole mass filter (MS1 scan and MS2 scan); and
- collecting ion intensities at m/z (Single Mass mode).

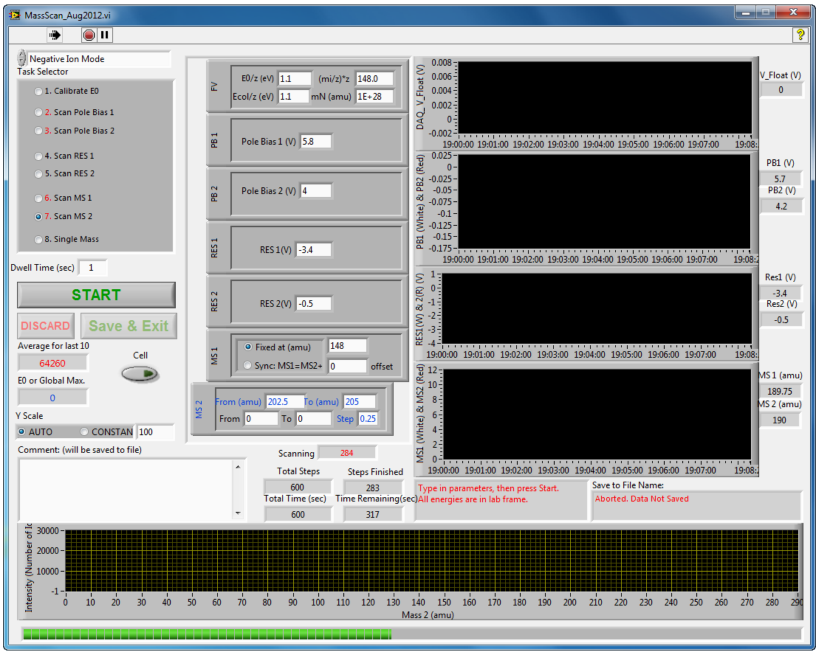

Negative Ion Mode

Task Selector
○ 1. Calibrate E0
○ 2. Scan Pole Bias 1
○ 3. Scan Pole Bias 2
○ 4. Scan RES 1
○ 5. Scan RES 2
○ 6. Scan MS 1
● 7. Scan MS 2
○ 8. Single Mass

Dwell Time (sec) 1

Average for last 10: 64260

E0 or Global Max.: 0

Y Scale: ● AUTO ○ CONSTAN 100

Comment: (will be saved to file)

E0/z (eV) 1.1 (mi/z)*z 148.0

Ecol/z (eV) 1.1 mN (amu) 1E+28

Pole Bias 1 (V) 5.8

Pole Bias 2 (V) 4

RES 1(V) -3.4

RES 2(V) -0.5

● Fixed at (amu) 148

○ Sync: MS1=MS2+ 0 offset

From (amu) 202.5 To (amu) 205

From 0 To 0 Step 0.25

Scanning 284

Total Steps 600 Steps Finished 283

Total Time (sec) 600 Time Remaining(sec) 317

V_Float (V) 0

PB1 (V) 5.7

PB2 (V) 4.2

Res1 (V) -3.4

Res2 (V) -0.5

MS 1 (amu) 189.75

MS 2 (amu) 190

Type in parameters, then press Start.
All energies are in lab frame.

Save to File Name:
Aborted. Data Not Saved

Figure 2.2 Front panel of the LabVIEW program *MassScan.vi*

These procedures are described in detail as follows.

1) **Calibrate E_0** The initial kinetic energy of primary beam was analyzed using the octopole as the retarder. Primary ion beam intensities were measured while sweeping the dc floating voltage applied to the octopole and all electronic lenses downstream, i.e., a retarding potential analysis. Figure 1.6 illustrates the retarding potential analysis for the determination of E_0 for Na$^+$(proline) ion beam. The ion intensity versus the retarding voltage in the laboratory frame is indicated in closed circles, and its first derivative curve is shown in open circles. To locate

the E_0, a Lorentzian curve (in solid line) was fitted to the first derivative curve, resulting in a E_0 of 0.75 eV. By calculating the full width at half maximum (FWHM) of the Lorentzian curve, ΔE was determined to be 0.31 eV.

2-3) **Scan PB1 and PB2** A combination of RF and DC potentials was applied to each quadrupole mass filter. These included a RF potential and a DC potential for ion mass selection, along with a pole DC bias for ion beam collimation. The former two potentials were determined based on m/z of given ions, and generated by a RF/DC power supply (Extrel 150-QC), while the latter was controlled by my LabVIEW program. Before experiments, PB1 and PB2 were scanned individually from –10 V to +10 V to locate optimal values for higher ion intensity.

4-5) **Scan ΔRes1 and ΔRes2** Prior to mass spectra measurements, ΔRes for each mass filter was optimized by measuring the ion intensity at the primary ion m/z, and 2 amu off the primary ion m/z positions, respectively, as scanning the ΔRes control voltage from –5 V to +5 V. An optimal value of ΔRes is the one that gives the highest ion intensity at the primary ion m/z position, while negligible counts when the m/z position is off by 2 amu. This will result in the FWHM of mass peak no more than 2 amu. Note that it may become necessary to compromise the ΔRes and ion intensity, particularly when scanning mass over a wide range.

6-7) **Scan Mass 1 and Mass 2** Quadrupole mass filters are designed to precisely select ions with specific m/z. The m/z value was controlled by the mass command voltages generated by LabVIEW programs.

In Mass 1 scan, the mass scan was performed by the first stage mass filter over a defined m/z range, with the second stage mass filter operating in rf-only mode as an ion guide. This mode was mainly used to examine all the species produced from the ESI source. In Mass 2 scan, the second stage mass filter was scanned while the first mass filter was either fixed at a specific m/z or operated as a rf-only ion guide. This was mainly used for measuring product ions from ion-molecule reactions, while the primary ion was selected by the first stage mass filter. In this case, the first mass filter was set at primary ion m/z.

8) **Single Mass mode** Measuring ion intensity at a given m/z position with other parameters fixed is essential to verify the stability and consistence of the ESI source and the mass spectrometer over time. This is also an effective way for troubleshooting.

During experiments, Mass 1 scan and Mass 2 scan were performed initially to determine m/z positions of primary and product ions, followed by PB1 and PB2 optimization to improve ion transmission. Once these values were optimized, ΔRes1 and ΔRes2 were scanned and optimized accordingly. Subsequently, E_0 was determined before running ion-molecule experiments at various collision energies.

During mass scan, in order to avoid contamination from previous counts, a period of 0.1 second was implanted between each two scan steps. This period allows the time for the change of mass command voltage, while the counter stopped counting. This implementation ensured the ion counts collected by LabVIEW program represent the true counts at each m/z position.

2.4.2 IMR.vi

IMR.vi was designed to measure ion-molecule reaction cross sections, and adopted all parameters optimized by *MassScan.vi*. It was capable of precisely controlling the collision energy and the pressure of neutral collision gas in the scattering cell during ion-molecule reactions. Figure 2.3 depicts the front panel of the program.

IMR.vi only executed one type of task, i.e., collecting ion intensities at designated reactant and product m/z positions alternatively while varying the collision energies E_{col} with other parameters fixed at certain values. Prior to experiments, ion mode was selected on the front panel. Parameters, including: E_0, PB1, PB2, MS1 (reactant ion), MS2 (for reactant and product ions), ΔRes1, and ΔRes2, were determined previously by *MassScan.vi*.

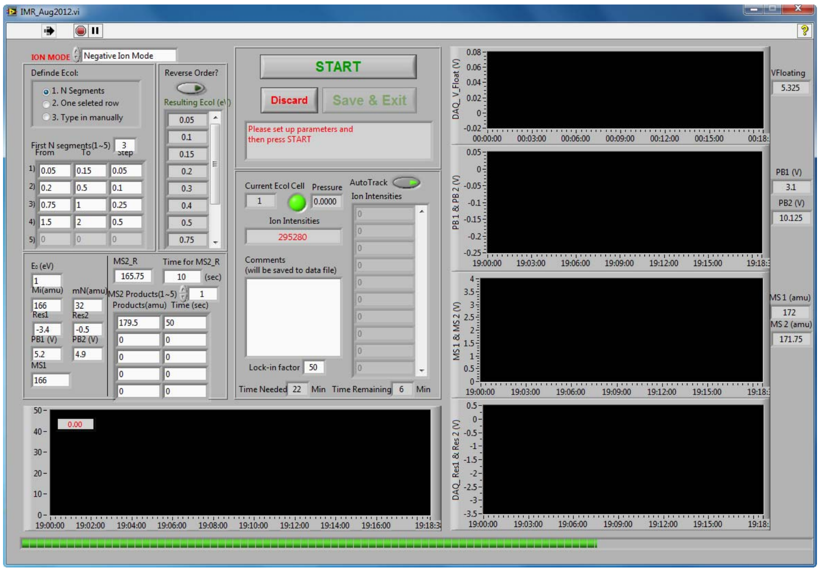

ION MODE: Negative Ion Mode

Definde Ecol:
● 1. N Segments
○ 2. One seleted row
○ 3. Type in manually

First N segments(1~5): 3

	From	To	Step
1)	0.05	0.15	0.05
2)	0.2	0.5	0.1
3)	0.75	1	0.25
4)	1.5	2	0.5
5)	0	0	0

Reverse Order?

Resulting Ecol (eV): 0.05, 0.1, 0.15, 0.2, 0.3, 0.4, 0.5, 0.75

Please set up parameters and then press START

E_0 (eV): 1
Mi(amu): 166
mN(amu): 32
Res1: -3.4
Res2: -0.5
PB1 (V): 5.2
PB2 (V): 4.9
MS1: 166

MS2_R: 165.75
Time for MS2_R: 10 (sec)
MS2 Products(1~5): 1

Products(amu)	Time (sec)
179.5	50
0	0
0	0
0	0
0	0

Current Ecol Cell: 1
Pressure: 0.0000
Ion Intensities: 295280
AutoTrack
Ion Intensities: 0, 0, 0, 0, 0, 0, 0, 0, 0, 0
Comments (will be saved to data file)
Lock-in factor: 50
Time Needed: 22 Min
Time Remaining: 6 Min

0.00

VFloating: 5.325
PB1 (V): 3.1
PB2 (V): 10.125
MS 1 (amu): 172
MS 2 (amu): 171.75

Figure 2.3 Front panel of the LabVIEW program *IMR.vi*

In each experiment, up to five different product ions could be detected for cross section measurements. And the dwell time for reactant and each product ions could be varied individually.

Collision energies can be set up in divided segments. For example, E_{col} of 0.05, 0.1, 0.2, 0.3, 0.4, 0.5, 0.75, 1.0 eV could be divided into three segments:

- ❖ Segment 1: from 0.05 to 0.1 eV, step 0.05 eV
- ❖ Segment 2: from 0.2 to 0.5 eV, step 0.1 eV
- ❖ Segment 3: from 0.75 to 1.0 eV, step 0.25 eV

The resulting E_{col} array was displayed on the front panel once the program started.

During scan, the first mass filter was fixed at the m/z of the primary ion. All E_{col} was looped through sequentially. Measurement at each E_{col} was divided into two sections, scattering cell on (i.e. neutral reactant gas was directed into scattering cell) followed by scattering cell off (i.e. neutral reactant gas was directed to the chamber). During each section, primary ion intensities and product ion intensities were measured individually over pre-set dwell time, as illustrated by the sequence in Figure 2.4.

E_{col}			
Scattering Cell ON		Scattering Cell OFF	
reactant	product1 → product2 → product3 → …	reactant	product1 → product2 → product3 → …

Figure 2.4 A sequence of measurements at each E_{col}

The measured ion intensities for each m/z were listed in the “Ion Intensities” table on the front panel. The AO control voltages for Floating Voltage, PB1/PB2, ΔRes1/ΔRes2, Mass command 1/Mass command 2 were monitored in real time by various AIs. The current E_{col} and the status of the scattering cell (i.e. ON or OFF) were also indicated on the front panel, and updated in real time. Comments by users could be typed in anytime during the experiment, which was also saved to the data file.

References

1 National Instruments, 2012 <http://www.ni.com/>.
2 NI M-series DAQmx manual , National Instruments, <http://www.ni.com/pdf/manuals/371022k.pdf>.
3 Manual for 150-QC quadrupole power supply, ABB Extrel, 1997.

Chapter 3

NaAOT Reverse Micelles in the Gas Phase: Formation and Structures

3.1 Introduction

Sodium bis(2-ethylhexyl)sulfosuccinate (NaAOT) is an ionic surfactant, with two branched alkyl chains as shown in Figure 3.1. It is well suited to form stable reverse micelles in apolar solvents. With surfactant hydrophilic polar heads oriented around an approximately spherical, nanoscopic internal core and hydrophobic alkyl chains forming the outer surface, reverse micelles represent polar microenvironments. In practice, NaAOT reverse micelles are widely used in chemical and biophysical work for solubilization, separation, catalysis, drug delivery, nanoparticle synthesis, and generating membrane-mimetic systems.[1-3]

In contrast with enormous work devoted to NaAOT aggregates in solution, only a handful of investigations have been reported concerning NaAOT aggregates as charged species in the gas phase,[4-12] including electrospray ionization (ESI) and matrix-assisted laser desorption/ionization (MALDI) mass spectra,[6, 10] time-of-flight secondary ion mass spectra[12] and infrared multiple photon dissociation spectra[9] of singly and doubly positively charged NaAOT aggregates. These measurements revealed reverse micelle-like structures for these aggregates. Parallel to experimental advances, molecular dynamics (MD) simulations have demonstrated that NaAOT reverse micelle remains stable *in vacuo*,[13-15] with apolar tails collapsing on the outer surface to make the structure more compact.[13]

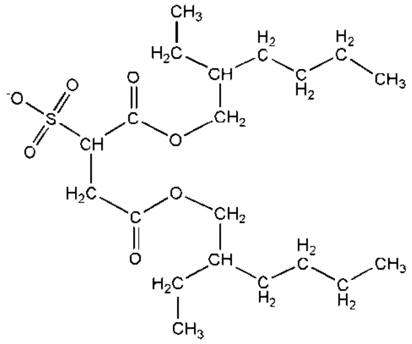

Figure 3.1 Skeletal formula of bis(2-ethylhexyl) sulfosuccinate anion (AOT^-).

In this chapter, the formation of positively multiply charged NaAOT aggregates in the gas phase is reported using ESI mass spectrometry. Collision induced dissociation (CID) was employed to determine their structures.[4] It was found that, positively charged NaAOT aggregates adopted a reverse micelle-like structure in the gas phase, with compositions of $[Na_{n+z}AOT_n]^{z+}$ ($z = 1 - 5$). High charge states allowed the observation of much larger aggregation numbers ($n = 2 - 44$) than those reported in literature.[13, 16-18] Multiply charged $[Na_{n+z}AOT_n]^{z+}$ was able to accommodate guest amino acid molecules. CID of mass-selected reverse micellar ions with Xe was performed to verify reverse micelle-like structures of gas-phase micellar assemblies, and determine the preferential incorporation site of amino acid.

3.2 Experimental

Instruments and materials The experiments were carried out using our mass spectrometer operated in positive ion mode. Both quadrupole mass filters used Extrel 9.5 mm diameter tri-filter rods operating at 880 kHz (Extrel model 150 QC) to cover the m/z range from 10 to 4,000.

The molar masses, purities, manufacturers and storage of chemicals and solvents used in the experiment are listed in appendix C. All chemicals were used without further purification.

NaAOT ($C_{20}H_{37}NaO_7S$, 444.56g•mol^{-1}, stored over P_2O_5 in a desiccator) reverse micelles were prepared in anhydrous hexane containing 2.0×10^{-3}, 5.0×10^{-3} and 10×10^{-3} M NaAOT, respectively. These concentrations are above the CMC of NaAOT in hexane (1.1×10^{-3} M).[19] To verify the influence of pre-formed micelles in solution on gas-phase aggregates, another NaAOT solution was prepared at a concentration of 0.5×10^{-3} M, below the CMC. Water was added to the solution to achieve different water-to-AOT molar ratios ω_0, and the solution was sonicated for 10 minutes to create a transparent reverse micellar solution. The conductivity of the solution was measured using a YSI model 34 conductance meter.

In experiments, the sample solution was sprayed into the ambient atmosphere through an electrospray needle using a syringe pump at a constant flow rate of 0.04 ml•hr^{-1}. The electrospray needle was biased at 3,000 V relative to ground. Positively charged droplets formed from the electrospray needle were fed into the heated desolvation capillary. Initial radii of spray droplets were estimated to be ~ 0.6 μm.[20-22] Assuming solvent evaporates uniformly from the droplet surface, the time for hexane evaporation was estimated at less than 0.5 ms.[23] The distance between the electrospray needle tip and the sampling orifice of the capillary was ~1 cm. The capillary was biased at 70 V relative to ground and heated to 150 °C. Charged liquid droplets underwent desolvation as they passed through the heated capillary, converting to gas-phase ions. A skimmer was located 5 mm from the capillary end, and was biased at 10 V relative to ground. Ions that emerged from the skimmer were passed into a rf hexapole ion guide at a pressure of 10 mTorr, leading to collisional focusing.[24-26] Ions subsequently passed into a set of entrance focusing lenses followed by a quadrupole mass filter. Mass-selected ions were then injected into a rf octopole ion guide which trapped ions in the radial direction. The octopole ion guide operated at 2.6 MHz with a peak-to-peak amplitude of 700 V. DC bias voltage was applied to the ion guide, with amplitude varied from –500 to +500 V. The octopole passed through a scattering cell containing the collision gas Xe at ~ 0.01 mTorr. Precursor ions and their fragment ions were collected by the octopole ion guide, and directed to the second mass spectrometer for mass analysis. Ion signals were counted using a pulse-counting electron multiplier.

CID measurements Assuming gas-phase micelles are spherical, a micelle made of 20 NaAOT molecules has a radius of ~19 Å. The collision cross section of this micelle with Xe was estimated to be 1300 Å^2. To keep multiple collision effects to an insignificant level, the pressure of Xe in the scattering cell was maintained at 0.010 – 0.013 mTorr during CID cross section measurements. In this pressure range, the probability of a single collision between a micellar ion and Xe was ~15%, and that of double collisions was < 4%. The majority of micellar ions (> 81%) passed through the scattering cell without interacting with Xe at all.

Numerous dissociation channels and product ions of various mass and charge were produced from CID of multiply charged ions. The difficulty of measuring cross sections for individual channels is rationalized as follows. 1) Due to the low Xe pressure, intensities of product ions were too low to achieve a good signal-to-noise ratio. 2) Because CID of multiply charged precursor ions accompanied charge separation,[21, 27, 28] some product ions possessed m/z which was beyond the mass spectrometer detection limit (i.e., 4000). 3) For the given octopole rf frequency (f) and amplitude (V_{rf}), only ions with radial velocities up to well-defined cutoff values can be confined by the octopole.[29] At high E_{col}, light product ions may have high radial velocities. In order for these ions to have stable trajectories, the rf frequency should be large enough that the field changes polarity frequently on the time scale of the ions' radial motion in the octopole. On the other hand, the magnitude of the effective potential (U_{eff}) confining the ions' radial motion is proportional to V_{rf}/mf^2. High frequency dictates high V_{rf}; however, there are V_{rf} limits set by arcing, and high V_{rf} also tends to exacerbate the breakdown of adiabaticity.[29] For the mass ratios in this system, it is difficult to avoid loss of some product ions at high E_{col}. For these reasons, only total CID cross sections were measured by the loss of primary micellar ions at each E_{col}.

Because of the low measured ion intensities, it is important to minimize systematic variation in experimental conditions that might be caused by drifting potentials, change in ion beam intensities, etc. In experiments, different E_{col} were cycled through several times. RPA measurements of precursor ions were performed before and after each experiment to check the initial kinetic energy of the primary ion beam. The entire experiment was repeated several times to ensure the reproducibility.

3.3 Results and discussion

3.3.1 Mass spectra of NaAOT/water/hexane reverse micellar solutions

Figure 3.2 depicts the mass spectra obtained by ESI of NaAOT/water/hexane reverse micellar solutions with varying values of ω_0. Gas-phase aggregates have the composition of $[(NaAOT)_nNa_z]^{z+}$, within the instrument detection range (m/z = 1 – 4,000). Each aggregate hosts extra Na^+ ions (in addition to AOT counter ions), which account for its overall charge. Assignments of mass peaks are based on their aggregation numbers (n) and charges (z), and the labels for the same charge states are grouped together. In the following discussion the aggregates are indicated as n/z for convenience. The most intense mass peaks in Figures 3.2a and 3.2b are attributed to the singly charged species, of which 5/1 and 6/1 are the strongest, and the relative abundance of aggregates decreases with increasing aggregate size and charge. A series attributed to singly charged $[(NaAOT)_nH]^+$ is identified in Figures 3.2a and 3.2b, of which one Na^+ is substituted for a proton. But the intensities of $[(NaAOT)_nH]^+$ are much lower compared to corresponding $[(NaAOT)_nNa]^+$.

It was found that, the distributions of gas-phase NaAOT aggregate size, and therefore charge, are strongly dependent on the values of ω_0, and heavier aggregates form upon increasing ω_0, as demonstrated in Figures 3.2a and 3.2b. At $\omega_0 = 0 - 5$ (mass spectrum for $\omega_0 = 5$ not shown, but similar to $\omega_0 = 0$), the maximum aggregation number (n_{max}) and charge (z_{max}) are 26 and 3, respectively. The values of n_{max} and z_{max} increase to 35 and 4 at $\omega_0 = 6.5$ (not shown), and to 44 and 5 at $\omega_0 = 10$. The actual values of n_{max} could be larger, since the maximum size at each ω_0 is approaching the detection limit of the mass filter. There is a minimal aggregation number (n_{min}) for each charge state, 2, 4, 8, 14 and 20 for z = 1, 2, 3, 4 and 5, respectively.

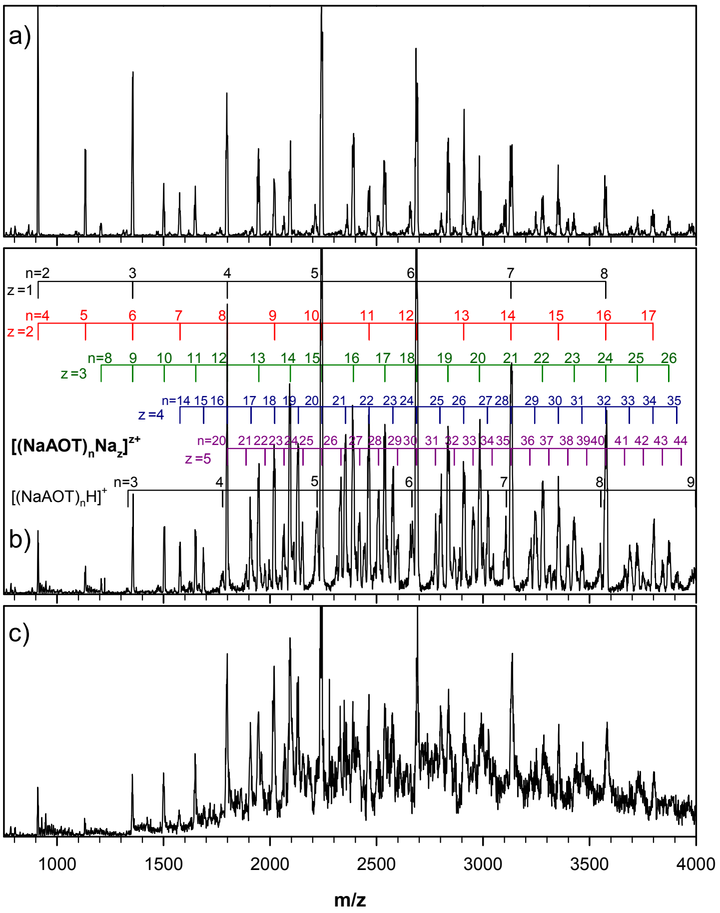

Figure 3.2 ESI mass spectra of NaAOT/water/hexane reverse micellar solutions with different ω_0. [NaAOT] = 5.0×10^{-3} M and a) $\omega_0 = 0$, b) $\omega_0 = 10$, and c) $\omega_0 = 30$.

It is also worth noting that, increasing ω_0 from 10 to 20 does not change the size and charge distribution of gas-phase aggregates. But the abundance of multiply charged species relative to that of singly charged species increases remarkably as ω_0 is progressively increased. When ω_0 exceeds 20, the mass spectra become congested and poorly resolved. The mass spectrum of $\omega_0 = 30$ is shown in Figure 3.2c, with a progressively growing background signal starting at m/z = 1500. A reasonable explanation for the broadened and diffused spectrum at $\omega_0 = 30$ is that the abundance of large, multiply charged micelles increases at high ω_0, and higher charge states are more susceptible to in-source dissociation with residual gas because they have higher collision energies than low charge states at the same acceleration voltage.[30] Another possible contribution to the complexity of mass spectra at extremely high water loading could be attributed to residual water molecules within reverse micelles. Because gas-phase aggregates underwent collisions with air and solvent molecules, portions of small aggregates observed in Figures 3.2a – 3.2c could be yielded from dissociation of large aggregates by sequential losses of AOT and Na^+.

To evaluate the influence of pre-formed micelles in solution on gas-phase aggregates, the NaAOT solutions with various concentrations were prepared in hexane while keeping the value of ω_0 at 10. For solutions containing 2.0×10^{-3}, 5.0×10^{-3}, and 10×10^{-3} M NaAOT (all above the CMC), no difference was found in the distributions of aggregate size and charge, with $n_{max} = 44$ and $z_{max} = 5$ for these solutions. In other words, above the CMC with fixed water content, the NaAOT concentration didn't affect gas-phase aggregates. However, for a solution of 0.5×10^{-3} NaAOT (below the CMC), n_{max} and z_{max} decreased to 26 and 3, respectively.

It is interesting to note that, the dependence of observed n_{max} on ω_0 for gas-phase aggregates is analogous to that for the micellar solution. Dry NaAOT reverse micelles in apolar solvents have an average aggregation number around 20.[13, 31, 32] Aggregation numbers of wet reverse micelles could be estimated using $n = 4\pi r_{core}^2/A_{head}$ and $r_{core} = 1.7\ \omega_0(\text{Å})$,[33] where r_{core} is the radius of the micellar core and A_{head} is the area occupied by each AOT polar head at the interface (0.52 nm^2).[1, 34, 35] Typical values of n in solution are estimated to be 18, 32 and 70 for ω_0 = 5, 6.5, and 10, respectively. The values of observed gas-phase n_{max}, except for ω_0 = 10, are comparable to the corresponding n in solution. The possibility of missing large gas-phase aggregates at m/z > 4,000 could not be ruled out, since theoretical simulations suggest that gas-phase micelles could have more compact structures compared to those in solution.[17] However, it is less likely that the large aggregates would be in high abundance. In summary, the correlation between the size of gas-phase aggregates and ω_0 of ESI solutions — a key property of reverse micelles in solution, implies that gas-phase aggregates retain a memory of starting assembly in solution.

3.3.2 Mass spectra of NaAOT monomers in methanol/water (1:1)

In order to further investigate the effects of solution conditions on the size and charge distribution of gas-phase aggregates, a control experiment was carried out under the same conditions, except a methanol/water (1:1 volume ratio) solution of 1.0×10^{-3} M NaAOT (below CMC in water, 2.0×10^{-3} M[19]) was used. In this case, only aggregates of n = 2 – 26 and z = 1 – 3 were observed, which is similar to the spectrum obtained from a dry AOT/hexane micellar solution (i.e. ω_0 = 0). In addition, the distribution of size and charge is independent of NaAOT concentration in methanol/water, in the range of 0.7×10^{-3} – 5.0×10^{-3} M which was chosen to bracket the CMC of NaAOT.

Although the NaAOT solution was prepared in a similar manner, our ESI mass spectra of NaAOT in methanol/water are somewhat different than those reported by Bongiorno and

Giorgi *et al.*[6-8] Their ESI mass spectra are dominated by singly charged species $[(NaAOT)_nNa]^+$, and doubly and triply charged species are of negligible abundance. Discrepancy is also noted in the shape of ion abundance profiles. In our mass spectra aggregates 5/1 and 6/1 exhibit the highest abundance, while in their mass spectra the trimeric species 3/1 is the base peak. These discrepancies are most likely related to the differences in the ESI operating conditions and instrumentation. In their experiments, ESI was operated at a flow rate of 0.12 – 4.2 $ml \cdot hr^{-1}$ with a nitrogen sheath gas. Their capillary was heated to 230 °C, and mass spectra were measured on an ion-trap mass spectrometer (LCQ DECA, ThermoFinnigan). In contrast, our ESI source was operated at a much lower flow rate (0.04 $ml \cdot hr^{-1}$) and with no sheath gas. The capillary temperature was maintained at 150 °C, and mass spectra were collected on a quadrupole mass spectrometer. Some of these different operating conditions may exert counteracting effects on size and charge distributions. For example, the sheath gas and high capillary temperature used in their experiment increased the evaporation rate and reduced the time available for desorption of ions during stages of low-droplet charge density, which perhaps lead to low ion intensities of lower charge states.[30] On the other hand, their ESI was operated at a higher flow rate, which increased the evaporation time and favored lower charge states. Note that multiply charged NaAOT aggregates are extremely sensitive to the potential between the capillary and the skimmer, because they gain higher translational energies than the lower charge states in the same electrical field. In our experiment, the skimmer was biased at 10 V. Aggregates of $z \geq 3$ achieved the highest intensity at capillary voltage of 70 V, but completely disappeared when the capillary voltage increased to more than 110 V. The capillary-skimmer potential was not indicated in Bongiorno and Giorgi *et al.*'s experiments. It is suspected that the absence of high charge states in their measurements may be due to the significant in-source CID. This comparison implies that ESI and instrumental conditions are another important controlling factor for the distribution of gas-phase aggregates. For this reason, all data in this experiment were collected under the same experimental conditions unless otherwise stated, so that one can focus on effects of solution conditions.

3.3.3 Mass spectrum of NaAOT reverse micelles encapsulating glycine

In this experiment, Gly was added into NaAOT reverse micelle solutions in hexane with ω_0 = 10 (i.e., [NaAOT] = 5.0×10^{-3} M and [Gly] = 1.0×10^{-3} M). Reverse micelles were then introduced to the gas phase via ESI, followed by mass analysis. This simple amino acid was chosen because it facilitated the identification of key factors in gas-phase reverse micelle encapsulation.

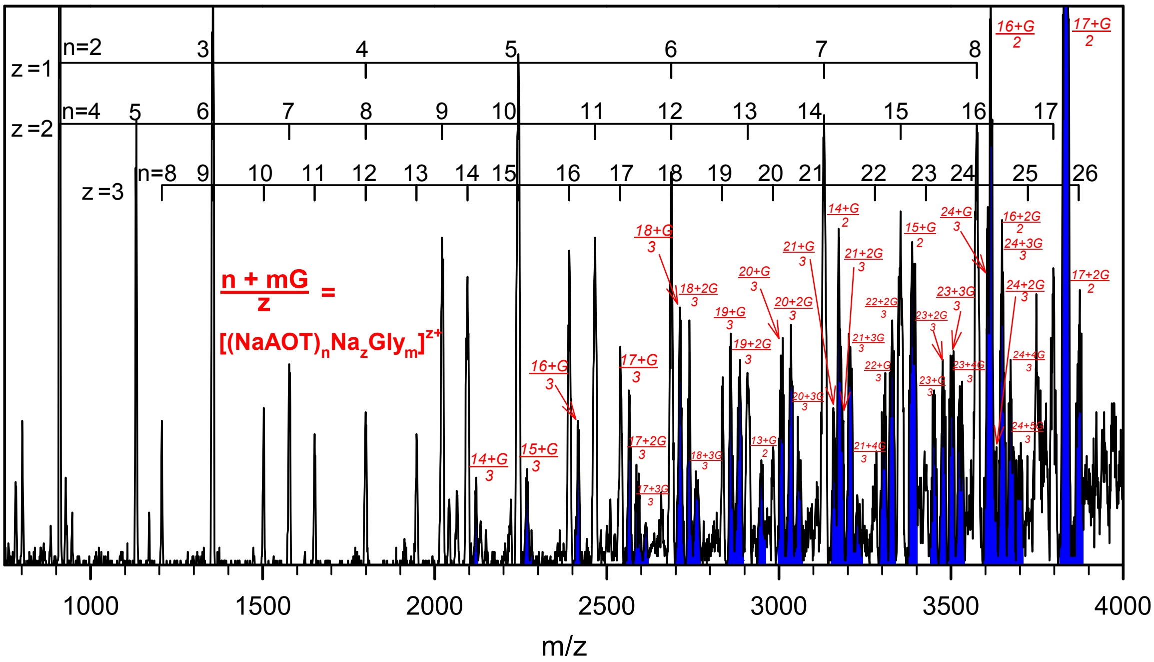

Figure 3.3 ESI mass spectrum of a reverse micellar solution containing 5.0×10^{-3} M NaAOT, 5.0×10^{-2} M H_2O (ω_0 = 10), and 1.0×10^{-3} M glycine in hexane.

Figure 3.3 shows the mass spectrum of Gly-encapsulating NaAOT reverse micelles. In the m/z range below 2,000, mass spectrum of reverse micelles with Gly incorporated is indistinguishable from that of empty reverse micelles shown in Figure 3.2b, which implies that at this m/z range, gas-phase aggregates are unoccupied. Occupied NaAOT aggregates are observed with compositions of $[(\mathrm{NaAOT})_n\mathrm{Na}_z\mathrm{Gly}_m]^{z+}$ in the m/z range above 2,000. These species become prevailing at m/z above 3,000. In the figure, these species are indicated in shaded areas, and labeled as (n+mG)/z. Note that, although Na^+ and/or H^+ can be attached to Gly molecule,[36, 37] no monomers and clusters of sodiated or protonated Gly have been detected, indicating that all Gly molecules are confined within NaAOT aggregates.

Another interesting finding is the strong correlation between the encapsulation capability and the size of gas-phase NaAOT aggregates. For aggregates with aggregation number less than 13, no encapsulation was detected. Aggregates of $n \geq 13$ can entrap one Gly molecule, while those of $n \geq 16$ can entrap two. Up to three Gly molecules can be accommodated in single aggregates of $n \geq 17$, four Gly molecules in those of $n \geq 21$, and five in those of $n \geq 24$. Assuming a spherical reverse micelle-like geometry for NaAOT aggregates, its core diameter D is roughly equal to $\sqrt{n \times A / \pi}$ where A is the area of the AOT polar head (0.52 nm^2). D is calculated to be 1.4, 1.6, 1.7, 1.9, and 2.1 nm for n = 13, 16, 17, 21 and 25, respectively. The size of a Gly molecule is 0.6 – 0.7 nm. Therefore, the maximum number of encapsulated Gly molecules roughly matches the available micellar core size. Among Gly-encapsulating aggregates, (17+G)/2 has the highest abundance, indicating a particularly stable geometric structure for this assembly.

A charge dependence of Gly encapsulation is also found. For example, for occupied aggregates of the same size, doubly charged species have a higher abundance than triply charged ones (e.g. (15+G)/2 vs. (15+G)/3, and (17+G)/2 vs. (17+G)/3), and doubly charged species can entrap more Gly molecules (e.g. (16+G)/2 vs. (16+G)/3). It is also worth noting that upon encapsulation of Gly the intensities of highly charged micelles (i.e. $z > 3$) dramatically decreases, implying that Gly and Na^+ compete for surfactants, and AOT may have a higher affinity for Gly than for Na^+.

These observations deviate from expectations if random associations are assumed between surfactants and Gly molecules. ESI mass spectrometry experiments were performed with proline or tryptophan incorporated into NaAOT reverse micelles, and a similar dependence of encapsulation on micelle size was found. The analysis of tryptophan-encapsulating NaAOT reverse micelles will be discussed in detail in next chapter. These findings strongly support a reverse micelle-like structure for gas phase NaAOT aggregates containing biomolecules in their interior. To emphasize the spatially ordered reverse micelle-like NaAOT aggregates, these aggregates will be referred to as gas-phase reverse micelles (or micellar ions) in the remainder of the chapter.

3.3.4 CID of gas-phase NaAOT reverse micelles

Empty reverse micelles One issue in interpreting CID of NaAOT reverse micellar ions concerns mass coincidences among different charge states. Ion intensities of peaks corresponding to singly charged micellar ions include the shares of all multiply charged ions at the same m/z positions. For example, m/z of 2,687 represents at least four overlapping charge states, 6/1, 12/2, 18/3, and 24/4. For this reason, 13/2, 15/2, 17/2, 16/3, 17/3, 19/3 and 20/3 were chosen as the precursor ions, listed in ascending order of micelle size and charge. Selection of these ions circumvents the complication of mass coincidence with other charge states, and simplifies the interpretation of product ion spectra. In consequence, the dissociation behavior of each micellar ion is clearly revealed. Figure 3.4 shows the product ion spectra from CID of mass-selected micellar ions. To map out all dissociation product ions within the instrument m/z detection limit, date on Figure 3.4 (and on Figure 3.6) were obtained at a relatively high Xe pressure (0.15 mTorr) in the scattering cell, and were accumulated over a long period of time. Many product ions were produced in collisions of these precursor ions with Xe. Because of multiple collisions between precursor ions and Xe at a high gas pressure (and primary fragment ions may continue to undergo collisions that cause them to fragment as well), the relative intensities of product ions in Figure 3.4 do not reflect the branching ratio. However, all product ions in Figure 3.4 were observed under single-collision conditions as well.

Dissociation channels for individual precursor ions are summarized in Table 3.1. Both complementary product ions, produced from a dissociation leading to two charged products, were observed in mass spectra and are included in the table, unless otherwise stated. Dissociation of reverse micelles strongly depends on their charge states. For the doubly charged micellar ions, CID exclusively produces singly charged products. It is interesting to note that the major CID channels for doubly charged micellar ions correspond to divisions of precursor ions into two nearly equally-sized products, e.g., 15/2→8/1+7/1. CID of triply charged micellar ions becomes more complex, and products include both singly and doubly charged ions, as well as small amounts of triply charged ions. Because of overlapping of singly, doubly and triply charged ions, some peaks may actually be attributed to more than one product ion mass. Alternative assignments are indicated using parentheses for some product ions in Figure 3.4. It is possible to produce three singly charged products from CID of triply charged precursor ions; however, these channels cannot be assigned unambiguously and thus are not included in the table.

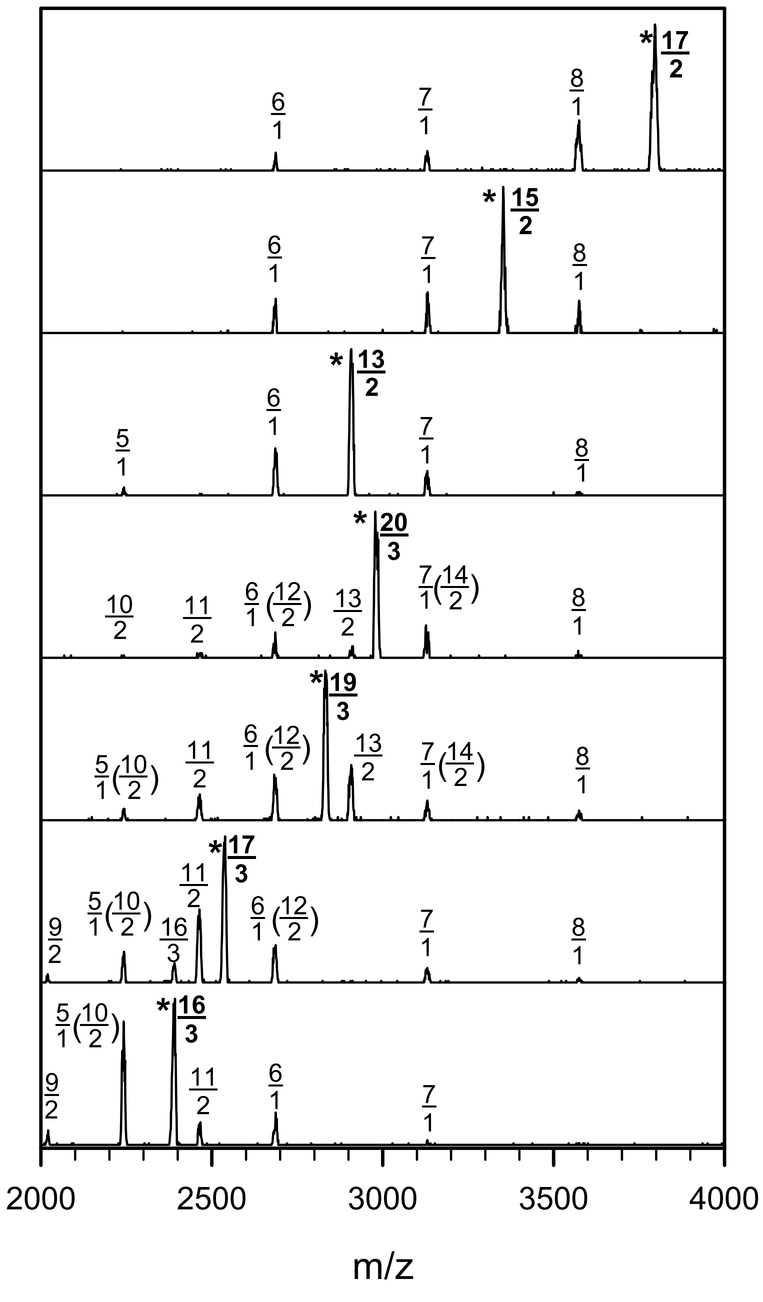

Figure 3.4 CID mass spectra of mass-selected NaAOT reverse micellar ions. Spectra were measured at E_{col} = 1.0 eV for doubly charged ions and E_{col} = 1.5 eV for triply charged ions, with a 0.15 mTorr Xe in the scattering cell. Asterisks indicate precursor ions, and the labels in parentheses are alternative assignments for product ions.

Table 3.1 CID products of gas-phase NaAOT reverse micellar ions

Precursor ions	Dissociation channels	Precursor ions	Dissociation channels
$\frac{13}{2}$	$\frac{8}{1}+\frac{5}{1}$ $\frac{7}{1}+\frac{6}{1}$	$\frac{16}{3}$	$\frac{11}{2}+\frac{5}{1}$ $\frac{10}{2}+\frac{6}{1}$ $\frac{9}{2}+\frac{7}{1}$
$\frac{15}{2}$	$\frac{9^{*}}{1}+\frac{6}{1}$ $\frac{8}{1}+\frac{7}{1}$	$\frac{17}{3}$	$\frac{16}{3}+1$ $\frac{12}{2}+\frac{5}{1}$ $\frac{11}{2}+\frac{6}{1}$ $\frac{10}{2}+\frac{7}{1}$ $\frac{9}{2}+\frac{8}{1}$
$\frac{17}{2}$	$\frac{11^{*}}{1}+\frac{6}{1}$ $\frac{10^{*}}{1}+\frac{7}{1}$ $\frac{9^{*}}{1}+\frac{8}{1}$	$\frac{19}{3}$	$\frac{13}{2}+\frac{6}{1}$ $\frac{14}{2}+\frac{5}{1}$ $\frac{12}{2}+\frac{7}{1}$ $\frac{11}{2}+\frac{8}{1}$ $\frac{10}{2}+\frac{9^{*}}{1}$
		$\frac{20}{3}$	$\frac{14}{2}+\frac{6}{1}$ $\frac{13}{2}+\frac{7}{1}$ $\frac{12}{2}+\frac{8}{1}$ $\frac{11}{2}+\frac{9^{*}}{1}$ $\frac{10}{2}+\frac{10^{*}}{1}$

* beyond the m/z detection limit of the mass spectrometer.

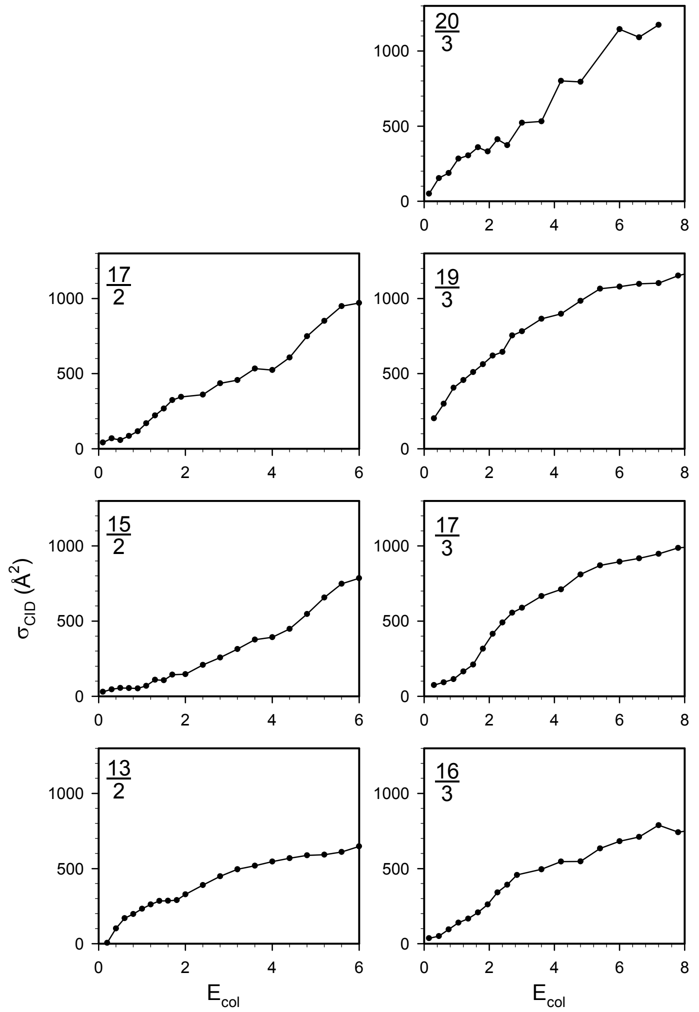

Figure 3.5 CID cross sections of mass-selected NaAOT reverse micellar ions, measured at single collision conditions.

Total CID cross sections (σ_{CID}) for precursor ions are reported in Figure 3.5, in the E_{col} range of 0.1 – 6.0 eV for doubly charged ions and 0.1 – 8.0 eV for triply charged ions. All collision energies are given in the center-of-mass frame. The main points of cross section measurements are as follows: 1) σ_{CID} shows threshold-like behavior at low E_{col} and increases as E_{col} rises. 2) σ_{CID} strongly depends on reverse micelle size. At E_{col} = 6.0 eV, σ_{CID} increases from ~ 600 Å^2 for 13/2, to ~ 950 Å^2 for 17/3, and ~ 1150 Å^2 for 20/3. 3) σ_{CID} is enhanced by the micelle charge. For example, 17/3 has larger σ_{CID} than 17/2 at all collision energies. 4)

σ_{CID} of large micellar ions was compared with their hard-sphere collision cross sections ($\sigma_{\text{hard-sphere}}$) with Xe. At our highest E_{col}, σ_{CID} for 17/3, 19/3, and 20/3 are 1,000 – 1,200 Å^2. Assuming spherical geometries for reverse micellar ions, their hard-sphere collision cross sections are 1,200 – 1,300 Å^2. σ_{CID} is approaching the collision limit at our highest E_{col}. Therefore, at sufficiently high energies, it is expected that nearly every hard sphere collision will lead to dissociation, and σ_{CID} becomes independent of E_{col}.[38] For micellar ions of n < 17, maximum σ_{CID} are smaller than their $\sigma_{\text{hard-sphere}}$. However, it is possible that they have not reached the plateau in close proximity to $\sigma_{\text{hard-sphere}}$ at our highest E_{col}. In any case, σ_{CID} provides a measure of the lowest limit of the average micelle size.

Gly-encapsulating reverse micellar ions Because CID of occupied reverse micelles may involve a competition between stripping surfactants and expelling confined amino acids, it is interesting to compare CID of empty and Gly-encapsulating reverse micellar ions. Such competition should be driven by the precursor ion structure, and by the stability of neutral and charged products formed. To enable a direct comparison, CID of Gly-encapsulating reverse micellar ions were performed using similar sizes and charges of precursor ions to those employed for empty micellar ions, i.e., (13+G)/2, (15+G)/2, (17+G)/2, (16+G)/3, (17+G)/3, (19+G)/3, and (20+G)/3.

Mass spectra of CID product ions for mass-selected reverse micellar ions incorporating Gly is shown in Figure 3.6 and their dissociation channels are summarized in Table 3.2. Occupied reverse micellar ions have distinct dissociation channels from the corresponding empty ones. As listed in Table 3.2, dissociation of occupied reverse micelles produces large product ions, some of which still encapsulate Gly, suggesting that encapsulation of Gly may improve the overall stability of reverse micellar structures. The smallest stripped micellar ion still capable of hosting a Gly molecule is (13+G)/2, similar to what was observed in the mass spectrum of Gly-encapsulating reverse micelles (Figure 3.3). Figure 3.6 also shows that, under the same conditions, (17+G)/2 yields less dissociation than other precursor ions. It follows that (17+G)/2 has higher stability, again in agreement with ESI mass spectral results. σ_{CID} for Gly-encapsulating reverse micellar ions are shown in Figure 3.7. Generally, occupied micellar ions have similar or slightly higher σ_{CID} than empty micellar ions. Consistent with its high stability, (17+G)/2 has a smaller σ_{CID} than all other precursor ions except (13+G)/2.

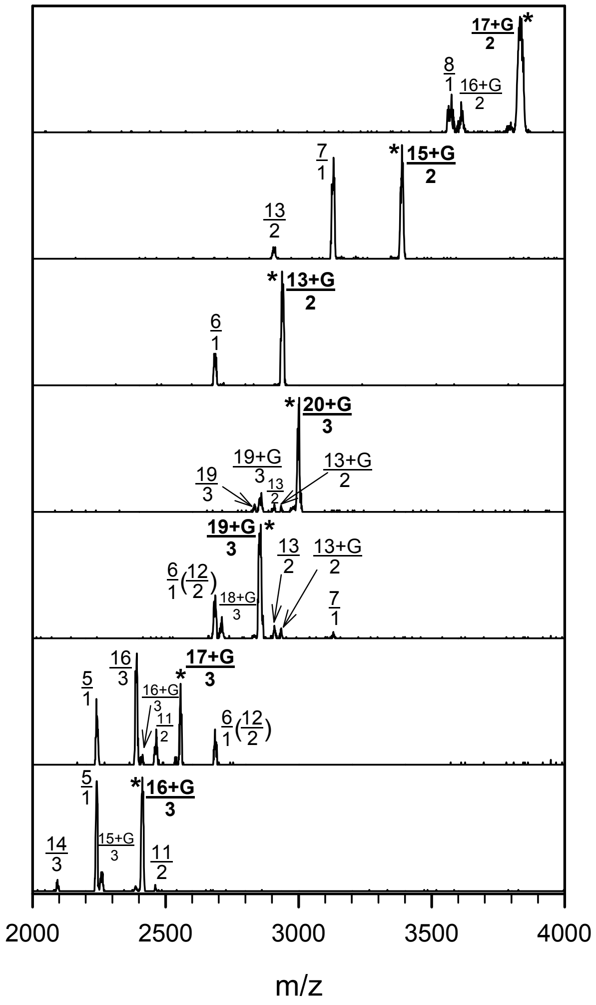

Figure 3.6 CID mass spectra of mass-selected NaAOT reverse micellar ions encapsulating Gly. Spectra were measured at E_{col} = 1.0 eV for doubly charged ions and E_{col} = 1.5 eV for triply charged ions, with a 0.15 mTorr Xe in the scattering cell. Asterisks indicate precursor ions, and the labels in parentheses are alternative assignments for product ions.

Table 3.2 CID products of gas-phase NaAOT reverse micellar ions encapsulating Gly

Precursor ions[a]	Dissociation channels	Precursor ions[a]	Dissociation channels
$\frac{13+G}{2}$	$\frac{7}{1}$(not detected) $+\frac{6}{1}+G$	$\frac{16+G}{3}$	$\frac{15+G}{3}+1$ $\frac{14}{3}+2+G$ $\frac{11}{2}+\frac{5}{1}+G$
$\frac{15+G}{2}$	$\frac{13}{2}+2+G$ $\frac{8}{1}$(not detected) $+\frac{7}{1}+G$	$\frac{17+G}{3}$	$\frac{16+G}{3}+1$ $\frac{16}{3}+1+G$ $\frac{12}{2}+\frac{5}{1}+G$ $\frac{11}{2}+\frac{6}{1}+G$
$\frac{17+G}{2}$	$\frac{16+G}{2}+1$ $\frac{8}{1}+\frac{9}{1}+G^{b}$	$\frac{19+G}{3}$	$\frac{18+G}{3}+1$ $\frac{13+G}{2}+\frac{6}{1}$ $\frac{13}{2}+\frac{6}{1}+G$ $\frac{12}{2}+\frac{7}{1}+G$
		$\frac{20+G}{3}$	$\frac{19+G}{3}+1$ $\frac{19}{3}+1+G$ $\frac{13+G}{2}+\frac{7}{1}$ $\frac{13}{2}+\frac{7}{1}+G$

[a] the precursor and product ions are indicated as $\frac{n+mG}{z}$, where n is the aggregation number, z is the charge and m is the number of encapsulated glycine molecules.

[b] $\frac{9}{1}$ is beyond the mass/charge detection limit of the mass spectrometer.

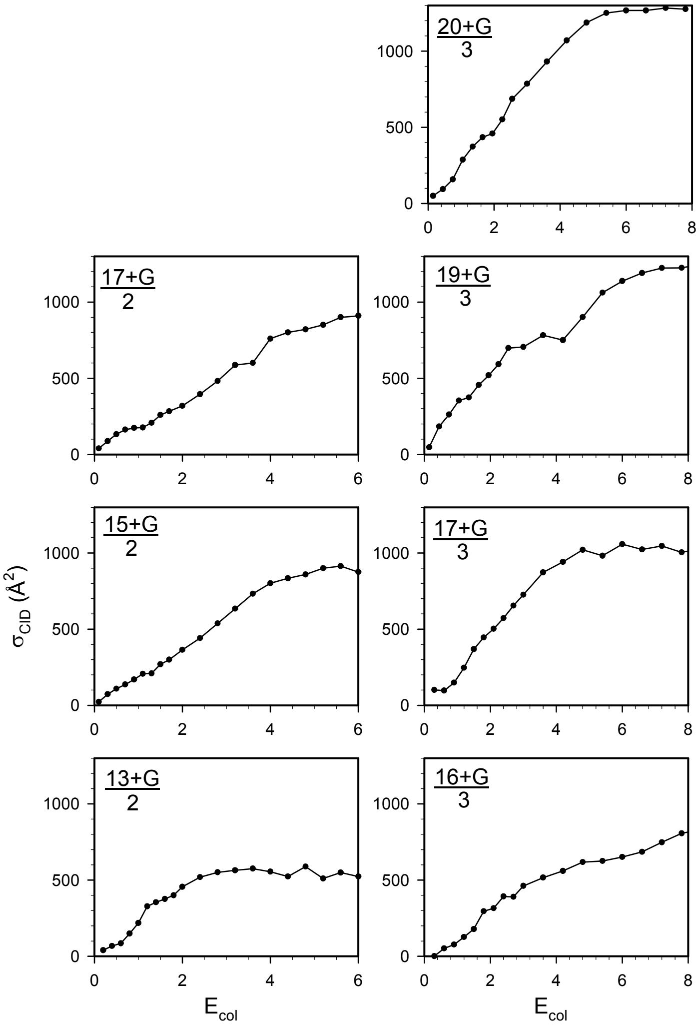

Figure 3.7 CID cross sections of mass-selected NaAOT reverse micellar ions encapsulating Gly, measured at single collision conditions.

3.3.5 Dependence of gas-phase reverse micelle size and charge on solution conditions

An understanding of the reverse micelle formation mechanism in the ESI process provides insights into the interpretation of effects of solution conditions. In conventional ESI mass spectrometry, the charge state of ions is determined by the charge density at the droplet surface.[30] Initial radius (R) and charge (q) of the droplets produced by electrospray can be estimated as [20-22]

$$R = \left(V_f \varepsilon / K\right)^{1/3} \qquad (1)$$

$$q = 0.7[8\pi(\varepsilon_0 \gamma R^3)^{1/2}] \qquad (2)$$

where ε and ε_0 are the permittivity of the solvent and the vacuum, respectively, γ is the surface tension of the solvent, and K is the conductivity of the solution. Based on these relationships, droplet radius and charge are predicted to be 0.59 – 0.62 μm and $2.1 - 2.2 \times 10^4$ for NaAOT ($0.5 - 5.0 \times 10^{-3}$ M)/water ($\omega_0 = 10$)/hexane, 0.92 μm and 5.4×10^4 for NaAOT (1.0×10^{-3} M) in methanol/water, and 0.6 μm and 2.8×10^4 for NaAOT (5.0×10^{-3} M) in methanol/water. The predicted values of R and q reveal that, neither the solvent nor the NaAOT concentration itself changes the charge density at droplet surface to a significant extent. Therefore, it is less likely that the charge density at droplet surface is responsible for formation of highly charged micellar ions (i.e. $z > 3$). Different charge distributions from different solutions must be related to the aggregate structures in solution.

One critical aspect of our experiment is whether large reverse micelles exist in the starting solution. For NaAOT/water/hexane solutions above the CMC, surfactants tend to form reverse micelle aggregates. When transferred from solution to the gas phase, reverse micelles may be able to preserve their structures, at least to some extent. In contrast, NaAOT cannot form micelles below the CMC. Neither can NaAOT form large micelles in anhydrous hexane or methanol/water. As a result, in the latter three cases, self-assembling of NaAOT into large reverse micelles has to take place in the gas phase between electrospray and exposure to a high vacuum, and the small size of gas-phase reverse micelles are tentatively attributed to the fact that surfactants have a low concentration in the vapor state. Bongiorno *et al.* concluded a similar formation mechanism for methanol/water solution.[6] In sum, two approaches were adopted for producing gas-phase reverse micelles, one utilizes NaAOT/water/hexane micellar solutions, and the other uses hexane or methanol/water solutions of monomeric NaAOT. While both cases may involve self-assembling of NaAOT in the gas phase, the micellar solution certainly helps formation of large gas-phase aggregates. CID of the same micellar ions prepared with different approaches resulted in similar product ions, suggesting that the micellar structures are independent of the approach used for preparation.

It may be argued that multiply charged aggregates are not stable in a reverse micelle-like structure, because the micellar core has to host extra counter ions, and there is coulombic repulsion when the charges are too close to each other inside the core.[6] However, based on direct optimization of dry, isolated NaAOT reverse micelles,[13] and molecular dynamics simulations of low ω_0 NaAOT reverse micelles in isooctane,[39, 40] most Na^+ ions penetrate the layer of AOT polar heads where the Na^+ ions coordinate with the sulfonate group. Some Na^+ can exist outside, where they coordinate with the carbonyl group of AOT.[40] Mulliken charge analysis of AOT anion was performed at the B3LYP/6-31+G(d,p) level of theory using Gaussian 03.[41] Each sulfonate oxygen atom has a Mulliken charge close to or exceeding –0.6, and each carbonyl oxygen atom has a Mulliken charge close to –0.5. Na^+ may be able to interact with sulfonate and/or carbonyl oxygen atoms belonging to different AOT.[6] Therefore, from the point of view of electrostatic interactions, coordination of Na^+ with these oxygen atoms offers favorable structures for multiply charged reverse micelles, and could become one of important forces controlling aggregation. It is conceivable that for large reverse micelles, one single extra Na^+ is unable to interact with all AOT. Therefore, to stabilize the micellar structure, more Na^+ ions are needed as the “gluing” agent between adjacent AOT. This hypothesis is supported by the fact that triply charged micellar ions generally are more stable and have higher intensities than doubly charged ions, as shown in Figure 3.2b.

3.3.6 Is water necessary for reverse micelles?

In solution phase, confined, ordered water molecules exist inside the reverse micelle core.[42-45] Nanoscale water droplets are assumed to promote the aggregation of amphiphilic surfactants around the micellar core. Surprisingly, water molecules are absent in most gas-phase reverse micellar ions, with the exception of small aggregates where n = 2 – 5, in which a progression of water adducts were formed. Loss of water was also found from gas-phase reverse micelles which incorporate Gly and other amino acid molecules. As demonstrated in present and previous experiments,[6-8] losing water does not affect the stability of gas-phase NaAOT reverse micelles. Theoretical simulations[6,46] also suggest that the stability of reverse micellar structure in the vacuum is independent of water. Moreover, the structure of a dry, isolated AOT reverse micelle with a central void has been proposed by direct optimization.[13]

Loss of water was also observed in gas-phase CTAB reverse micelles[47] and was interpreted in terms of dissociation upon collisions.[48] While collision activated dissociation could be a main reason for water loss, other factors may also contribute such as low temperature-induced water shedding. Flynn and co-workers reported NMR studies of low temperature-induced water shedding from NaAOT reverse micelles composed of a low ionic strength aqueous core.[49, 50] They found that at a temperature of -30 °C most of the encapsulated water is lost from the core, leaving the micelles nearly dry. The explanation is that encapsulation of water molecules into NaAOT reverse micelles is a spontaneous process (i.e. $\Delta G = \Delta H - T\Delta S < 0$). Since insertion of water in NaAOT reverse micelles is an endothermic process (unfavorable from an enthalpic point of view), the positive change of the system enthalpy (ΔH) must be compensated by a positive change of the system entropy (ΔS).[50-52] However, as temperature decreases and water becomes supercooled, enthalpy dominates the system and the micelles expel water molecules. Similarly, in ESI experiments, evaporation of solvent from electrospray droplets results in cooling of reverse micelles before they enter the capillary and may cause exclusive loss of water. As water sheds, the size of the reverse micelles naturally decreases, leading to stronger interactions between Na^+ ions and sulfonate/carbonyl groups of AOT.

One interesting question would be, how are Gly molecules entrapped in gas-phase NaAOT reverse micelles? Gly could be randomly attached to the micellar surface, or entangled with AOT hydrophobic tails. This is further explored and discussed in the next chapter.

3.4 Conclusions

In this chapter, the formation and characterization of positively multiply charged NaAOT micelles in the gas phase is presented using our ESI guided-ion beam tandem mass spectrometer. It was found that, positively charged NaAOT gas-phase micelles tend to adopt reverse micelle-like structure, with the compositions of $[Na_{n+z}AOT_n]^{z+}$ with $z = 1 - 5$ and $n = 2 - 44$. The dependence of gas-phase reverse micelle sizes and charges on starting solutions was observed, which suggested that, in addition to self-assembling of surfactants in the gas-phase, pre-formed micelles in solution may preserve reverse micellar structure when transferred to the gas phase (at least to some extent) and thus help form large gas-phase aggregates.

Another most interesting finding from our experiment is that gas-phase NaAOT reverse micelles could encapsulate guest molecules, and thus act as nanometer-sized carriers of biomolecules in the gas phase. The encapsulation and selective transport of amino acid molecules were further explored and will be discussed in detail in the next chapter.

References

1 P. L. Luisi, M. Giomini, M. P. Pileni, and B. H. Robinson, *Biochim. Biophys. Acta,* 1988, 947, 209-246.

2 K. Kon-no, *Surface Colloid Sci.,* 1993, 15, 125-151.

3 M.-P. Pileni, *Natural Materials,* 2003, 2, 145-150.

4 Y. Fang, A. Bennett, and J. Liu, *Int. J. Mass Spectrom.,* 2010, 293, 12-22.

5 Y. Fang, A. Bennett, and J. Liu, *Phys. Chem. Chem. Phys.,* 2011, 13, 1466-1478.

6 D. Bongiorno, L. Ceraulo, A. Ruggirello, V. T. Liveri, E. Basso, R. Seraglia, and P. Traldi, *J. Mass Spectrom.,* 2005, 40, 1618-1625.

7 G. Giorgi, L. Ceraulo, and V. T. Liveri, *J. Phys. Chem. B,* 2008, 112, 1376-1382.

8 G. Giorgi, E. Giocaliere, L. Ceraulo, A. Ruggirello, and V. T. Liveri, *Rapid Comm. Mass Spectrom.,* 2009, 23, 2206-2212.

9 G. Giorgi, L. Ceraulo, G. Berden, J. Oomens, and V. T. Liveri, *J. Phys. Chem. B,* 2011, 115, 2282-2286.

10 D. Bongiorno, L. Ceraulo, G. Giorgi, S. Indelicato, and V. T. Liveri, *J. Mass. Spectrom.,* 2011, 46, 1263-1268.

11 L. Ceraulo, G. Giorgi, V. T. Liveri, D. Bongiorno, S. Indelicato, F. Di Gaudio, and S. Indelicato, *European Journal of Mass Spectrometry,* 2011, 17, 525-541.

12 S. A. Burns, P. L. Valint, Jr., and J. A. Gardella, Jr., *Langmuir,* 2009, 25, 11244-11249.

13 A. I. Bulavchenko, A. F. Batishchev, E. K. Batishcheva, and V. G. Torgov, *J. Phys. Chem. B,* 2002, 106, 6381-6389.

14 G. Longhi, S. L. Fornili, V. T. Liveri, S. Abbate, D. Rebeccani, L. Cerauloe, and F. Gangem, *Phys. Chem. Chem. Phys.,* 2010, 12, 4694-4703.

15 G. Longhi, S. Abbate, L. Ceraulo, A. Ceselli, S. L. Fornili, and V. T. Liveri, *Phys. Chem. Chem. Phys.,* 2011, 13, 21423-21431.

16 N. P. Barrera, N. D. Bartolo, P. J. Booth, and C. V. Robinson1, *Science,* 2008, 321, 243-246.

17 R. Allen, S. Bandyopadhyay, and M. L. Klein, *Langmuir,* 2000, 16, 10547-10552.

18 R. Neutze, R. Wouts, D. v. d. Spoe, E. Weckert, and J. Hajdu, *Nature,* 2000, 406, 752-757.

19 K. Mukherjee, S. P. Moulik, and D. C. Mukherjee, *Langmuir,* 1993, 9, 1727-1730.

20 J. F. D. L. Mora, *J. Fluid Mech.,* 1992, 243, 561-574.

21 J. S. Klassen, Y. Ho, A. T. Blades, and P. Kebarle, *Adv. Gas-Phase Ion Chem.,* 1998, 3, 255-318.

22 P. Kebarle, *J. Mass Spectrom.,* 2000, 35, 804-817.

23 S. E. Rodriguez-Cruz, J. T. Khoury, and J. H. Parks, *J. Am. Soc. Mass Spectrom.,* 2001, 12, 716-725.

24 R. M. Moision, and P. B. Armentrout, *J. Am. Soc. Mass Spectrom. ,* 2007, 18, 1124-1134.

25 A. N. Krutchinsky, I. V. Chernushevich, V. L. Spicer, W. Ens, and K. G. Standing, *J. Am. Soc. Mass Spectrom.,* 1998, 9, 569-579.

26 D. J. Douglas, and J. B. French, *J. Am. Mass Spectrom.,* 1992, 3, 398-408.

27 S. A. McLuckey, G. L. Glish, and G. J. V. Berkel, *Anal. Chem.,* 1991, 63, 1971-1978.

28 J. James L. Stephenson, and S. A. McLuckey, *Anal. Chem.,* 1998, 70, 3533-3544.

29 D. Gerlich, 'Inhomogeneous RF fields: A versatile tool for the study of processes with slow ions', in *State-Selected and State-to-State Ion-Molecule Reaction Dynamics. Part I. Experiment*, ed. by C. Y. Ng and M. Baer (New York: John Wiley & Sons, Inc., 1992), pp. 1-176.

30 G. Wang, and R. B. Cole, 'Solution, gas-phase, and instrumental parameter influences on charge-state distributions in electrospray ionization mass spectrometry', in *Electrospray Ionization Mass Spectrometry: Fundamentals, Instrumentation, and Applications*, ed. by Richard B. Cole (New York: John Wiley & Sons, Inc, 1997), pp. 137-174.

31 M. Ueda, and Z. A. Schelly, *J. Colloid Interface Sci.,* 1988, 124, 673-676.

32 M. Ueda, and Z. A. Schelly, *Langmuir,* 1988, 4, 653-655.

33 M. E. Leser, and P. L. Luisi, *Chimia,* 1990, 44, 270-282.

34 A. M. Maitra, and P. K. Patanjali, in *Surfactants in Solution*, ed. by K. L. Mittal and P. Bothorel (New York: Plenum Press, 1986), p. 581.

35 R. M. Lemert, R. A. Fuller, and K. P. Johnston, *J. Phys. Chem.,* 1990, 94, 6021-6028.

36 R. M. Moision, and P. B. Armentrout, *J. Phys. Chem. A,* 2002, 106, 10350-10351-10362.

37 S. J. Ye, R. M. Moision, and P. B. Armentrout, *Int. J. Mass Spectrom.,* 2005, 240, 233-248.

38 J. Liu, B. Van Devener, and S. L. Anderson, *J. Chem. Phys.,* 2002, 116, 5530-5543.

39 J. Faeder, and B. M. Ladanyi, *J. Phys. Chem. B,* 2000, 104, 1033-1046.

40 J. Chowdhary, and B. M. Ladanyi, *J. Phys. Chem. B,* 2009, 113, 15029-15039.

41 M. J. Frisch, G. W. Trucks, H. B. Schlegel, G. E. Scuseria, M. A. Robb, J. R. Cheeseman, J. J. A. Montgomery, T. Vreven, K. N. Kudin, J. C. Burant, J. M. Millam, S. S. Iyengar, J. Tomasi, V. Barone, B. Mennucci, M. Cossi, G. Scalmani, N. Rega, G. A. Petersson, H. Nakatsuji, M. Hada, M. Ehara, K. Toyota, R. Fukuda, J. Hasegawa, M. Ishida, T. Nakajima, Y. Honda, O. Kitao, H. Nakai, M. Klene, X. Li, J. E. Knox, H. P. Hratchian, J. B. Cross, V. Bakken, C. Adamo, J. Jaramillo, R. Gomperts, R. E. Stratmann, O. Yazyev, A. J. Austin, R. Cammi, C. Pomelli, J. W. Ochterski, P. Y. Ayala, K. Morokuma, G. A. Voth, P. Salvador, J. J. Dannenberg, V. G. Zakrzewski, S. Dapprich, A. D. Daniels, M. C. Strain, O. Farkas, D. K. Malick, A. D. Rabuck, K. Raghavachari, J. B. Foresman, J. V. Ortiz, Q. Cui, A. G. Baboul, S. Clifford, J. Cioslowski, B. B. Stefanov, G. Liu, A. Liashenko, P. Piskorz, I. Komaromi, R. L. Martin, D. J. Fox, T. Keith, M. A. Al-Laham, C. Y. Peng, A. Nanayakkara, M. Challacombe, P. M. W. Gill, B. Johnson, W. Chen, M. W. Wong, C. Gonzalez, and J. A. Pople, Gaussian 03, Rev. E.01, Wallingford CT: Gaussian, Inc, 2004.

42 M. Wong, J. K. Thomas, and T. Nowak, *J. Am. Chem. Soc.,* 1977, 99, 4730-4736.

43 H.-S. Tan, I. R. Piletic, and M. D. Fayer, *J. Chem. Phys.,* 2005, 122, 174501.

44 M. R. Harpham, B. M. Ladanyi, and N. E. Levinger, *J. Phys. Chem. B,* 2005, 109, 16891-16900.

45 P. A. Pieniazek, Y.-S. Lin, J. Chowdhary, B. M. Ladanyi, and J. L. Skinner, *J. Phys. Chem. B,* 2009, 113, 15017-15028.

46 Y. Wang, D. S. D. Larsson, and D. v. d. Spoel, *Biochem.,* 2009, 48, 1006-1015.

47 M. Sharon, L. L. Ilag, and C. V. Robinson, *J. Am. Chem. Soc.,* 2007, 129, 8740-8746.

48 S.-W. Lee, P. Freivogel, T. Schindler, and J. L. Beauchamp, *JACS,* 1998, 120, 11758-11765.

49 W. D. V. Horn, A. K. Simorellis, and P. F. Flynn, *J. Am. Chem. Soc.,* 2005, 127, 13553-13660.

50 A. K. Simorellis, W. D. V. Horn, and P. F. Flynn, *J. Am. Chem. Soc.,* 2006, 128, 5082-5090.

51 A. D'Aprano, A. Lizzio, and V. T. Liveri, *J. Phys. Chem.,* 1987, 91, 4749-4751.

52 S. P. Moulik, and S. Ray, *Pure Appl. Chem.,* 1994, 66, 521-525.

Chapter 4

Solubilization of Amino Acids in Gas-Phase NaAOT Reverse Micelles

4.1 Introduction

In chapter 3, generation and characterization of gas-phase multiply positively charged NaAOT aggregates were reported. It was found that, gas-phase NaAOT aggregates tended to adopt a reverse micelle-like structure, with the composition of $[(\mathrm{NaAOT})_n\mathrm{Na}_z]^{z+}$. They are capable of encapsulating up to five glycine molecules in single reverse micelles. CID was employed to probe the interactions between surfactants and accommodated Gly molecules. It was concluded that gas-phase NaAOT reverse micelles could act as nanometer-sized vehicles for transport of non-volatile amino acids from solution to the gas phase. However, some interesting questions remained, particularly regarding the driving forces of incorporation of amino acids into gas-phase reverse micelles.

Driving forces for the uptake of amino acids into NaAOT/water reverse micelles in apolar solution have been reported in a great deal of work.[1-11] In sum, hydrophilic amino acids (both zwitterionic[12] and charged forms), are predominately hosted inside the micellar water pools,[7] and charged amino acids would lead to its increased solubilization as verified by pH variation experiments.[8-10] On the other hand, hydrophobic amino acids[13-15] are mainly incorporated in the interfacial surfactant layer via hydrophobic interactions, and electrostatic interactions may alter partitioning of hydrophobic amino acids between interfacial zones and water pools. Compared to the solution-phase study, much less is known about encapsulation of amino acids by gas-phase reverse micelles. Encapsulation and transport of amino acids and other biomolecules into gas-phase micelles allow new inroads for biophysical and bioanalytical research, enabling analysis of their properties under constrained environments in a vacuum. Therefore, it would be very informative to investigate and gain some insights into the driving forces for the incorporation of amino acids into NaAOT reverse micelles in the gas phase.

The work in this chapter is aimed at exploring the solubilization driving forces of various amino acids in gas-phase NaAOT reverse micelles, as well as how they could be tuned. Firstly, encapsulation of various amino acids and their model compounds in gas-phase NaAOT reverse micelles were compared using ESI mass spectrometry. Secondly, site locations of amino acids of different hydrophobicities and charge states within gas-phase reverse micelles were determined from CID of amino acid-encapsulating reverse micellar ions. Finally, different interactions between amino acids and reverse micelles were employed for selective encapsulation of amino acids by gas-phase reverse micelles.

4.2 Experimental

Instruments and materials Experiments were carried out on our ESI guided-ion-beam tandem mass spectrometer operated in positive ion mode. Both quadrupole mass filters operated at 880 kHz to cover the m/z range from 10 to 4,000. For conventional mass spectral measurements, the first quadrupole mass filter was operated in the rf-only mode as an ion guide, and mass scans were performed by the second quadrupole mass filter. The mass resolving power was adjusted to over 100 to resolve the charge and stoichiometry of ions without significantly losing ion intensities.

The molar masses, purities, suppliers and storage of chemicals and solvents used in this experiment are listed in appendix C. All chemicals were used without further purification. The operating procedure has been described in detail in chapter 3. Here only a list of key parameters adopted is given in Table 4.1, emphasizing the unique conditions of this experiment.

Table 4.1 Key operating parameters of the mass spectrometer in positive ion mode

ESI flow rate	0.04 ml•hr^{-1}
ESI bias voltage	3,000 V
Capillary bias voltage	70 V
Capillary temperature	150 °C
Skimmer bias voltage	10 V
Pressure in hexapole ion guide	10 – 15 mTorr

Table 4.2 Molecular structures, ionization constants and isoelectric points of various amino acids[12]

Amino acid	Glycine (G[a])	Aspartic acid (D[a])	Tryptophan (W[a])	Proline (P[a])	Arginine (R[a])
Structure	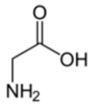	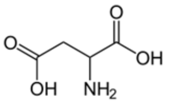	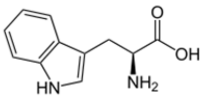	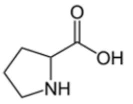	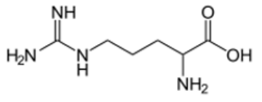
pK_a of α-COOH	2.3	1.9	2.8	2.0	2.2
pK_a of α-NH_3^+	9.6	9.6	9.4	10.6	9.0
pK_a of side chain	-	3.7	-	-	12.5
pI	6.1	2.8	5.9	6.3	10.8

[a] one-letter code for amino acid.

Positively charged micelle solution Table 4.2 lists the structures, ionization constants (pK_a), and isoelectric points (pI) in aqueous solutions for the amino acids under study. ESI solutions were prepared in methanol/water (1:1 volume ratio) containing 1.0×10^{-3} M NaAOT (below the CMC in water, 2.0×10^{-3} M,[16] so that reverse micelles were not formed) and 0.2×10^{-3} M amino acid (e.g. tryptophan). The solution was sonicated for 10 minutes prior to ESI. The pH of the solution was measured using a Thermo Scientific Orion 3-Star pH meter. As demonstrated below, NaAOT and amino acids were able to form amino acid-encapsulating reverse micelles via self-assembling in the gas phase between electrospray and exposure to the high vacuum of the mass spectrometer.[17, 18] CID product ion mass spectra of mass-selected NaAOT reverse micellar ions were measured at E_{col} = 1.0 eV for doubly charged ions and E_{col} = 1.5 eV for triply charged ions. All measurements were repeated at least three times.

4.3 Results and discussion

4.3.1 Solubilization of neutral and protonated tryptophan in gas-phase reverse micelles

Dependence of amino acid hydrophobicity and charge state on incorporation capacity into gas-phase reverse micelles In order to examine both hydrophobic effect and electrostatic effect in gas-phase reverse micelles, neutral and protonated tryptophan was chosen as guest molecules, based on the fact that tryptophan has the most hydrophobic side chain (i.e. indole ring) of all amino acids[13] but becomes hydrophilic upon protonation. An mass spectrum obtained from ESI of NaAOT (1.0×10^{-3} M) and tryptophan (0.2×10^{-3} M) in methanol/water is shown in Figure 4.1a. For the sake of clarity, the m/z range below 1500 is not shown, but no encapsulation of tryptophan was observed at that range. It was found that, within the instrument detection range, the dominant peaks belong to empty reverse micelles with the compositions of $[(NaAOT)_nNa_z]^{z+}$. Assignments of mass peaks of empty reverse micelles are based on the micellar aggregation numbers (n) and charges (z), and the labels for the same charge states are grouped together. For convenience, in the following discussion the empty reverse micelles are indicated as n/z. The pH of the ESI solution was measured at 6.1, which is close to the tryptophan isoelectric point (pI) of 5.9 reported in an aqueous solution. However, it can be expected that pH may increase dramatically in the electrospray droplets due to the nature of positive mode ESI processes. In addition, there may exist difficulties in ionizing the -COOH group of tryptophan, due to its proximity to AOT anionic head groups.[19] As a result, protonated tryptophan (henceforth designated as

WH) was incorporated into reverse micelles and detected in the mass spectrum with the compositions of $[(NaAOT)_nNa_{z-m}WH_m]^{z+}$. These are indicated in shaded areas and labeled (*n* + *m WH*)/*z*. Solubilization of protonated tryptophan can be viewed as an ion-exchange process between positively charged *WH* and Na^+ ions.[8, 10] To investigate the hydrophobic effect of the tryptophan indole group, the ESI solution pH was adjusted to 7.9 by adding NaOH to a concentration of 0.2 × 10^{-3} M in methanol/water. With these conditions, only neutral tryptophan (hereafter designated as *W*) was carried into gas-phase reverse micelles by ESI, with the compositions of $[(NaAOT)_nNa_zW_m]^{z+}$. *W*-encapsulating reverse micelles are indicated in shaded areas in Figure 4.1b, and labeled (*n* + *m W*)/*z*.

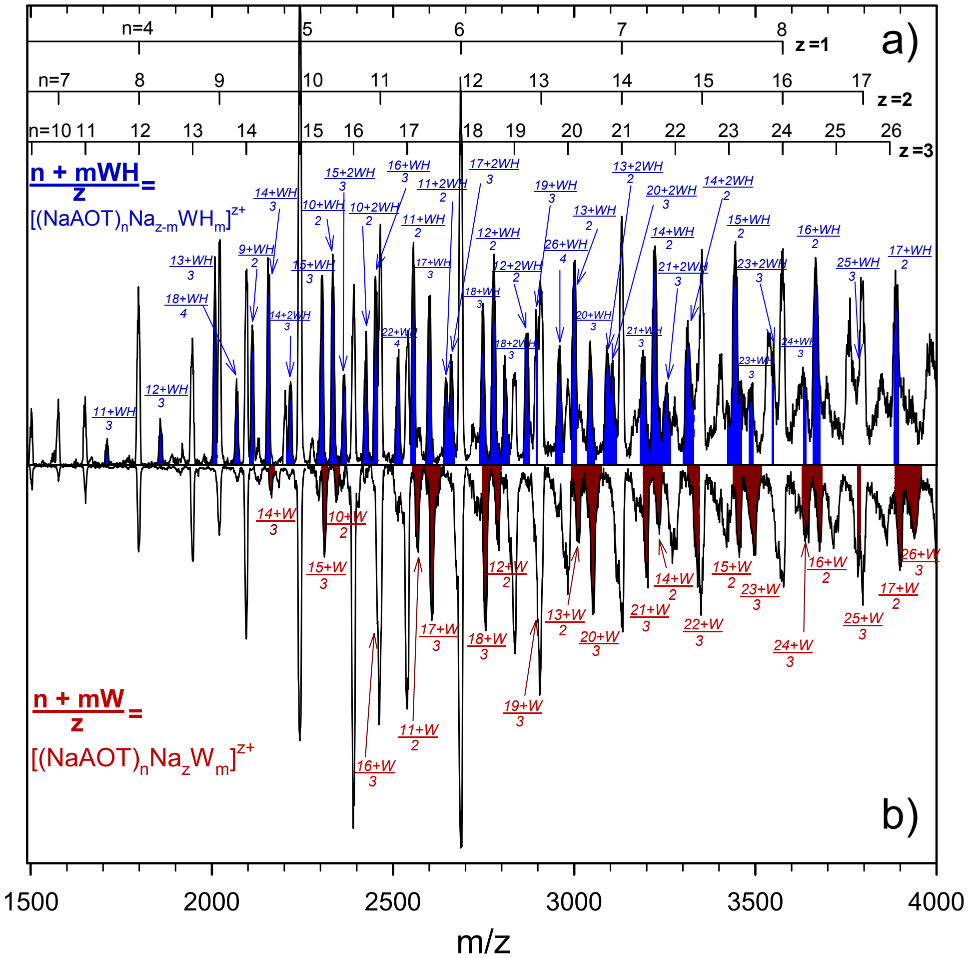

Figure 4.1 ESI mass spectra of NaAOT reverse micellar ions containing a) protonated tryptophan (*WH*) and b) neutral tryptophan (*W*).

Figures 4.1a and 4.1b show a strong correlation between size and incorporation capability of gas-phase reverse micelles. For doubly charged reverse micelles, incorporation of protonated tryptophan starts from aggregation number $n = 9$, and micelles of $n \geq 10$ can entrap two protonated tryptophan molecules. Triply charged reverse micelles start incorporating tryptophan at $n = 11$, and micelles of $n \geq 14$ can entrap two protonated tryptophan molecules. Assuming a spherical reverse micelle-like geometry for NaAOT aggregates, its core diameter D is roughly equal to $\sqrt{n \times A_{head} / \pi}$ where A_{head} is the area occupied by each AOT polar head at the interface ($0.52 nm^2$).[6, 20, 21] D is calculated to be 1.2, 1.3, 1.4, and 1.6 nm for $n = 9$, 10, 11and 14, respectively. The orientation-averaged size of a protonated tryptophan molecule is 0.5 – 0.6 nm. Taking into account the volume occupied by counter ions, Na^+, the number of encapsulated protonated tryptophan molecules roughly matches the reverse micellar core size. For comparison, incorporation of neutral tryptophan starts from $n = 10$ for doubly charged micelles, and $n = 14$ for triply charged micelles, respectively. Incorporation of more than one neutral tryptophan molecule in single micelles was not observed in Figure 4.1b. For both protonated and neutral tryptophan, the starting aggregation numbers for incorporation remained constant when the initial tryptophan-loading ratio to NaAOT, [tryptophan]/[NaAOT], varied from 10:1 to 10:3 in ESI solutions. These observations deviate from expectations if random associations are assumed between amino acids and surfactants. Similar results were obtained using protonated and neutral tyrosine as guest molecules for gas-phase NaAOT reverse micelles (mass spectra not shown), where the incorporation of protonated and neutral tyrosine both starts from $n = 8$ for doubly charged reverse micelles, and $n = 11$ for triply charged reverse micelles, respectively.

The fact that neutral hydrophobic amino acids (tryptophan and tyrosine) can be incorporated into gas-phase reverse micelles does not necessarily confirm that the hydrophobic effect is the major driving force for solubilization, since neutral amino acids most likely exist in zwitterionic forms and maintain some solute-surfactant electrostatic interactions. With this in mind, control experiments were performed using methanol/water solutions of NaAOT with various probe molecules, including phenol, β-naphthol and phloretic acid. Phenol and β-naphthol were used as probe molecules because they resemble the uncharged polar side chains of tryptophan and tyrosine, and can reside at the interface of NaAOT reverse micelles in apolar solvents (e.g. n-heptane and isooctane) as co-surfactants, with their hydroxyl groups hydrogen-bonded to AOT polar heads and aromatic rings penetrating between AOT hydrocarbon tails.[19, 20, 22, 23] Phloretic acid was chosen since it is actually a tyrosine analogue with only the amino group is absent from the tyrosine structure. ESI mass spectra of the solutions containing NaAOT and each of the three probe molecules were measured, respectively, following the same procedures used for NaAOT/amino acids. Their solution pH was not adjusted intentionally, i.e., pH 6.5 for NaAOT (1.0×10^{-3} M)/phenol (0.2×10^{-3} M) and NaAOT(1.0×10^{-3} M)/β-naphthol (0.2×10^{-3} M) in methanol/water, and pH 4.8 for NaAOT (1.0×10^{-3} M)/phloretic acid (0.2×10^{-3} M) in methanol/water. Surprisingly, none of the three probe molecules were observed within gas-phase NaAOT reverse micelles. It may be argued that phenol and β-naphthol could not effectively incorporate onto the micellar interface during self-assembling of NaAOT reverse micelles in the gas phase. For this reason, ESI mass spectra of NaAOT (5.0×10^{-3} M)/water (5.0×10^{-2} M)/hexane reverse micellar solutions containing 1×10^{-3} M phenol and β-naphthol were also measured, respectively. The NaAOT concentration used is above its CMC in hexane[16] to ensure the formation of NaAOT and water reverse micelles in hexane as well as adsorption of phenol or β-naphthol at the water pool interface. Again, neither phenol nor β-naphthol was detected in the ESI mass spectra. Obviously, the hydrophobic effect and hydrogen bonding are not strong enough to incorporate phenol and β-naphthol onto the surface of gas-phase reverse micelles. From the fact that phloretic acid could not be incorporated, it can be inferred that the carboxylic acid group alone (without the amino group in the molecule) does not help achieve a great enough driving force for incorporation of the molecule into gas-phase reverse micelles, either. Consequently, neutral *zwitterionic* tryptophan (and tyrosine) must have the charged $-NH_3^+$ group strongly interact with AOT sulfonic group. It is the combination of hydrophobic and electrostatic interactions that allows incorporation of neutral tryptophan (and tyrosine) into gas-phase reverse micelles.

It would be interesting to compare incorporation of protonated and neutral amino acids qualitatively. For this purpose, relative incorporation efficiencies defined as

$$E_{WH} = \frac{I([(NaAOT)_n Na_{z-1} WH]^{z+})}{I([NaAOT)_n Na_z]^{z+})} \qquad (1)$$

and

$$E_W = \frac{I([(NaAOT)_n Na_z W]^{z+})}{I([NaAOT)_n Na_z]^{z+})} \qquad (2)$$

were calculated, where $I([(NaAOT)_nNa_{z-1}WH]^{z+})$, $I([(NaAOT)_nNa_zW]^{z+})$ and $I([(NaAOT)_nNa_z]^{z+})$ represent measured ion intensities of *WH*-, *W*-encapsulating, and empty host reverse micellar ions, respectively. To avoid complication of mass coincidence of selected host micellar ions with other charge states, $[(NaAOT)_nNa_z]^{z+}$ of *13/2*, *15/2*, *17/2*, *14/3*, *16/3*, *17/3* and *20/3* were chosen as host micellar ions for analysis. NaAOT reverse micellar ions can each encapsulate more than one *WH* molecule; however, the contributions of multiple encapsulations of *WH* were not included when calculating incorporation efficiencies E_{WH}. This omission was deliberate, since reverse micellar ions can only take one

W molecule each. For direct comparison of incorporation efficiencies for WH and W, the results focused on encapsulation of single molecules in both cases. The calculation results are listed in Table 4.3, and were averaged over three sets of mass spectra. For comparison, the incorporation efficiencies E_{GH} and E_{G} (i.e., efficiencies of incorporating one protonated glycine and one neutral glycine in NaAOT reverse micellar ions, respectively), calculated from our previous experimental data[18] has been included in Table 4.3. These calculations give very rough estimates, but are sufficient to reveal general trends. Clearly, protonation dramatically increases the incorporation efficiencies of tryptophan for all reverse micelles, but has little effect on incorporation efficiencies of glycine.

Table 4.3 Incorporation efficiencies of protonated (WH) and neutral (W) tryptophan, and protonated (GH) and neutral (G) glycine in gas-phase NaAOT reverse micellar ions

Host reverse micellar ions [a]	E_{WH}	E_{W}	E_{WH} / E_{W}	E_{GH}	E_{G}	E_{GH} / E_{G}
$\frac{13}{2}$	1.11	0.34	3.3	0.82	0.60	1.4
$\frac{15}{2}$	1.03	0.62	1.7	0.78	0.90	0.9
$\frac{17}{2}$	1.09	0.70	1.6	1.30	1.50	0.9
$\frac{14}{3}$	1.06	0.20	5.3	0.65	0.50	1.3
$\frac{16}{3}$	1.04	0.40	2.6	0.83	0.71	1.2
$\frac{17}{3}$	1.25	0.67	1.9	1.00	0.94	1.1
$\frac{20}{3}$	1.42	1.10	1.3	1.25	1.20	1.0

[a] Host reverse micellar ions are indicated as $\frac{n}{z}$, where n is the aggregation number, and z is the total charge.

The differences between E_{WH} and E_{W}, and between E_{GH} and E_{G}, arise from the extra electrostatic interactions between protonated amino acids and anionic AOT polar heads. It was found that, on average, this extra electrostatic effect improves incorporation efficiencies of tryptophan by a factor of 2 – 3. Note that the enhancement ratio of E_{WH}/E_W decreases rapidly with increasing micellar size, and approaches a minimum for reverse micelles of *20/3*. This is simply due to the fact that large micelles can hold more *WH* molecules. For glycine, there is no hydrophobic contribution and an attractive electrostatic potential is needed for solubilization of this amino acid in reverse micelles. Therefore, a large increase in incorporation was expected when glycine becomes protonated. However, there is no dramatic difference between E_{GH} and E_G. Only a slight enhancement of E_{GH}/E_G was observed upon protonation of glycine (except for micelles of *15/2* and *17/2*, where protonation causes a minor decrease in the uptake of single amino acids, presumably because the fraction of reverse micelles containing more than one glycine molecule increases upon protonation of glycine). The observed small differences between E_G and E_{GH} were tentatively attributed to the fact that neutral zwitterionic glycine structure could interact with sodium ions and AOT polar heads inside the micellar cavity and becomes stabilized by these electrostatic interactions. It is also worth noting that, in the gas phase the glycine-Na^+ binding energy is 1.7 eV,[24, 25] and proton affinity of glycine (9.2 eV).[26] However, the gas-phase affinity values seem have very little connection with the expected behavior in condensed phase or in gas-phase reverse micelles.

Solubilization sites of hydrophilic and hydrophobic amino acids Figure 4.2 shows the CID product ion mass spectra of *WH*-encapsulating reverse micellar ions, measured at E_{col} = 1.0 eV for doubly charged precursor ions and 1.5 eV for triply charged precursor ions. To map out all dissociation product ions within the instrumental m/z detection limit, CID mass spectra were obtained at a relatively high Xe pressure (0.15 mTorr) in the scattering cell. Because of multiple collisions between precursor ions and Xe at this gas pressure, and because primary fragment ions may continue to undergo collisions that cause them to fragment, the relative intensities of product ions in CID mass spectra do not reflect CID branching ratios. However, all product ions were observed at a Xe pressure of 0.01-0.013 mTorr, where the probability of multiple collisions is < 4%. CID of multiply charged reverse micellar ions results in numerous dissociation channels and product ions of varying mass and charge, and some product ions may possess m/z that is beyond the instrument detection limit. In addition, because of mass coincidence among different charged states, some ion peaks may actually be attributed to more than one product ion mass. For example, m/z of 3131 may represent micelles of three overlapping charge states *7/1*, *14/2*, and *21/3*. In Figure 4.2, alternative assignments for some product ions are indicated in parentheses.

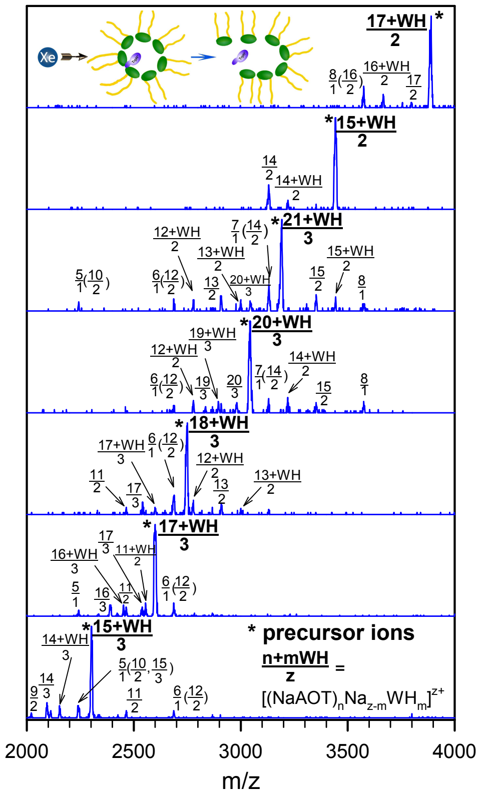

Figure 4.2 CID mass spectra of mass-selected micellar ions containing protonated tryptophan (*WH*). Spectra were measured at E_{col} = 1.0 eV for doubly charged precursor ions and E_{col} = 1.5 eV for triply charged precursor ions, with 0.15 mTorr Xe in the scattering cell. Asterisks indicate precursor ions, and labels in parentheses are alternative assignments for product ions. Inserted cartoon illustrates encapsulation of *WH* within the gas-phase reverse micellar core.

Table 4.4 summarizes dissociation channels for selected *WH*-encapsulating reverse micellar ions. For most dissociation channels, both complementary product ions produced from a dissociation leading to two charged products were observed in mass spectra. For comparison, the CID results of corresponding neutral Gly-encapsulating NaAOT reverse micellar ions have also been included in Table 4.4, along with empty reverse micellar ions obtained from the previous study[18] discussed in previous chapter. Because glycine and protonated tryptophan are both hydrophilic, similarities would be expected in dissociation of reverse micelles containing these two amino acids.

Table 4.4 CID products of empty and amino acid-encapsulating NaAOT micellar ions

WH-encapsulating micellar ions [a]	Dissociation channels	Gly-encapsulating micellar ions [b]	Dissociation channels	Empty micellar ions [b]	Dissociation channels
$\frac{15+WH}{2}$	$\frac{14+WH}{2}+1$ $\frac{14}{2}+1+WH$	$\frac{15+G}{2}$	$\frac{13}{2}+2+G$ $\frac{14}{2}+1+G$	$\frac{15}{2}$	$\frac{9^c}{1}+\frac{6}{1}$ $\frac{8}{1}+\frac{7}{1}$
$\frac{17+WH}{2}$	$\frac{17}{2}+WH$ $\frac{16+WH}{2}+1$ $\frac{16}{2}+1+WH$ $\frac{9^c}{1}+\frac{8}{1}+WH$	$\frac{17+G}{2}$	$\frac{16+G}{2}+1$ $\frac{9^c}{1}+\frac{8}{1}+G$	$\frac{17}{2}$	$\frac{11^c}{1}+\frac{6}{1}$ $\frac{10^c}{1}+\frac{7}{1}$ $\frac{9^c}{1}+\frac{8}{1}$
$\frac{15+WH}{3}$	$\frac{14+WH}{3}+1$ $\frac{14}{3}+1+WH$ $\frac{10}{2}+\frac{5}{1}+WH$ $\frac{9}{2}+\frac{6}{1}+WH$ $\frac{11}{2}+\frac{4}{1}+WH$				

$\frac{17+WH}{3}$	$\frac{17}{3}+WH$ $\frac{16+WH}{3}+1$ $\frac{16}{3}+1+WH$ $\frac{12}{2}+\frac{5}{1}+WH$ $\frac{11+WH}{2}+\frac{6}{1}$ $\frac{11}{2}+\frac{6}{1}+WH$	$\frac{17+G}{3}$	$\frac{16+G}{3}+1$ $\frac{16}{3}+1+G$ $\frac{12}{2}+\frac{5}{1}+G$ $\frac{11}{2}+\frac{6}{1}+G$	$\frac{17}{3}$	$\frac{16}{3}+1$ $\frac{12}{2}+\frac{5}{1}$ $\frac{11}{2}+\frac{6}{1}$ $\frac{9}{2}+\frac{8}{1}$
$\frac{18+WH}{3}$	$\frac{17+WH}{3}+1$ $\frac{17}{3}+1+WH$ $\frac{13+WH}{2}+\frac{5}{1}$ $\frac{13}{2}+\frac{5}{1}+WH$ $\frac{12+WH}{2}+\frac{6}{1}$ $\frac{12}{2}+\frac{6}{1}+WH$ $\frac{11}{2}+\frac{7}{1}+WH$				
$\frac{20+WH}{3}$	$\frac{20}{3}+WH$ $\frac{19+WH}{3}+1$ $\frac{19}{3}+1+WH$ $\frac{14+WH}{2}+\frac{6}{1}$ $\frac{14}{2}+\frac{6}{1}+WH$ $\frac{12+WH}{2}+\frac{8}{1}$ $\frac{12}{2}+\frac{8}{1}+WH$	$\frac{20+G}{3}$	$\frac{19+G}{3}+1$ $\frac{19}{3}+1+WH$ $\frac{13+G}{2}+\frac{7}{1}$ $\frac{13}{2}+\frac{7}{1}+G$	$\frac{20}{3}$	$\frac{14}{2}+\frac{6}{1}$ $\frac{13}{2}+\frac{7}{1}$ $\frac{12}{2}+\frac{8}{1}$ $\frac{11}{3}+\frac{9^{c}}{1}$ $\frac{10}{2}+\frac{10^{c}}{1}$

$\frac{21+WH}{3}$	$\frac{20+WH}{3}+1$ $\frac{16}{2}+\frac{5}{1}+WH$ $\frac{15+WH}{2}+\frac{6}{1}$ $\frac{15}{2}+\frac{6}{1}+WH$ $\frac{14}{2}+\frac{7}{1}+WH$ $\frac{13+WH}{2}+\frac{8}{1}$ $\frac{13}{2}+\frac{8}{1}+WH$ $\frac{12+WH}{2}+\frac{9^c}{1}$ $\frac{12}{2}+\frac{9^c}{1}+WH$				

[a] Precursor and product ions are indicated as $\frac{n+mWH}{z}$ for those containing protonated tryptophan (WH), $\frac{n+mG}{z}$ for those containing glycine (G), and $\frac{n}{z}$ for empty micelles, where n is the aggregation number, z is the total charge, and m is the number of encapsulated amino acids.

[b] From ref. 18

[c] Beyond the m/z detection limit of the mass spectrometer.

As demonstrated in Figure 4.2 and Table 4.4, dissociation of reverse micellar ions showed a strong dependence on their charge state and encapsulation. CID of doubly charged empty NaAOT reverse micellar ions exclusively produced singly charged fragment ions, while CID of triply charged empty NaAOT reverse micellar ions resulted in singly, doubly and triply charged ions.[18] Occupied reverse micellar ions had distinct dissociation channels from empty ones, producing large product ions, some of which still encapsulate amino acids. This suggested that amino acid encapsulation improved the overall stability of reverse micellar structures. It is worth noting that, all listed pairs of *WH*- and Gly-encapsulating reverse micellar ions, (15+WH)/2 and (15+G)/2, (17+WH)/2 and (17+G)/2, (17+WH)/3 and (17+G)/3, and (20+WH)/3 and (20+G)/3, exhibited similar dissociation patterns. In Figure 4.1a (i.e. a mass spectrum of *WH*-encapsulating micellar ions) a strong correlation was observed between the encapsulation capability and the size of micellar ions. Similar behavior was also observed in CID mass spectra of *WH*-encapsulating reverse micelles. The smallest stripped micellar ions still capable of hosting protonated tryptophan were 11/2.

In chapter 3, CID cross sections were measured for mass-selected empty and Gly-encapsulating precursor reverse micellar ions. It was found that CID cross sections were approaching the hard-sphere collision limits at high collision energies (assuming spherical geometries for reverse micellar ions). The cross sections provided a measure of the lowest limit of the average micelle size. Measurements of CID cross sections were also attempted at various collision energies for this system. Unfortunately, the low intensities of selected *WH*-encapsulating precursor ions made it exceedingly difficult to achieve good signal-to-noise ratios for measurements at a Xe pressure of 0.01 mTorr (which was required to ensure a single-collision condition between micellar ions and Xe). Note that, CID cross sections generally increase with increasing E_{col} and the maximum CID cross sections of *WH*-encapsulating reverse micellar ions seem close to those of corresponding Gly-encapsulating reverse micellar ions. The resemblance between CID products and cross sections of *WH*- and Gly-encapsulating reverse micellar ions were so striking that they made clear the conclusion that protonated tryptophan was encapsulated inside the micellar core and attracted to AOT head groups near the interface. This is similar to the site location of protonated tryptophan in NaAOT and water reverse micelles immersed in apolar media such as n-heptane and dichloroethane,[7, 11] and is consistent with the molecular dynamics simulated solute location of positively charged chromophore in NaAOT reverse micelles.[27]

CID of mass-selected reverse micellar ions containing neutral tryptophan, *W*, as depicted in Figure 4.3, revealed different dissociation patterns than those containing *WH* and glycine. Dissociation of *W*-encapsulating reverse micellar ions corresponded to stripping of *W* (and only *W* moiety) off reverse micelles. Such CID results provided direct evidence of the incorporation site location of neutral tryptophan. In other words, neutral tryptophan must adsorb to the micellar surface due to its hydrophobic nature. This scenario raised two possibilities. Neutral tryptophan could either penetrate into the surfactant polar head layer as a co-surfactant,[4] or randomly tether to and/or embed in AOT hydrophobic tails following the principle of "like dissolves like". The second possibility may be discounted for several reasons. First, if random associations were assumed between tryptophan and AOT, associations between tryptophan and small NaAOT aggregates would have been observed. In fact, NaAOT reverse micelles demonstrated strong size dependence for incorporation of neutral tryptophan. Incorporation of tryptophan started from reverse micelles with aggregation number ≥ 10. Secondly, as described above, polar hydrophobic molecules such as phenol and β-naphthol could not be carried by gas-phase NaAOT reverse micelles at all, suggesting that the hydrophobic effect (of the tryptophan indole group) was unable to allow the micellar assembly of NaAOT and neutral tryptophan survive in the gas phase. Thirdly, the control experiment using the tyrosine model molecule, phloretic acid, confirmed that, in the absence of an amino group, the carboxylic acid group did not help satisfy the forces for incorporation of amino acid. All these facts led to the conclusion that neutral tryptophan must have intercalated in the surfactant interfacial layer, acting as a co-surfactant based on a "surface-monolayer" model where the solute was adsorbed into the interface.[1-4] The driving forces for incorporation had contributions from the hydrophobic effect of the indole group with AOT branched alkyl tails; and more importantly, from the electrostatic interactions between the zwitterionic backbone $^{+}H_3N\text{-}C^{\alpha}\text{-}COO^{-}$ and the anionic AOT sulfonic polar head.[10] Repulsion between the zwitterion carboxylate group and the

AOT anionic polar head may exist, but this could be compensated by the attraction between the carboxylate group and the Na^+ ions located near the interface head region. The proposed incorporation mechanism for neutral tryptophan explains the reverse micelle size dependence of tryptophan incorporation capacity (see Figure 4.1b). Small reverse micelles (i.e., $n < 10$ for doubly charged micelles) had large curvatures, and consequently, could not provide enough interfacial area (near head regions) for incorporation of guest tryptophan molecule. For triply charged micelles, the extra Na^+ made the micelle more rigid and increased the curvature, so incorporation of neutral did not occur for $n < 14$.

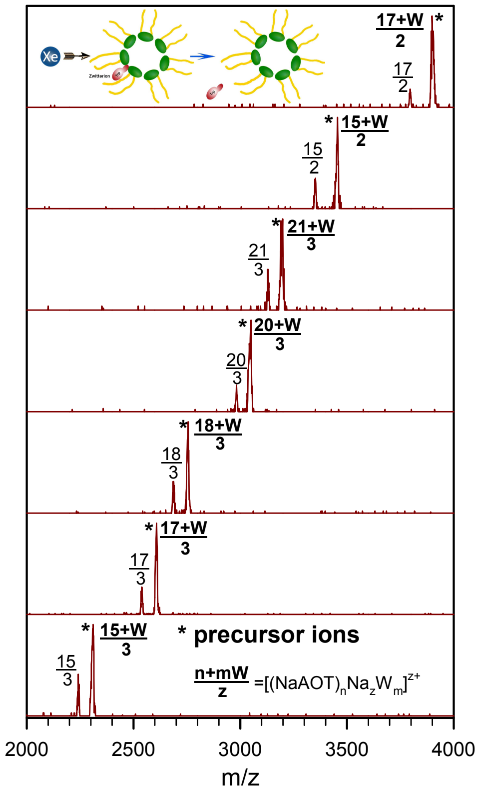

Figure 4.3 CID mass spectra of mass-selected micellar ions containing neutral tryptophan (*W*). Spectra were measured at E_{col} = 1.0 eV for doubly charged precursor ions and E_{col} = 1.5 eV for triply charged precursor ions, with 0.15 mTorr Xe in the scattering cell. Asterisks indicate precursor ions. Inserted cartoon illustrates interfacial incorporation of *W* by gas-phase reverse micelles.

Note that the possibility could not be ruled out that protonated tryptophan could partition between the reverse micellar inner core and the reverse micelle interfacial region. However, based on the comparison of CID mass spectra of *WH*- and *W*-encapsulating reverse micellar ions, protonated tryptophan predominantly partitioned inside the core and its interfacial solubilization was negligible. Different site locations of protonated and neutral tryptophan also explained the observations in Figures 4.1a and 4.1b that large reverse micelles had a higher capability of encapsulating *WH* inside the core than incorporating *W* outside — this was because the micellar core volume $(=(n\times A_{head})^{3/2}/6\pi^{1/2}$, where A_{head} is AOT polar head area as defined above) increases faster with the aggregation number *n* than the micellar interface area $(=n\times A_{head})$.

4.3.2 Selective encapsulation of various amino acids by gas-phase reverse micelles

Aspartic acid *versus* tryptophan Dependence of site localization of tryptophan on the pH of the ESI solution provided insight into the driving forces for gas-phase reverse micellar solubilization. It demonstrated that different experimental parameters may be used to control and manipulate the interactions between amino acid and NaAOT surfactants, and therefore the incorporation site of the same amino acid within reverse micelles. It may also make selective incorporation of amino acids of different charge states possible. To investigate this possibility, experiments were carried out in the presence of two amino acids. First, aspartic acid and tryptophan were chosen on the basis of their pI values. Aspartic acid is hydrophilic and has two carboxylic acid groups, with pK_{a1} 1.9, pK_{a2} 3.7, pK_{a3} 9.6, and pI 2.8 (lower than tryptophan pI 5.9 by 3.1 units). Shown in Figure 4.4 is the mass spectrum of an ESI solution containing NaAOT (1.0×10^{-3} M) and aspartic acid (0.1×10^{-3} M) in methanol/water with pH 4.6. As illustrated in this figure, gas-phase reverse micelles were occupied by protonated aspartic acid (henceforth designated as *DH*). No neutral aspartic acid was observed; presumably because of the change of pH in the spraying droplets and of pK_a and pI of aspartic acid in reverse micelles.[10, 19] However, all ion peaks associated with encapsulation of protonated aspartic acid disappeared after the addition of 0.1×10^{-3} M tryptophan to the ESI solution (pH changed to 5.1). Instead, a mass spectrum similar to Figure 4.1a was obtained, where only protonated tryptophan was encapsulated. In other words, gas-phase reverse micelles exclusively selected protonated tryptophan.

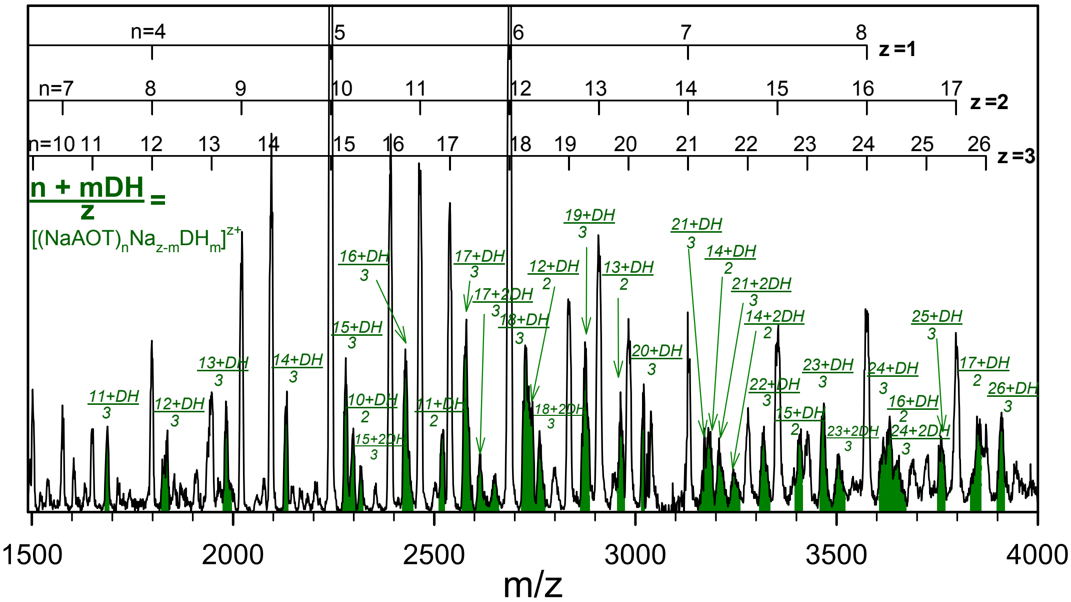

Figure 4.4 ESI mass spectrum of gas-phase NaAOT reverse micellar ions containing protonated aspartic acid (*DH*).

Arginine versus tryptophan Arginine and tryptophan were compared in a similar fashion. Arginine has two amino groups, with pK_{a1} 2.2, pK_{a2} 9.0, pK_{a3} 12.5, and pI 10.8. As presented in Figure 4.5, the mass spectrum of NaAOT (1.0×10^{-3} M), arginine (0.1×10^{-3} M) and tryptophan (0.1×10^{-3} M) in methanol/water (pH 7.5) only showed encapsulation of protonated arginine (designated as *RH*) in gas-phase reverse micelles. Observations of protonated tryptophan from a mixture of aspartic acid and tryptophan, and of protonated arginine from a mixture of arginine and tryptophan, as shown in Figures 4.4 and 4.5, respectively, indicated that different amino acids competed for protons in solutions and/or during ESI. The amino acid with a higher pI was more likely protonated, and the corresponding protonated species had a greater chance for encapsulation within the micellar core through electrostatic interactions with AOT anionic polar heads. Consequently, the preference for encapsulation within the micellar core increased in ascending order of amino acid pI values, i.e., aspartic acid (pI 2.8) < tryptophan (5.9) < arginine (10.8). This interpretation is supported by another experiment in which tryptophan and proline were compared. It was found that gas-phase reverse micelles showed less discrimination between tryptophan (pI 5.9) and proline (pI 6.3) than between tryptophan and arginine. It should also be noted that pI values of these amino acids are adopted from their aqueous solutions, and are used here only as a guide to predict amino acid responsiveness in the gas phase and in micellar environments.

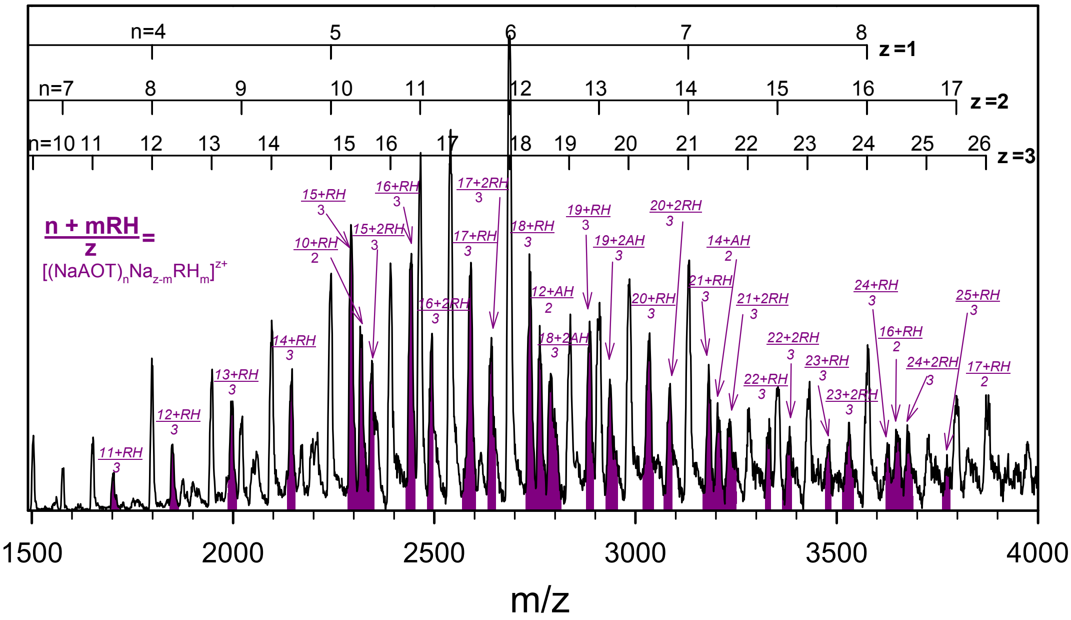

Figure 4.5 ESI mass spectrum of an ESI solution containing NaAOT (1.0×10^{-3} M), arginine (0.1×10^{-3} M), and tryptophan (0.1×10^{-3} M) in methanol/water (1:1 volume ratio). Only protonated arginine (*RH*) was encapsulated into gas-phase reverse micelles. No tryptophan was detected.

This interpretation did not completely explain the selective encapsulation of different amino acids by reverse micelles. For example, the methanol/water solution of NaAOT (1.0×10^{-3} M), arginine (0.1×10^{-3} M) and tryptophan (0.1×10^{-3} M) has a similar pH (7.5) to that of NaAOT (1.0×10^{-3} M) and tryptophan (0.2×10^{-3} M) (pH 7.9). Considering the latter solution was used for obtaining neutral tryptophan-encapsulating reverse micellar ions in Figure 4.1b, some neutral tryptophan-entrapped reverse micellar ions would have been expected from the NaAOT/arginine + tryptophan solution as well. However, no significant amount of tryptophan was detected in Figure 4.5. This could be rationalized by two possible reasons. First, the spraying droplets may have a greater fraction of protonated arginine than that of neutral tryptophan, resulting in most reverse micelles being occupied by protonated arginine instead of neutral tryptophan. Second, protonated arginine established strong electrostatic interactions with AOT polar heads at the interface, which pulled the AOT head groups together and increased the curvature and rigidity of the micelle interface, leading to expulsion of neutral tryptophan from the curved surfactant-head region (i.e. a squeezing-out effect[1, 3]). The strong electrostatic interactions also inhibited change in micellar shape, a change required to accommodate neutral tryptophan at the curved interfacial region.[11] Consequently, protonated arginine acted as a stripping agent and neutral tryptophan molecules could no longer be incorporated in its presence. A similar phenomenon occurred in the presence of protonated tryptophan and neutral aspartic acid. This indicated that electrostatic associations between AOT anionic polar heads and positively charged amino acids were more important than other factors for controlling amino acid solubilization in gas-phase reverse micelles. Note that selective extraction of different amino acids had been reported for NaAOT reverse micelles in supercritical fluids[6] and in isooctane,[28] but none of those experiments showed exclusive extraction with a high selectivity as presented in our gas-phase system.

4.4 Conclusions

In this chapter, encapsulation of various hydrophilic and hydrophobic amino acids in gas-phase NaAOT reverse micelles was studied and their mechanisms were elucidated. Electrostatic and hydrophobic effects on the solubilization of amino acids were evaluated in the experiment. It was found that, hydrophilic amino acids were encapsulated inside micellar cavities via electrostatic interactions. Neutral tryptophan, on the other hand, intercalated in the interfacial region and acted as a co-surfactant. These phenomena could be expected from the hydrophobicities of amino acids as determined from their partitioning between a hydrophobic environment and aqueous solution.[13-15] Solubilization of hydrophobic tryptophan required forces contributed from both the hydrophobic effect of amino acid side chain and the electrostatic interactions between amino acid backbone $–H_3N^+$-C^{α}-COO^- and NaAOT. Protonation of tryptophan could significantly improve its incorporation efficiency in gas-phase reverse micelles, and displaced its site locations from the interfacial region to the micellar core. In contrast, protonation of glycine had little effect on its encapsulation in gas-phase reverse micelles. Encapsulation of protonated amino acids made the micellar structure more rigid and stable,[11] and inhibited further incorporation of neutral amino acids at the interfacial region. This explained the experimental observations that gas-phase reverse micelles showed preferential encapsulation of tryptophan over aspartic acid and of arginine over tryptophan, consistent with the order of their isoelectric points (i.e. protonation capabilities) in aqueous solutions.

This study also demonstrates that, compared to the hydrophobic effect, electrostatic interactions were much stronger for driving solubilization of amino acids in gas-phase reverse micelles. The most interesting finding is that, gas-phase reverse micelles were able to act as nanometer-sized vehicles for selective transport of hydrophilic and hydrophobic amino acids into the gas phase. This may lead to potential applications of reverse micelles in gas-phase separation and mass analysis of neutral and charged amino acids. It also provided insight on the dynamics of amino acid transport in atmospheric reverse micelle aerosols.

References

1 E. B. Leodidis, and T. A. Hatton, *J. Phys. Chem.,* 1990, 94, 6400-6411.

2 E. B. Leodidis, and T. A. Hatton, *J. Phys. Chem.,* 1990, 94, 6411-6420.

3 E. B. Leodidis, A. S. Bommarius, and T. A. Hatton, *J. Phys. Chem. ,* 1991, 95, 5943-5956.

4 E. B. Leodidis, and T. A. Hatton, *J. Phys. Chem.,* 1991, 95, 5957-5965.

5 E. B. Leodidis, and T. A. Hatton, *J. Colloid Interface Sci.,* 1991, 147, 163-177.

6 R. M. Lemert, R. A. Fuller, and K. P. Johnston, *J. Phys. Chem.,* 1990, 94, 6021-6028.

7 M. Adachi, M. Harada, A. Shioi, and Y. Sato, *J. Phys. Chem.,* 1991, 95, 7925-7931.

8 M. M. Cardoso, M. J. Barradas, M. T. Carrondo, K. H. Kroner, and J. G. Crespo, *Bioseparation,* 1998, 7, 65-78.

9 M. M. Cardoso, M. J. Barradas, K. H. Kroner, and J. G. Crespo, *Journal of Chemical Technology and Biotechnology,* 1999, 74, 801-811.

10 X. Fu, J. Li, Y. Ma, L. Zhang, D. Wang, and Z. Hu, *Colloids and Surfaces A: Physicochemical and Engineering Aspects,* 2001, 179, 1-10.

11 R. Rinaldi, P. L. O. Volpe, and I. L. Torriani, *J. Colloid Interface Sci.,* 2008, 318, 59-67.

12 P. Vollhardt, and N. Schore, *Organic Chemistry*. 6th edn. 1270 vols (New York: W. H. Freeman and Company, 2009).

13 Y. Nozaki, and C. Tanford, *J. Bio. Chem.,* 1971, 246, 2211-2217.

14 W. C. Wimley, T. P. Creamer, and S. H. White, *Biochemistry,* 1996, 35, 5109-5124.

15 W. C. Wimley, and S. H. White, *Nature Structure Biology,* 1996, 3, 842-848.

16 K. Mukherjee, S. P. Moulik, and D. C. Mukherjee, *Langmuir,* 1993, 9, 1727-1730.

17 D. Bongiorno, L. Ceraulo, A. Ruggirello, V. T. Liveri, E. Basso, R. Seraglia, and P. Traldi, *J. Mass Spectrom.,* 2005, 40, 1618-1625.

18 Y. Fang, A. Bennett, and J. Liu, *Int. J. Mass Spectrom.,* 2010, 293, 12-22.

19 F. M. Menger, and G. Saito, *J. Am. Chem. Soc.,* 1978, 100, 4376-4379.

20 P. L. Luisi, M. Giomini, M. P. Pileni, and B. H. Robinson, *Biochim. Biophys. Acta,* 1988, 947, 209-246.

21 A. M. Maitra, and P. K. Patanjali, in *Surfactants in Solution*, ed. by K. L. Mittal and P. Bothorel (New York: Plenum Press, 1986), p. 581.

22 L. J. Magld, K. Kon-no, and C. A. Martin, *J. Phys. Chem.,* 1981, 85, 1434-1439.

23 E. Bardez, E. Monnier, and B. Valeur, *J. Phys. Chem.,* 1985, 89, 5031-5036.

24 R. M. Moision, and P. B. Armentrout, *J. Phys. Chem. A,* 2002, 106, 10350-10351-10362.

25 S. J. Ye, R. M. Moision, and P. B. Armentrout, *Int. J. Mass Spectrom.,* 2005, 240, 233-248.

26 M. J. Locke, and R. T. McIver, Jr. , *J. Am. Chem. Soc.,* 1983, 105, 4226-4232.

27 J. Faeder, and B. M. Ladanyi, *J. Phys. Chem. B,* 2005, 109, 6732-6740.

28 M. Hebrant, and C. Tondre, *Analytical Sciences,* 1998, 14, 109-115.

Chapter 5

Effects of Negative Charge State on Gas-Phase NaAOT Micellar Structures and Encapsulation Properties

5.1 Introduction

NaAOT is soluble in various solvents with the ability to assemble into direct or reverse micelles. In nonpolar media[1, 2] or super critical fluids,[3] reverse micellar assemblies emerge with AOT polar heads oriented around an central core and hydrophobic chains directed outward. The size of reverse micelle grows by absorbing water molecules into the inner core,[4] and the system is described as "water-in-oil" micro-emulsion in the presence of a large water content. By contrast, when dissolved in polar solvents above its critical micellar concentration (CMC), NaAOT surfactants form direct micelles by hydrophobic effects, with their hydrophobic tails constituting an apolar center and hydrophilic polar heads in contact with surrounding solvent molecules,[1, 5, 6] referred to as direct or "oil-in-water" micelles. An interesting question is whether direct and reverse micellar structures could evolve via self-assembling of NaAOT in the gas phase.

Chapters 3 and 4 reported the formation and characterization of multiply positively charged NaAOT aggregates in the gas phase using our ESI mass spectrometry[7], along with the determination of driving forces for amino acid solubilization. It was found that positively charged NaAOT gas-phase micelles tend to adopt reverse micelle-like structure, with the compositions of $[Na_{n+z}AOT_n]^{z+}$ and could accommodate various guest molecules. Hydrophilic amino acids were encapsulated inside micellar cavities via electrostatic interactions, while solubilization of hydrophobic amino acids required combination of forces from both hydrophobic and electrostatic effects. In addition, gas-phase reverse micelles were able to act as nanometer-sized vehicles for selective transport of hydrophilic and hydrophobic amino acids in the gas phase.

In this chapter, multiply negatively charged NaAOT micelles in the gas phase was studied, attempting to illuminate the charge state effects on gas-phase micellar structure as well as micellar incorporation capability towards amino acids. Our mass spectrometry was employed to examine the stoichiometry, incorporation and dissociation of negatively charged aggregates. The results led to taking into consideration the possibility of a direct micelle-like structure for negatively charged gas-phase NaAOT aggregates.

5.2 Experimental

Instruments and materials In the present study, the experiments were carried out on our guided-ion beam tandem mass spectrometer as described in previous chapters, except that the apparatus was operated in negative ion mode. Both quadrupole mass filters were operated at 880 kHz to cover a m/z range from 10 to 4,000. The mass resolving power was adjusted to over 100 to resolve the charge and stoichiometry of ions without significantly losing ion intensities.

The molar masses, purities, suppliers and storage of chemicals and solvents used in this experiment are listed in appendix C. All chemicals were used without further purification. The operating procedure has been described in detail in chapter 3. Here only a list of key parameters adopted in this experiment is given in Table 5.1.

Negatively charged micelles NaAOT solutions were prepared in methanol/water (1:1 volume ratio) with NaAOT concentration varying from 1.0×10^{-3} to 15×10^{-3} M. In addition, 2.0×10^{-3} M Gly or Trp was added to NaAOT solution of 10×10^{-3} M in methanol/water to make amino acid-containing NaAOT solutions. To assist deprotonation of Trp, 10×10^{-3} M

NaOH was added to the NaAOT/Trp solution, achieving a solution pH of 11.74. All solutions were sonicated for 10 min to help desolvation and degassing before ESI.

Table 5.1 Key operating parameters of the mass spectrometer in negative ion mode[8]

ESI flow rate	0.03 or 0.04 ml•hr^{-1}
ESI bias voltage	-1,900 – -2,400 V
Capillary bias voltage	-200 V
Capillary temperature	150 °C
Skimmer bias voltage	-25 V
Pressure in hexapole ion guide	15 – 24 mTorr

CID was measured for both empty and amino acid-containing micellar aggregates. Given the large m/z ratios of heavy ions to light neutral gas in this experiment, E_{col} was varied modestly from 0.5 to 2.0 eV for CID experiments, and similar fragmentation patterns of selected precursor aggregate ions were observed. CID product ion mass spectra of mass-selected negatively charged NaAOT aggregates were measured at E_{col} = 1.0 eV so that the results can be directly compared with those of positively charged aggregates obtained at the same E_{col}, to better understand the effects of charge state on micellar structures and encapsulation properties. Due to low product ion intensities, the cell pressure was set at 0.3 mTorr to achieve a good signal-to-noise ratio. However, precursor aggregate ions and product ions underwent multiple collisions at this pressure, making it impossible to determine cross section for each dissociation channel.

5.3 Results and discussion

5.3.1 Formation of multiply negatively charged NaAOT aggregates

In order to investigate the effects of ESI solution conditions on the size, charge and intensity distributions of gas-phase NaAOT aggregates, mass spectra were measured for a series of solutions with NaAOT concentration varying from 1.0 × 10^{-3} (below CMC of 2.5 ×

10^{-3} M in aqueous solution⁵) to 15 × 10^{-3} M. Despite a wide variation in solution concentration, the abundance profiles of negatively charged gas-phase aggregates were nearly identical under all conditions, except that the absolute intensities of all aggregates increased significantly when a high concentration was used. When NaAOT concentration exceeded 15 × 10^{-3} M, a progressively growing background started to become significant; in the meantime, the absolute intensities of major peaks remained the same. Based on the quality of spectra, 10 × 10^{-3} M was chosen as the optimal concentration for all the rest experiments. The mass spectrum obtained at this concentration is demonstrated in Figure 5.1a.

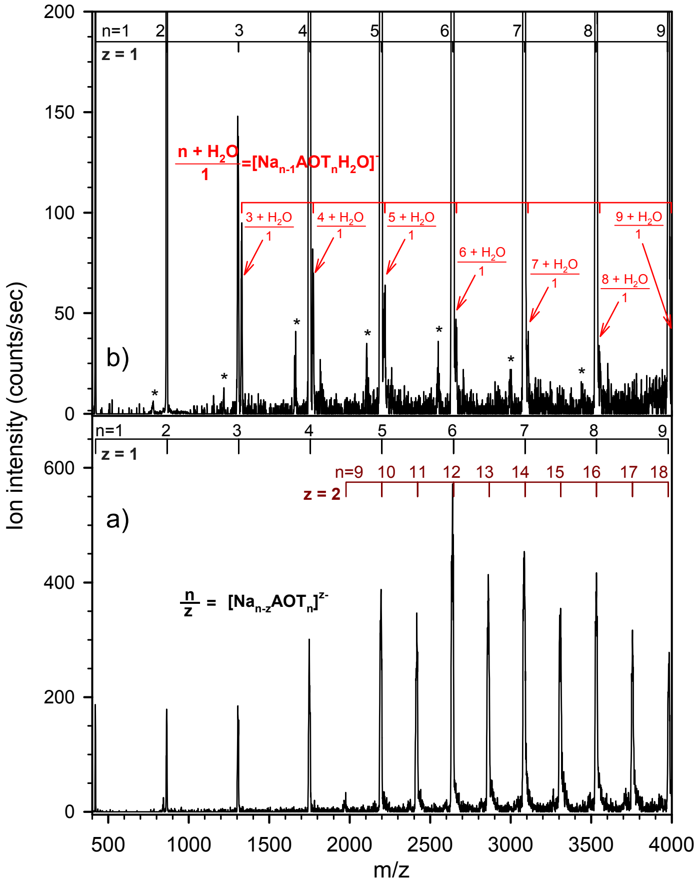

Figure 5.1 Negative ESI mass spectra of a methanol/water solution of 10 × 10^{-3} M NaAOT. Voltages applied to the capillary and the skimmer are a) -200 V and -25 V, and b) -300 V and -58 V, respectively. The features noted with '*' are due to fragmentation clusters, as explained in the text.

It is worth to mention that a similar phenomenon was observed concerning ESI solution conditions in my previous study of positively charged NaAOT aggregates in the gas phase[7]. As discussed in chapter 3, NaAOT concentration in methanol/water was varied from 0.7×10^{-3} to 5.0×10^{-3} M to bracket the CMC. No difference was found in the size and charge distributions of resulting $[Na_{n+z}AOT_n]^{z+}$ aggregates, no matter whether or not the solution concentration was above the CMC. Hence, in both positive and negative ion modes, NaAOT concentration did not affect the evolution of gas-phase aggregates. It follows that, ESI mass spectra did not mirror NaAOT aggregation states in solution[9]; instead, aggregation of NaAOT took place between ESI and exposure to the high vacuum of the mass spectrometer.

The mass peaks observed in Figure 5.1a could be attributed to the compositions of $[Na_{n-z}AOT_n]^{z-}$ with the aggregation number $n = 1 - 18$ and negative charge $z = 1 - 2$. The progressions of the same charge numbers were grouped together in the figure, and aggregates were indicated as *n/z* for convenience in the following discussion. Each aggregate lacked 1 – 2 Na^+ counterions, which accounted for its overall charge number. Singly charged aggregates started with monomer AOT^-, while doubly charged aggregates emerged from the aggregation number of 9. Relative abundance of singly charged aggregates (after subtracting the share of doubly charged species at the same *m/z* position) increased gradually till the maximum at 4/1, and then decreased. Doubly charged species exhibited a similar profile of ion intensity vs. aggregation number with a maximum intensity at 13/2; however, doubly charged species bore much higher intensities than neighboring singly charged ones. The actual maximum aggregation number for charged aggregates could be larger, since the largest detected aggregation number for each progression (*i.e.* 9 for $z = 1$ and 18 for $z = 2$) had approached the *m/z* detection limit of mass filters. However, "undetected" large aggregates would be less likely to have high abundance based on the ion intensity profiles depicted in Figure 5.1a.

It is noteworthy that NaAOT aggregates could only hold at most two extra charges in negative ion mode, much less than the extra charges they were able to carry in positive ion mode, *i.e.*, $z = 1 - 5$ for $[Na_{n+z}AOT_n]^{z+}$[7]. This may imply a different way in which coulombic repulsion affects the stability of negatively charged aggregates compared to their positively charged analogues, which in turn limits the size of aggregates in negative ion mode.

In addition, negative ESI mass spectra of NaAOT aggregates showed some differences than those reported by Bongiorno *et al.*[10] and Giorgi *et al.*[11]. Although solutions were prepared in a similar manner, their negative ESI mass spectra corresponded to only monocharged $[Na_{n-1}AOT_n]^-$, which paralleled monocharged $[Na_{n+1}AOT_n]^+$ in their positive ESI mass spectra. Multiply charged species had been detected in both positive[7] (as discussed in previous chapters) and negative ion modes. The mass spectra in this study showed that, 4/1 exhibited the highest abundance among negatively monocharged species; while in their mass spectra the monomer 1/1 was the most intense peak followed by the dimer 2/1. These discrepancies were most likely related to the differences in ESI and instrument conditions which were factored into the interactions of gas-phase surfactants and hence the distributions of gas-phase aggregates[7]. For these reasons, all experimental date were collected under nearly identical conditions, unless specified otherwise.

5.3.2 Solvation of small negatively monocharged NaAOT aggregates

In the present study, solvent molecules were mostly excluded in negatively charged aggregates, similar to their positively charged analogues described in chapter 3, yielding "dry" $[Na_{n-z}AOT_n]^{z-}$, as demonstrated in Figure 5.1a. This provided further evidence that surfactant-surfactant interactions were an overwhelming driving force for self-assembling of NaAOT in the gas phase[12]. Solvent molecules were not necessary for building a large gas-phase aggregate architecture[7], neither were they required for entrapping guest molecules (*vide infra*). In fact, while solvation of small gas-phase AOT-divalent metal ion clusters has been recently detected[13], such as solvated monomeric aggregates $[MgAOT(CH_3OH)_2]^+$, $[MgAOT(CH_3OH)H_2O]^+$ and $[CaAOT(CH_3OH)]^+$ and dimeric aggregate $[NiAOT_2(CH_3OH)]^+$, solvated NaAOT aggregates has not been reported yet.

The experiment revealed that, among instrument operating parameters, the capillary-skimmer potential was most critical for the intensity and size distributions of aggregate ions. Therefore a control experiment was carried out under the same condition as used for Figure 5.1a except that the voltages applied on capillary and skimmer were increased to -300 V and -58 V, respectively. In this case, only monocharged aggregates $[Na_{n-1}AOT_n]^-$ of $n = 1 - 9$ were detected (Figure 5.1b). This phenomenon could be attributed to the fact that multiply charged species were more sensitive to the capillary-skimmer potential. They would gain higher translation energy than singly charged species in the same electrical field, and thus could not survive in-source CID. Similar results were observed in positive ESI mass spectra of NaAOT aggregates[7]. Accordingly, the high electrical field between the capillary and skimmer was unfavorable for aggregation and micellation. Interestingly, only under this high electrical field a new series of clusters emerged, which could be assigned to solvation of aggregates by single water molecules, *i.e.*$[Na_{n-1}AOT_nH_2O]^-$ ($n = 3 - 9$) as indicated in Figure 5.1b. The intensities of solvated aggregates were less than 5% of corresponding "dry" aggregates, monotonously decreasing with increasing aggregate size. When pure methanol was used as the ESI solvent, these solvated aggregates mostly disappeared. Therefore, these results complemented the observation of water solvated NaAOT aggregates in the gas phase. In addition to $[Na_{n-1}AOT_nH_2O]^-$, another series of low intensity aggregates were observed (marked with asterisks in Figure 5.1b). It started at *m/z* of 778 with neighboring peaks differed by the number of NaAOT unit. This series were tentatively attributed to either an impurity present in NaAOT, or fragment ions formed during in-source collisions of "dry" aggregates.

5.3.3 Incorporation of amino acids within negatively charged NaAOT aggregates

Neutral Gly A simple amino acid without a side chain would facilitate identification of key factors in gas-phase micellar entrapment. Based on this consideration, Gly was chosen as the first guest molecule for the incorporation experiment. In this experiment, NaAOT solution was prepared in methanol/water, into which Gly was added ([NaAOT] = 10.0×10^{-3} M and [Gly] = 2.0×10^{-3} M). The negative ESI mass spectrum of NaAOT/Gly solution is shown in Figure 5.2. The most intense ion peaks in the mass spectrum were assigned to empty aggregates *n/z*, and their abundance features were similar to those observed in Figure 5.1a. In the *m/z* range below 2,000, mass spectrum of NaAOT/Gly was indistinguishable from that of pure NaAOT, suggesting that in this m/z range gas-phase aggregates were unoccupied. Occupied aggregates were observed in the m/z range above 2,000, featuring the compositions of $[\mathrm{Na}_{n-z}\mathrm{AOT}_n\mathrm{Gly}_m]^{z-}$ where m is the number of Gly molecules entrapped. These species are highlighted in pink in the figure, and labeled as *(n + mG)/z*. Note that there is *m/z* coincidence between singly and doubly charged species, for example, *(7+G)/1* and *(14+2G)/2*; for these species both assignments were given. It was found that, the entrapment capability of aggregates strongly correlated with their sizes. No entrapment of Gly was detected for aggregates of $n < 7$. Aggregates of $n \geq 7$ may accommodate single Gly, and up to two Gly molecules can be accommodated in aggregates of $n \geq 13$.

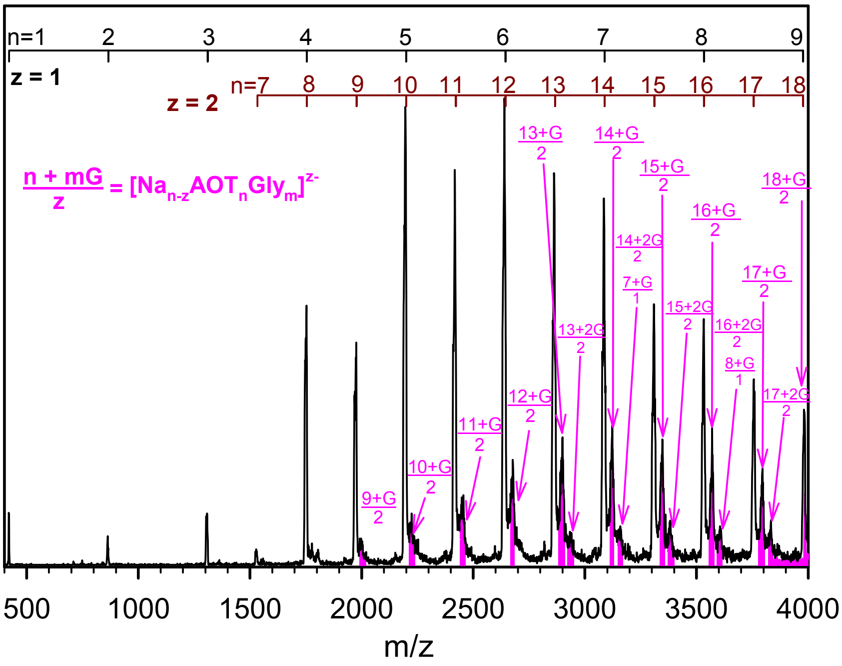

Figure 5.2 Negative ESI mass spectrum of a methanol/water solution containing 10 × 10^{-3} M NaAOT and 2.0 × 10^{-3} M Gly.

Neutral Trp The Trp side chain (*i.e.* indole ring) is the most hydrophobic of all amino acid side chains, and aqueous solubility of Trp is 1.38 g/100 g water at 25 °C (compared to 25.16 g/100 g water for Gly)[14, 15]. Comparison of neutral Gly and Trp as guest molecules would allow for examination of hydrophobic effects in gas-phase micellar solubilization, and similar approaches were used to determine the driving forces for the solubilization of amino acids in solution-phase NaAOT reverse micelles[16-19]. Negative mass spectrum of NaAOT/Trp was measured using a solution of NaAOT (10 × 10^{-3} M) and Trp (2 × 10^{-3} M) in methanol/water. *p*H of this solution was measured to be 6.5, slightly higher than Trp isoelectric point *p*I of 5.9 in aqueous solution[20]. As shown in Figure 5.3a, neutral Trp was incorporated into $[Na_{n-z}AOT_n]^{z-}$ to form $[Na_{n-z}AOT_nTrp_m]^{z-}$ where m is the number of Trp entrapped. They are labeled as $(n + mW)/z$ in the figure, where W designates Trp. For the sake of clarity in showing the assignments of $(n + mW)/z$, the m/z range below 1,400 is not shown in the figure, since no Trp signal was discernible in that range. In contrast to its low incorporation capability for Gly, each aggregate could entrap up to four Trp molecules, and there was no obvious correlation between aggregate size and the maximum number of Trp molecules each aggregate may host. In the figure all empty and Trp-entrapping aggregates associated with the same aggregate number are linked together, and aggregates with various values of *m* are shaded in different colors.

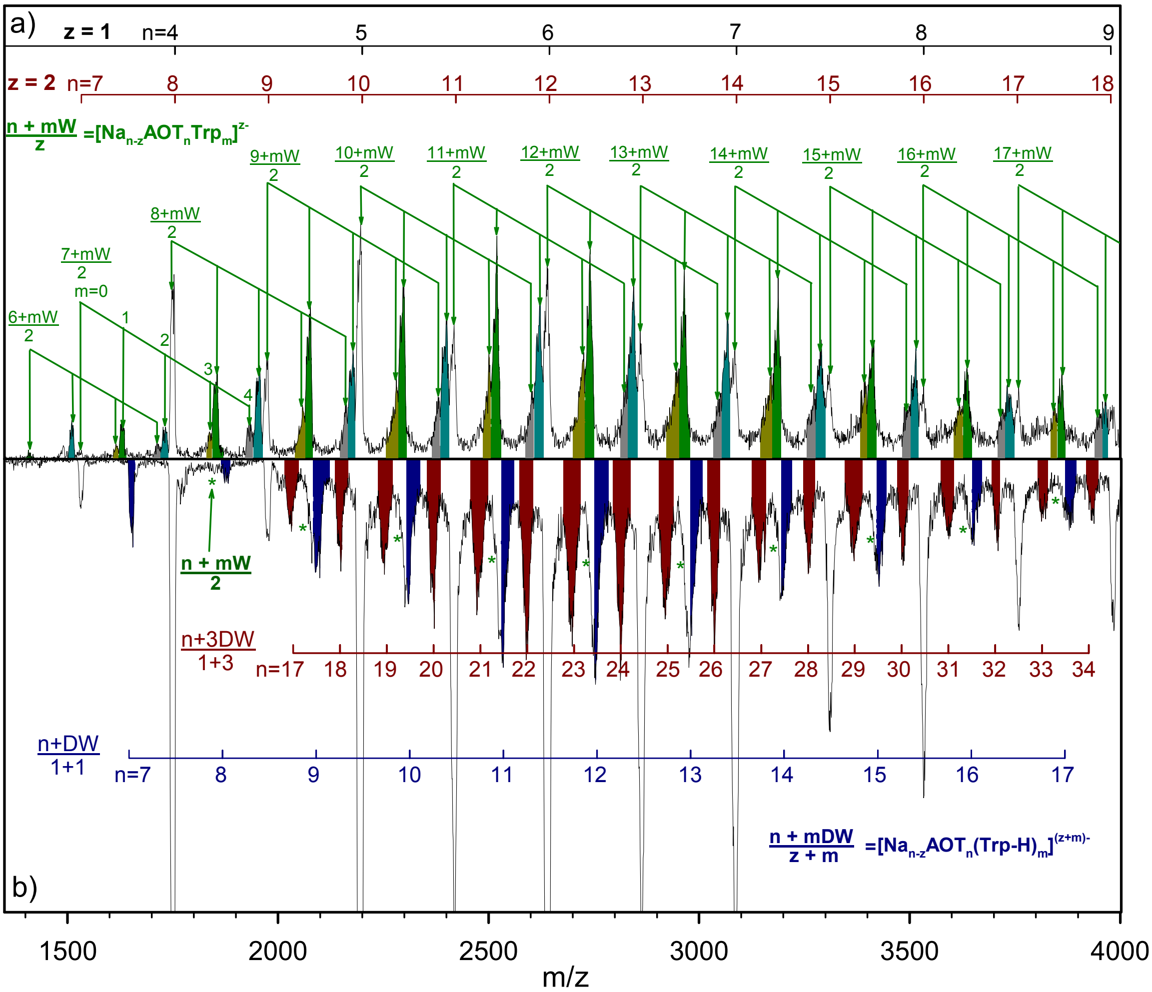

Figure 5.3 Negative ESI mass spectra of a methanol/water solution containing a) 10 × 10^{-3} M NaAOT and 2.0 × 10^{-3} M Trp, and b) 10 × 10^{-3} M NaAOT, 2.0 × 10^{-3} M Trp, and 10 × 10^{-3} M NaOH.

To quantitatively compare incorporation capability of the same aggregate towards Gly and Trp, relative incorporation efficiencies defined as

$$E_G = \frac{I([Na_{n-z}AOT_nGly]^{z-})}{I([Na_{n-z}AOT_n]^{z-})} \qquad (1)$$

$$E_W = \frac{I([Na_{n-z}AOT_nTrp]^{z-})}{I([Na_{n-z}AOT_n]^{z-})} \qquad (2)$$

were calculated in a similar manner as discussed in chapter 4, where $I([\mathrm{Na}_{n\text{-}z}\mathrm{AOT}_n]^{z-})$, $I([\mathrm{Na}_{n\text{-}z}\mathrm{AOT}_n\mathrm{Gly}]^{z-})$ and $I([\mathrm{Na}_{n\text{-}z}\mathrm{AOT}_n\mathrm{Trp}]^{z-})$ represented ion intensities of empty aggregates and aggregates containing Gly and Trp in corresponding mass spectra, respectively.

One issue in mass spectral measurements is that there were m/z coincidences among different charged states. Intensities of singly charged aggregate ions are masked by the shares of doubly charged ions at the same m/z positions. For example, m/z of 2,644 represents two overlapping charge states, 6/1 and 12/2. To avoid complication arising from m/z coincidence of selected host aggregate ions with other charge states, $[\mathrm{Na}_{n\text{-}z}\mathrm{AOT}_n]^{z-}$ of 7/2, 9/2, 11/2, 13/2, 15/2 and 17/2 were chosen as hosts for analysis. $[\mathrm{Na}_{n\text{-}z}\mathrm{AOT}_n]^{z-}$ may each incorporate more than one Gly and Trp molecule; however, incorporation of multiple Gly or Trp was not included in E_G or E_W. This omission was deliberate, since small $[\mathrm{Na}_{n\text{-}z}\mathrm{AOT}_n]^{z-}$ can only take one Gly each. To enable direct comparison of incorporation efficiencies of different aggregate sizes and towards different amino acids, this experiment focused on incorporation of single amino acid. Calculation results, averaged over at least two replicate sets of mass spectra, are summarized in Table 5.2. These results gave very rough estimates, but were sufficient to reveal general trends.

Remarkable differences between values of E_G and E_W arose from distinct electrostatic and hydrophobic interactions involved in amino acid incorporation. For Gly, there was no hydrophobic interaction and an attractive electrostatic potential was essential for its solubilization into aggregates. In contrast, Trp is the most hydrophobic amino acid[14, 15]. As shown by the ratios of E_W/E_G listed in Table 5.2, hydrophobicity dramatically increased the incorporation of Trp into aggregates by a factor of 9 – 14. But the enhancement decreased rapidly with increasing aggregate size, and approached a minimum for aggregate of 17/2.

Table 5.2 Incorporation efficiencies of Gly (G) and Trp (W) in gas-phase negatively (and positively) charged NaAOT aggregates.

Negative host aggregates	$E_G{}^b$	$E_W{}^b$	$E_W/E_G{}^b$
$\frac{7}{2}$	–	5.6	–
$\frac{9}{2}$	0.12	1.7	14
$\frac{11}{2}$	0.18	1.6	9
$\frac{13}{2}$	0.33 (0.60)	1.5 (0.34)	4.5 (0.57)
$\frac{15}{2}$	0.48 (0.90)	1.3 (0.62)	2.7 (0.69)
$\frac{17}{2}$	0.54 (1.50)	1.2 (0.70)	2.2 (0.47)

[a] Host aggregates are indicated as $\frac{n}{z}$, where n is the aggregation number, and z is the total charge.

[b] Values in parentheses are incorporation efficiencies of Gly and Trp in positively charged aggregates, and their ratios, respectively.

Deprotonated Trp Solubilization of neutral Trp can be attributed to hydrophobic effects. To distinguish the roles of hydrophobic and electrostatic interactions in micellar solubilization of the same amino acid, *p*H of the NaAOT/Trp solution was adjusted to 11.74 by adding 10 × 10^{-3} M NaOH. Under this circumstance, deprotonated Trp was carried into negatively charged aggregates. The resulting spectrum (Figure 5.3b) demonstrated notable differences than that of neutral Trp (Figure 5.3a). Similar to that of NaAOT/Gly, this mass spectrum was overwhelmingly dominated by empty aggregates. In addition, two series of

$[\mathrm{Na}_{n\text{-}z}\mathrm{AOT}_n(\mathrm{Trp\text{-}H})_m]^{(z+m)-}$ aggregates were identified, corresponding to aggregates containing one and three deprotonated Trp (hereafter designated as DW), respectively. These two series are indicated in dark blue and red shaded areas in Figure 5.3b, and labeled as $(n + DW)/(1 + 1)$ where $n = 7 - 17$ and $(n + 3DW)/1{+}3$ where $n = 17 - 34$, respectively. It is somewhat puzzling that no aggregates containing two DW were detected. Note that $(n + DW)/(1 + 1)$ partially overlapped with $(n + W)/2$ (which are marked with green asterisks in Figure 5.3b) because of the ionization equilibrium between deprotonated and neutral Trp in ESI solution and spray droplets.

As incorporation of deprotonated Trp only happened for monocharged $[\mathrm{Na}_{n\text{-}1}\mathrm{AOT}_n]^-$, the relative incorporation efficiencies for deprotonated Trp were not compared with those for neutral Gly and Trp. However, deprotonation of Trp significantly reduced its incorporation into aggregates, making it resemble Gly in terms of incorporation efficiencies. This reduction may be explained by the displacement of Trp from the interfacial region close to apolar tails to the place near polar heads/counterions upon deprotonation. It implied that, while hydrophobic effects between Trp side chain and surfactant apolar tails dominated Trp incorporation, these effects were compromised by electrostatics between Trp charged backbone and surfactant polar heads.

Comparison with encapsulation properties of positively charged aggregates It would be interesting to compare the entrapment properties of negatively charged NaAOT aggregates with those of positively charged $[\mathrm{Na}_{n+z}\mathrm{AOT}_n]^{z+}$ reverse micelles reported in chapter 4. $[\mathrm{Na}_{n+z}\mathrm{AOT}_n]^{z+}$ started encapsulation of a Gly molecule from $n = 13$, and those of $n \geq 16$ could encapsulate two Gly molecules. Up to three Gly molecules could be encapsulated in single $[\mathrm{Na}_{n+z}\mathrm{AOT}_n]^{z+}$ of $n \geq 17$, four Gly molecules in those of $n \geq 21$, and five in those of $n \geq 24$. This strong size dependence of encapsulation capability supported a reverse micelle-like structure for $[Na_{n+z}AOT_n]^{z+}$. Assuming $[Na_{n+z}AOT_n]^{z+}$ was spherical and Gly molecules were all encapsulated within the micellar core, the maximum number of encapsulated Gly molecules did indeed match the core size of the reverse micelle. On the other hand, incorporation of neutral Trp into $[Na_{n+z}AOT_n]^{z+}$ started from $n = 10$, and each $[Na_{n+z}AOT_n]^{z+}$ reverse micelle could only take at most one neutral Trp molecule. Consistent with a reverse micellar structure, Trp was interpreted to be intercalated between AOT tails at the reverse micellar interface. Small $[Na_{n+z}AOT_n]^{z+}$ reverse micelles had large curvatures; and consequently could not provide enough interfacial area (near head regions) for incorporating more than one Trp molecule.

It is surprising that the negative charge state of NaAOT aggregates dramatically affects their incorporation behaviors towards Gly *vs.* Trp, yielding distinctly different results. $[Na_{n-z}AOT_n]^{z-}$ required lower aggregation number to entrap Gly molecules; in the meantime, incorporation of more than two Gly molecules was not observed in single $[Na_{n-z}AOT_n]^{z-}$. Moreover, each $[Na_{n-z}AOT_n]^{z-}$ can entrap four neutral Trp molecules, and the efficiency for incorporating the second Trp molecule was comparable to that for the first one. For comparison, the incorporation efficiencies for Gly and Trp have been included in Table 5.2 in positively charged NaAOT aggregates, respectively[7, 21]. It is obvious that $[Na_{n+z}AOT_n]^{z+}$ and $[Na_{n-z}AOT_n]^{z-}$ presented opposite affinities towards hydrophilic Gly and hydrophobic Trp, as exemplified by the values of E_G/E_W for corresponding positively and negatively charged aggregates. This hinted that $[Na_{n+z}AOT_n]^{z+}$ and $[Na_{n-z}AOT_n]^{z-}$ may have different mechanisms to accommodate guest molecules.

5.3.4 CID of negatively charged NaAOT aggregates

Empty aggregates For CID experiments, four doubly charged aggregates with odd aggregation numbers (*i.e.*, 11/2, 13/2, 15/2, and 17/2) were chosen as precursor ions, so that each of these precursor ions could be cleanly mass-selected and corresponded to a unique aggregation number. This circumvented the complications of *m/z* coincidences with other species. CID mass spectra described below were obtained at E_{col} = 1.0 eV and with 0.3 mTorr Xe in the scattering cell. The values of E_{col} and cell pressure were the same as those used for positively charged aggregates in previous chapters,[7, 21] enabling a direct comparison of these results from two different charge states.

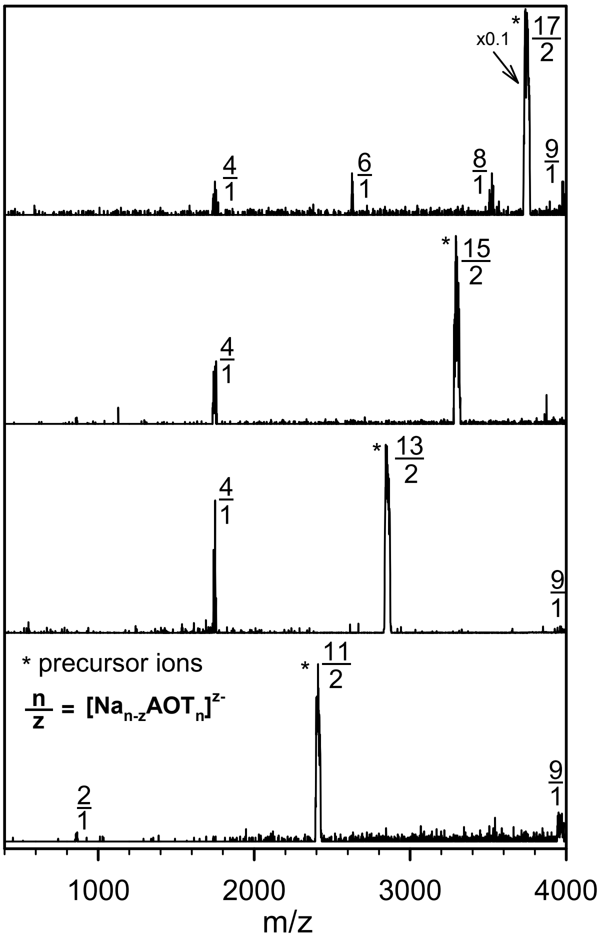

Figure 5.4 CID mass spectra of mass-selected negatively charged NaAOT aggregates. Spectra were measured at E_{col} = 1.0 eV, with 0.3 mTorr Xe in the scattering cell. Asterisks indicate precursor ions.

Figure 5.4 shows the product ion mass spectra from CID of mass-selected precursor ions. Because of multiple collisions between precursor ions and Xe at a high gas pressure (and primary fragment ions may continue to undergo collisions that cause secondary dissociations), relative intensities of product ions in the spectra do not reflect branching ratios. However, all product ions in this figure were detected under single-collision condition as well.

Dissociation product ions for all selected precursor ions are summarized in Table 5.3. Also included in the table are dissociation efficiencies (*Diss%*), estimated as

$$Diss\% = \frac{\Sigma\, I(\text{monocharged fragment ion})/2}{\Sigma\, I(\text{monocharged fragment ion})/2 + I(\text{doubly charged precursor ion})} \tag{3}$$

for each precursor ion. CID of doubly charged precursor ions exclusively produced two monocharged species. Both complementary product ions produced from a single dissociation of a doubly charged precursor ion, were detected and are included in the table, unless otherwise stated. Some fragment ion peaks may be attributed to more than one product ion because of the m/z overlapping of singly and doubly charged species. However, based on the trend in product ion charge state distributions, the contributions of doubly charged product ions were less likely to be significant. Most precursor ions had only one dissociation channel, with the exception of the largest one 17/2, which dissociates into 4/1 + 13/1, 6/1 + 11/1, and 8/1 + 9/1, respectively. Dissociation efficiency strongly depended on the aggregate size, increasing from 9% for 11/2 to 25 – 26% for 13/2 and 15/2, and dropping to only 5% for 17/2 suggesting the exceptionally high stability of 17/2.

Aggregates containing Gly and Trp Distinct than that of empty aggregates, CID of aggregates containing guest molecules involved a competition between stripping surfactants and expelling entrapped guest molecules. Such competition was driven by precursor ion structures and the stability of resulting neutral and charged products[7, 21]. To enable a direct comparison with empty aggregates, Gly and Trp-containing precursor aggregates with the same aggregation and charge numbers as those chosen for empty aggregates were selected, i.e., (11 + G or W)/2, (13 + G or W)/2, (15 + G or W)/2, and (17 + G or W)/2.

Table 5.3 Summary of CID products and dissociation efficiencies of empty and amino acid-containing negatively charged NaAOT aggregates

Empty precursor ions [a]	Dissociation channels [b]	Precursor ions containing Gly[a]	Dissociation channels [b]	Precursor ions containing Trp [a]	Dissociation channels [b]
$\frac{11}{2}$	$\frac{2}{1}+\frac{9}{1}$ (9%)	$\frac{11+G}{2}$	$\frac{11}{2}+G$ (51%)	$\frac{11+W}{2}$	$\frac{11}{2}+W$ (10%)
$\frac{13}{2}$	$\frac{4}{1}+\frac{9}{1}$ (26%)	$\frac{13+G}{2}$	$\frac{13}{2}+G$ (73%)	$\frac{13+W}{2}$	$\frac{13}{2}+W$ (7%)
$\frac{15}{2}$	$\frac{4}{1}+\frac{11^c}{1}$ (25%)	$\frac{15+G}{2}$	$\frac{15}{2}+G$ (42%)	$\frac{15+W}{2}$	$\frac{15}{2}+W$ (15%)
$\frac{17}{2}$	$\frac{8}{1}+\frac{9}{1}$ $\frac{6}{1}+\frac{11^c}{1}$ $\frac{4}{1}+\frac{13^c}{1}$ (total 5%)	$\frac{17+G}{2}$	$\frac{17}{2}+G$ (53%)	$\frac{17+W}{2}$	$\frac{17}{2}+W$ (10%)

[a] Precursor and fragment ions are indicated as $\frac{n}{z}$ for empty aggregates, $\frac{n+mG}{z}$ for those containing Gly (G), and $\frac{n+mW}{z}$ for those containing Trp (W), where *n* is the aggregation number, *z* is the total charge, and *m* is the number of incorporated amino acid molecules.

[b] Given in parentheses are the dissociation efficiencies, estimated as

$$\frac{\sum I(\text{monocharged fragment ion})/2}{\sum I(\text{monocharged fragment ion})/2 + I(\text{doubly charged precursor ion})}$$ for empty aggregates, and

$$\frac{I(\text{fragment ion})}{I(\text{fragment ion}) + I(\text{precursor ion})}$$ for aggregates containing amino acid.

[c] Beyond the *m/z* detection limit of the mass spectrometer.

Shown in Figures 5.5a and b are CID mass spectra of negatively charged NaAOT aggregates containing Gly and Trp, respectively. These mass spectra clearly revealed that only one dissociation channel existed for each of these precursor aggregate ions, corresponding to striping of Gly (or Trp), and only Gly (or Trp), off aggregates. This finding indicated that both Gly and Trp may be attached to the exterior of aggregate structures. As opposite to being encapsulated within the aggregate core, an amino acid anchored onto the outer surface could be easily knocked off by Xe collision without collapse of the remaining aggregate.

A comparison of dissociation efficiencies was made between aggregates containing Gly and Trp. As summarized in Table 5.3, the dissociation efficiency increased with the aggregate size in both systems, except for (13 + G)/2 which presented abnormally high dissociation efficiency. Under the same CID conditions, the dissociation efficiencies for aggregates containing Gly were higher than those containing Trp by a factor of 3 – 5 or more. In fact, dissociation efficiencies of Trp-containing aggregates were more or less comparable that of empty aggregates. This result was in accordance with the implication of incorporation efficiencies (Table 5.2), and reinforced that hydrophobic Trp has a higher affinity to NaAOT surfactants than hydrophilic Gly.

In view of the fact that deprotonated Trp combines hydrophobic side chain and charged hydrophilic backbone, CID of aggregates containing deprotonated Trp could be another ideal system for probing entrapment properties of negatively charged aggregates. Unfortunately, NaAOT aggregates containing deprotonated Trp co-exist and overlap with those containing neutral Trp in mass spectra, preventing the possibility of selection of "clean" deprotonated Trp-containing precursor ions for CID.

Comparison with CID of positively charged aggregates It is informative to compare CID products of positively and negatively charged empty aggregates of the same size. To differentiate the charge state for the same aggregation number, the sign of charge was included in the superscript of the acronym, *e.g., n/z*$^+$ for $[Na_{n+z}AOT_n]^{z+}$ and *n/z*$^-$ for $[Na_{n-z}AOT_n]^{z-}$. As discussed in chapter 3, the major CID channels of $[Na_{n+2}AOT_n]^{2+}$ corresponded to divisions of the precursor ion into two nearly equally-sized monocharged product ions[7], referred to as "symmetric fission"[22]. For instances, $13/2^+ \rightarrow 6/1^+ + 7/1^+$, $15/2^+ \rightarrow 7/1^+ + 8/1^+$, and $17/2^+ \rightarrow 8/1^+ + 9/1^+$. On the contrary, the sizes of two fragment ions produced from a $[Na_{n-2}AOT_n]^{2-}$ aggregate differed greatly, *exhibiting an* asymmetric division to one larger and one smaller species such as $13/2^- \rightarrow 4/1^- + 9/1^-$, $15/2^- \rightarrow 4/1^- + 11/1^-$, and $17/2^- \rightarrow 6/1^- + 11/1^-$.

It is more instructive to compare CID of amino acid-containing NaAOT aggregates in different charged states. The most profound difference was found in Gly-containing aggregates. Dissociation of positively charged Gly-containing aggregates produced various product ions, some of which were still able to entrap Gly. This had been taken as a strong piece of evidence that Gly was protected within the interior of a reverse micelle. By contrast, for negatively charged aggregates only Gly was eliminated without losing NaAOT units. CID of Trp-containing NaAOT aggregates went to another extreme, where all occupied aggregates expelled Trp only, despite the aggregate charge states.

5.3.5 What structure may gas-phase negatively charged NaAOT aggregates possess?

Before analyzing what mass spectrometry study could reveal about the structure of negatively charged NaAOT aggregates, it is useful to emphasize the differences from a comparative analysis of negatively charged $[Na_{n-z}AOT_z]^{z-}$ and positively charged $[Na_{n+z}AOT_z]^{z+}$, the latter of which could form reverse micelle in the gas phase[7, 21]. First,

$[Na_{n+z}AOT_z]^{z+}$ reverse micellar ions can accommodate up to five extra charges, while $[Na_{n-z}AOT_z]^{z-}$ aggregates can only hold two extra charges. Secondly, $[Na_{n+z}AOT_z]^{z+}$ ions showed a high encapsulation capability towards hydrophilic Gly with a strong size dependence, yet a limited incorporation capability towards hydrophobic Trp. $[Na_{n-z}AOT_z]^{z-}$ aggregates presented opposite behaviors, showing a much higher entrapping capability towards Trp (without aggregate size dependence) than towards Gly. Thirdly, protonation of Trp significantly improved its incorporation into $[Na_{n+z}AOT_z]^{z+}$ as it displaced Trp from the micellar interfacial zone to the core, whereas deprotonation of Trp dramatically decreased its incorporation into $[Na_{n-z}AOT_z]^{z-}$. Fourthly, CID of $[Na_{n+z}AOT_zGly]^{z+}$ led to various fragments, and expelling of Gly resulted in breakdown of the micellar structure. On the other hand, CID of $[Na_{n+z}AOT_zTrp]^{z+}$ corresponded to striping only Trp off reverse micelles. These CID patterns were attributed to different site locations of amino acids within reverse micelles. In other words, Gly was encapsulated into the micellar core while Trp was intercalated at the micellar interface. Conversely, for CID of negatively charged aggregates containing Gly and Trp, the above described difference vanished. At the same E_{col} used for positively charged reverse micelles, both Gly- and Trp-containing negatively charged aggregates ejected only amino acid. These dissimilarities indicate that, different than the expectation for reverse micellar incorporation, both Gly and Trp were loosely attached to negatively charged micelles.

These discrepancies led to clues regarding possible $[Na_{n-z}AOT_z]^{z-}$ structures in the gas phase. Bongiorno *et al.*[10, 23] and Giorgi *et al.*[11] reported gas-phase negatively monocharged NaAOT aggregates. Bongiorno *et al.* calculated the energy changes accompanying the formation of reverse and direct micelles for neutral, positively and negatively singly charged AOT trimers, and found the electrostatic interactions among surfactant head groups are larger than apolar-apolar interactions among surfactant alkyl chain which would favor a reverse micellar model for these trimers. MD simulations[24] suggested that, positively and negatively singly charged and neutral NaAOT aggregates may all form reverse micelle-like structures; however, negatively charged aggregate were the least stable and had larger total gyration radius (including all atoms) and core gyration radius (including core atoms only) than the same size neutral and positively charged aggregates. This implies additional repulsive effect for a negatively charged aggregate if existing in a reverse micellar structure.

Compared to singly charged aggregates, multiply charged aggregates brought about more intense coulombic repulsion. One way towards understanding the structures of multiply charged aggregates is to identify different effects of extra positive and negative charges. The presence of Na^+ counterions in the $[Na_{n+z}AOT_z]^{z+}$ reverse micelle allowed the repulsive interaction of AOT negative polar heads to be overcome; and extra Na^+ ions improved this gluing effect. This scenario raised a related question. Would multiply charged $[Na_{n+z}AOT_z]^{z+}$ be destabilized because of coulombic repulsion when Na^+ ions were too close to each other? Based on a direct optimization of dry, isolated NaAOT reverse micelles[25] and MD simulations of low water content NaAOT reverse micelles in isooctane[26, 27], most Na^+ ions penetrated the AOT polar heads layer and coordinated with the sulfonate group. Some Na^+ ions existed outside and coordinated with the carbonyl group. Coordination of Na^+ with these oxygen atoms offered a favorable structure for $[Na_{n+z}AOT_z]^{z+}$. On the other hand, had $[Na_{n-z}AOT_z]^{z-}$ adopted a similar reverse micellar structure as $[Na_{n+z}AOT_z]^{z+}$, repulsive interactions among "unneutralized" AOT^- polar heads (localized in the micellar center) could not be "shielded" from each other. This would have induced inherent instability leading to disruption of the whole micellar structures.

Based on these considerations and our incorporation and CID results, a direct micelle-like model (which exposes polar heads) is proposed here, which might better describe the structures and encapsulation properties of multiply negatively charged aggregates than a reverse micelle-like model (with polar heads buried within the interior of the micelle). In a direct micelle-like structure, Gly may adsorb to the interface through electrostatics with NaAOT polar heads and counterions; Trp, due to its hydrophobic indole ring, may partially penetrate into the surfactant layer. The cartoons in Figures 5.5a and 5.5b illustrate direct micelle-like structures for Gly- and Trp-containing aggregates. These cartoons were not intended to describe the whole structures of respective aggregates, but to demonstrate the localization of Gly and Trp and how these guest amino acids were facilely eliminated during CID. A direct micelle-like structure explained the observation that $[Na_{n-z}AOT_z]^{z-}$ aggregates have a higher affinity towards Trp than towards Gly. Following the principle of "like dissolves like", Trp could penetrate into AOT apolar tails acting as a co-surfactant and consequently gained more space compared to Gly. It followed that Trp incorporation showed weak aggregate size dependence. Moreover, deprotonation of Trp introduced repulsion between Trp charged backbone and AOT polar head. This electrostatics tended to push Trp away from the micellar surface, leading to reduced incorporation efficiency. Finally, the fact that Xe collision could strip Gly or Trp off the host without breaking the host structure was consistent with location of guest molecule near the exposed layer of a direct micelle-like structure. And as Trp side chain and AOT tails coalesced into a more stable architecture, less fragmentation would be expected for aggregates containing Trp. It is worth noting that, in addition to spherical direct micelle, other structures such as helicoidal or rodlike micelle[28] with exposed polar heads, may also be in agreement with encapsulation and dissociation behaviors of NaAOT aggregates. However, a helicoidal or rodlike micelle with replicate structure units along one dimension are unable to explain the fact that, while hydrophobic effects increased the incorporation of Trp into aggregates, the enhancement decreased rapidly with increasing aggregate size (Table 5.2).

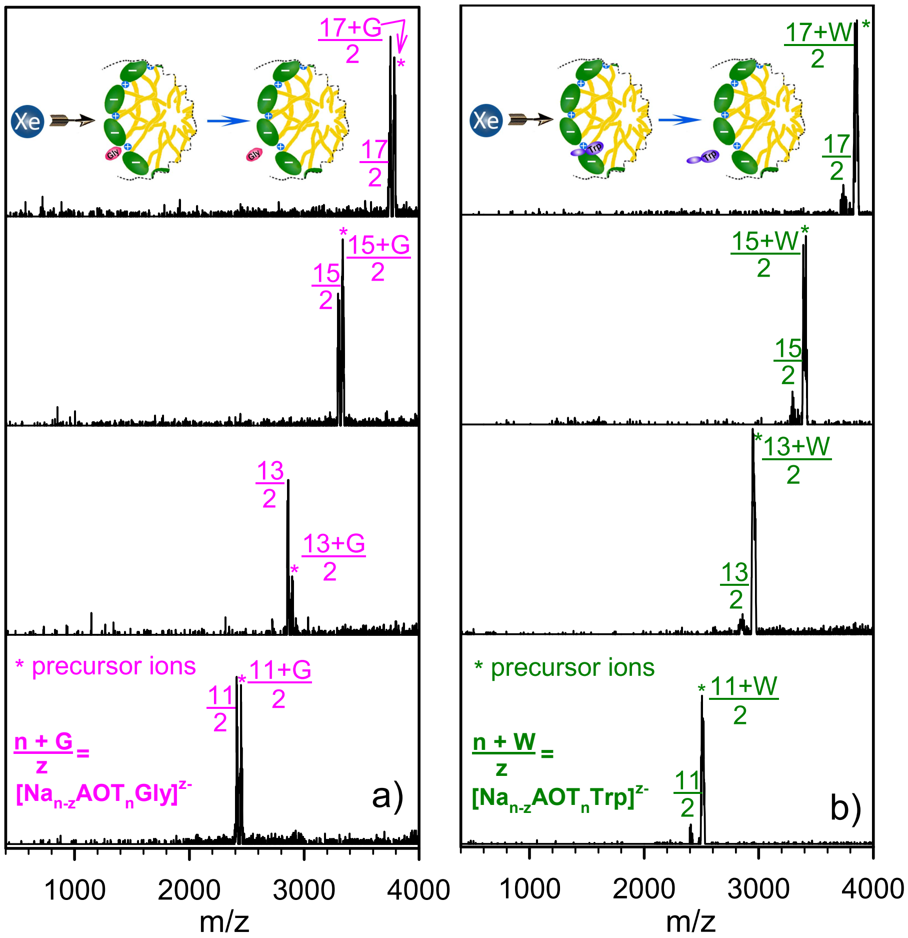

Figure 5.5 CID mass spectra of mass-selected negatively charged NaAOT aggregates containing a) Gly and b) Trp. All spectra were measured at E_{col} = 1.0 eV, with 0.3 mTorr Xe in the scattering cell. Asterisks indicate precursor ions. Inserted cartoons illustrate a) adsorption of Gly near surfactant polar heads and b) interfacial incorporation of Trp as a co-surfactant, respectively.

Note that gas-phase direct micelles have been reported previously for other systems, *e.g.*, 3-[(3-cholamidopropyl)-dimethylammonio]-1-propanesulfonate (CHAPS)[29], sodium dodecylsulfate (SDS) [29], bile salt[30], and decyltrimethylammonium bromide (DTAB) [31].

Particularly, Robinson *et al.* reported formation of gas-phase direct and reverse micelles using different ESI solutions of cetyltrimethylammonium bromide (CTAB)[28].

5.4 Conclusions

The experimental study presented in this chapter ascertained that NaAOT surfactants are able to form negatively multiply charged micelles in the gas phase with compositions of $[Na_{n-z}AOT_n]^{z-}$ where $n = 1 - 18$ and $z = 1 - 2$. Micellation occured via self-assembling of surfactants in the gas phase, and did not mirror aggregation states in ESI solutions. Solvation was only detected for small negatively charged aggregates, indicating that solvent-surfactant interactions were not essential for the formation of micelles in the gas phase. Incorporation of Gly, neutral and deprotonated Trp into $[Na_{n-z}AOT_n]^{z-}$ was achieved, respectively. Incorporation of hydrophilic Gly demonstrated strong aggregate size dependence. $[Na_{n-z}AOT_n]^{z-}$ of $n \geq 7$ could incorporate one Gly molecule, and those of $n \geq 13$ can incorporate two Gly molecules. In contrast, $[Na_{n-z}AOT_n]^{z-}$ showed a much higher incorporation capability towards hydrophobic Trp and could accommodate up to four Trp molecules each from the size of $n = 6$. However, deprotonation significantly reduced Trp incorporation. CID of negatively charged empty aggregates and those containing Gly and Trp was carried out. Fragmentation results were utilized to infer micellar ion structures and incorporation sites of amino acids, and hence to propose a direct micelle-like structure for these assemblies. These findings are different than those of positively charged NaAOT aggregates discussed in previous chapters, which had been proved to take a reverse micelle-like structure. It was concluded that micelles formed from the same solution but under different charge states exhibited markedly different mass spectra. More importantly, different charge states might affect resulting micellar structures, and consequently their incorporation behaviors.

Contrary to the general view that reverse micelle requires water molecules to “glue” the assembly, no water was found in gas-phase reverse micelles. It is speculated that, because of water shedding, more Na^+ is required to coordinate with AOT and support the reverse micellar structure. This finding implies potential applications of gas-phase reverse micelles in synthetic tasks where the absence of water is required for extremely aggressive chemistry.[32] CID was employed to provide insights into gas-phase reverse micellar structures, stability, and their dependence on micelle size.

References

1 K. Mukherjee, S. P. Moulik, and D. C. Mukherjee, *Langmuir,* 1993, 9, 1727-1730.

2 P. L. Luisi, M. Giomini, M. P. Pileni, and B. H. Robinson, *Biochim. Biophys. Acta,* 1988, 947, 209-246.

3 R. W. Gale, J. L. Fulton, and R. D. Smith, *J. Am. Chem. Soc.,* 1987, 109, 920-921.

4 M.-P. Pileni, *Natural Materials,* 2003, 2, 145-150.

5 E. F. Williams, N. T. Woodbery, and J. K. Dixon, *J. Colloid Interface Sci.,* 1957, 12, 452-459.

6 P. Mukerjee, and K. J. Mysels, *Critical Micelle Concentration of Aqueous Surfactant Systems* (Washington, DC: NSRDC-NBS 36, 1971).

7 Y. Fang, A. Bennett, and J. Liu, *Int. J. Mass Spectrom.,* 2010, 293, 12-22.

8 Y. Fang, F. Liu, and J. Liu, *Journal of The American Society for Mass Spectrometry,* 2012, submitted.

9 D. Bongiorno, L. Ceraulo, G. Giorgi, S. Indelicato, and V. T. Liveri, *J. Mass. Spectrom.,* 2011, 46, 1263-1268.

10 D. Bongiorno, L. Ceraulo, A. Ruggirello, V. T. Liveri, E. Basso, R. Seraglia, and P. Traldi, *J. Mass Spectrom.,* 2005, 40, 1618-1625.

11 G. Giorgi, E. Giocaliere, L. Ceraulo, A. Ruggirello, and V. T. Liveri, *Rapid Comm. Mass Spectrom.,* 2009, 23, 2206-2212.

12 L. Ceraulo, G. Giorgi, V. T. Liveri, D. Bongiorno, S. Indelicato, F. Di Gaudio, and S. Indelicato, *European Journal of Mass Spectrometry,* 2011, 17, 525-541.

13 G. Giorgi, I. Pini, L. Ceraulo, and V. T. Liveri, *J. Mass Spectrom.,* 2011, 46, 925-932.

14 Y. Nozaki, and C. Tanford, *J. Bio. Chem.,* 1971, 246, 2211-2217.

15 W. C. Wimley, and S. H. White, *Nature Structure Biology,* 1996, 3, 842-848.

16 E. B. Leodidis, and T. A. Hatton, *J. Phys. Chem.,* 1990, 94, 6400-6411.

17 E. B. Leodidis, and T. A. Hatton, *J. Phys. Chem.,* 1990, 94, 6411-6420.

18 E. B. Leodidis, A. S. Bommarius, and T. A. Hatton, *J. Phys. Chem. ,* 1991, 95, 5943-5956.

19 E. B. Leodidis, and T. A. Hatton, *J. Phys. Chem.,* 1991, 95, 5957-5965.

20 P. Vollhardt, and N. Schore, *Organic Chemistry.* 6th edn. 1270 vols (New York: W. H. Freeman and Company, 2009).

21 Y. Fang, A. Bennett, and J. Liu, *Phys. Chem. Chem. Phys.,* 2011, 13, 1466-1478.

22 D. J. Donaldson, A. F. Tuck, and V. Vaida, *Phys. Chem. Chem. Phys.,* 2001, 3, 5270-5273.

23 D. Bongiorno, L. Ceraulo, G. Giorgi, S. Indelicato, M. Ferrugia, A. Ruggirello, and V. T. Liveri, *J. Mass Spectrom.,* 2011, 46, 195-201.

24 G. Longhi, S. L. Fornili, V. T. Liveri, S. Abbate, D. Rebeccani, L. Cerauloe, and F. Gangem, *Phys. Chem. Chem. Phys.,* 2010, 12, 4694-4703.

25 A. I. Bulavchenko, A. F. Batishchev, E. K. Batishcheva, and V. G. Torgov, *J. Phys. Chem. B,* 2002, 106, 6381-6389.

26 J. Faeder, and B. M. Ladanyi, *J. Phys. Chem. B,* 2000, 104, 1033-1046.

27 J. Chowdhary, and B. M. Ladanyi, *J. Phys. Chem. B,* 2009, 113, 15029-15039.

28 M. Sharon, L. L. Ilag, and C. V. Robinson, *J. Am. Chem. Soc.,* 2007, 129, 8740-8746.

29 G. Siuzdak, and B. Bothner, *Angew. Chem. Int. Ed.,* 1995, 34, 2053-2055.

30 F. Cacace, G. de Petris, E. Giglio, F. Punzo, and A. Troiani, *Chem. Eur. J.,* 2002, 8, 1925-1933.

31 D. Nohara, and M. Bitoh, *J. Mass Spectrom.,* 2000, 35, 1434-1437.

32 J. P. Wilcoxon, and P. P. Provencio, *J. Phys. Chem. B,* 1999, 103, 9809-9812.

Chapter 6

Guided-Ion-Beam and Trajectory Study on the Reaction of Deprotonated Cysteine with Singlet Molecular Oxygen ($a^1\Delta_g$)

6.1 Introduction

Electronically excited singlet molecular oxygen ($O_2[a^1\Delta_g]$) has characteristic chemistry in which molecules are oxygenated.[1-5] This sets it apart from ground-state triplet O_2 which, because of two unpaired parallel-spin electrons, does not react with most molecules unless activated by extra energy. $^1O_2$ can be generated in biological systems by energy transfer to $^3O_2$ from protein-bound or other chromophores on exposure to UV and visible light (*i.e.* photosensitization[6]), and by a range of enzymatic and nonenzymatic reactions.[7] Consequently, $^1O_2$ chemistry plays an important role in biological aging, diseases and cell death,[5, 7-9] and in photodynamic therapy where $^1O_2$ is used for cancer treatment.[10]

Due to its electron-rich side chain, cysteine (Cys) is one of the most vulnerable residues towards $^1O_2$ oxidation in proteins.[7, 9, 11] In fact, because it is prone to oxidation, Cys is rarely present as a free residue at surface-exposed parts of proteins.[12] Oxidation of Cys by $^1O_2$ often leads to disulfide formation such as a dimeric product cystine.[13] This reaction is biologically important because that controlled oxidation of cysteine residues and reduction of cystine residues constitute a redox switching mechanism that controls the structure and function of a number of key proteins.[9, 14] Most experiments devoted to the elucidation of the oxidation mechanism of Cys were carried out in solution,[15-21] using dye-sensitized "photo-oxidation" methods where $^1O_2$ was generated with UV or visible light in the presence of sensitizers. Photo-oxidation of Cys is strongly pH dependent. At high pH (= 8 – 11) the reaction is mediated by $^1O_2$, while at low pH (= 4 – 6) the reaction is mediated by radicals formed during photosensitization and the oxidation of the thiol group to disulfide is suppressed.[3] Oxidation involves formation of a persulfoxide intermediate though the mechanism remains obscure. Oxidation products include cysteine, oxyacids (RSO_2H and RSO_3H), and other species that remain to be elucidated.

To avoid the complexities arising from photo-oxidation experiments in solution (such as types of sensitizers, light, solvent compositions, and competition between $^1O_2$- and radical-mediated reactions) and simply the interpretation of Cys oxidation mechanism, the reaction of Cys with $^1O_2$ in the gas phase was chosen. One advantage of investigating biomolecules in the gas phase is that it allows one to observe single molecules separated from bulk solution environments. In this way, intrinsic reactivity of molecules can be distinguished from solvent effects. The reaction of protonated Cys ($CysH^+$) with $^1O_2$ in the gas phase has been reported by our group[22] using electrospray-ionization (ESI)[23, 24] mass spectrometry and guided-ion-beam scattering methods.[25] By combining the input of gas-phase experiments and theoretical simulations, the reaction mechanism and dynamics for $CysH^+ + {}^1O_2$ was unraveled. One interesting finding is that the electronic excitation energy of $^1O_2$ could be used to drive dissociation of an intermediate complex, the so-called dissociative excitation transfer.[26] In the present chapter, investigation was extended to the oxidation of deprotonated cysteine ($[Cys-H]^-$), attempting to examine the effects of protonation/deprotonation on oxidation of Cys. Our guided-ion-beam tandem mass spectrometer, coupled with an ESI source, was employed to examine the reaction. To understand and supplement gas-phase experiments, electronic structure calculations were used to construct reaction coordinate, and direct dynamics trajectory simulations were used to provide additional mechanistic insights.

6.2 Experimental and computational details

Experimental procedures The experiment in this study was carried out in our guided-ion-beam tandem mass spectrometer, which has been described in detail in previous chapters, along with the operation, calibration and data analysis procedures.[22, 27-31] Only a brief description is given here, emphasizing the key operating parameters used (in Table 6.1), and the modifications made for this experiment.

Table 6.1 Key operating parameters of the mass spectrometer in negative ion mode

ESI flow rate	0.05 ml•hr^{-1}
ESI bias voltage	-2,540 V
Capillary bias voltage	-93 V
Capillary temperature	150 – 160 °C
Skimmer bias voltage	-25 V
Pressure in hexapole ion guide	20 mTorr

The molar masses, purities, manufacturers and storage of chemicals and solvents used in the experiment are listed in appendix C. All chemicals were used without further purification.

Both mass filters were operated at 2.1 MHz with m/z range of 1 – 500, to achieve high ion transmission and mass resolution for the system. For conventional mass spectral measurements, the first quadrupole mass filter was operated in the rf-only mode as an ion guide, and mass scans were performed by the second quadrupole mass filter. The sample solution was prepared in methanol/water (1:1 volume ratio) containing 0.5 mM L-cysteine with 0.5 mM NaOH added to assist deprotonation. Ion beam intensities of $[\mathrm{Cys\text{-}H}]^-$ was typically 1×10^6 ion/sec, and constant within 10%. Their initial kinetic energies were 0.25 eV, and the energy spreads were ~0.3 eV which corresponds to an energy spread of ~0.06 eV in the center-of-mass frame for the collision of $[\mathrm{Cys\text{-}H}]^-$ with $^1O_2$. Reaction cross sections were calculated from the ratio of product and reactant ion intensities, calibrated $^1O_2$ pressure, and the calibrated effective length of the scattering cell, using a Beer's Law relationship.[32]

Generation of singlet oxygen by microwave discharge Singlet molecular oxygen ($a^1\Delta_g$) was generated by microwave discharge[33, 34] in a 1:1 mixture of O_2:Ar, and the $^1O_2$ yield was estimated using the specific energy deposition per molecule in the discharge.[35] The presence of Ar improved discharge stability and did not affect the measurements of $^1O_2$ reactions, because Ar is unreactive with $[Cys-H]^-$ except for CID which could be measured independently. The gas flow from the leak valve passed through a 6.3 mm o.d. × 3.0 mm i.d. alumina discharge tube surrounded by an Evenson resonant microwave cavity,[36] which was excited by a 2,450 MHz microwave power supply (Opthos Instruments, model MPG-4) , with the microwave power fed into the cavity no more than 18 W and the power reflected from the cavity less than 5 W. The variations of forward and reflected power were controlled to be within 10%, and the *specific energy deposition per molecule* (calculated from the forward and reflected microwave power, and the gas density) was determined to be 14 eV. The $^1O_2$ yield (~5%) was estimated using the *specific energy deposition per molecule* in the discharge.[35] The discharge tube was cooled to below 55 °C by air blown into the interior of the cavity. The exit end of the discharge tube was coated by mercuric oxide to remove O atoms generated from discharge. The discharge was about 40 cm from the scattering cell entrance, and the light from the discharge was trapped by a Wood's horn to avoid direct photolysis of ions or production of background ions by photo-desorption from the ion guide surface.

To provide reasonable intensities of product ions, the pressure of O_2/Ar in the scattering cell was maintained at 0.33 mTorr. The collision cross section ($\sigma_{collision}$) for $[Cys-H]^- + O_2$, taken as the greater of the ion-induced dipole capture cross section ($\sigma_{capture}$)[37] and the hard-sphere collision cross section ($\sigma_{hard-sphere}$, calculated from the orientation-averaged contact radii of [Cys-H]$^-$ and O_2), is 31 – 67 Å^2 in the E_{col} range of 0.1 eV – 1.0 eV. Accordingly, the probability of [Cys-H]$^-$ undergoing a single-collision within the scattering cell is < 17%, and that of double collisions is < 4%. The majority of [Cys-H]$^-$ ions (> 79%) passed through the scattering cell without any interaction with O_2 or Ar, hence keeping multiple ion-molecule collisions to an insignificant level.

As a check on reproducibility, the entire experiment was repeated several times and each time different E_{col} was cycled through. The data presented are averages of several independent data sets. The relative error of the cross section measurements was ~25%. To check the reactivity of [Cys-H]$^-$ toward $^3O_2$ and Ar, a control experiment was performed under the same conditions except that the microwave discharge was turned off. Recently, a chemical $^1O_2$ generator has been set up in our research lab, which uses the reaction of $H_2O_2 + Cl_2 + 2KOH \rightarrow O_2(a^1\Delta_g)/O_2(X^3\Sigma_g) + 2KCl + 2H_2O$ to generate $^1O_2$ without O and O_3 contaminants.[22, 30, 38] The experiment was repeated relying on this chemical $^1O_2$ generator, and the $^1O_2$ concentration was determined by the emission of O_2 ($a^1\Delta_g \rightarrow X^3\Sigma_g^-$, $\nu = 0 - 0$) at 1,270 nm[39] using a cooled InGaAs photodetector.[30] A reasonably good agreement was achieved between experiments using microwave discharge and chemical $^1O_2$ generation schemes, respectively.

Computational methods To aid in reaction coordinate interpretation, density functional theory (DFT) electronic structure calculations were performed at the B3LYP level of theory with various basis sets including 6-31G, 6-31G(d), 6-31+G(d) and 6-311++G(d,p), using Gaussian 09.[40] All geometries were optimized by calculating force constants at every step. Vibrational frequencies and zero-point energies (ZPE) were scaled by a factor of 0.955 and 0.981,[41] respectively. All the transition states (TSs) found were verified as first-order saddle points by frequency calculations, and the vibrational mode with the imaginary frequency corresponds to the reaction pathway. Relaxed potential energy surface scans were performed to look for possible barriers during reactant approach or product separation.

Quasi-classical, direct dynamics trajectory simulations were conducted to identify important steps in the reaction coordinate for $[\text{Cys-H}]^{-}$ + $^{1}O_2$. The chemical dynamics program VENUS99 of Hase *et al.*[42] was used to set up trajectory initial conditions, and the Hessian-based method of Bakken *et al.*[43] implemented in Gaussian was used to propagate each trajectory, with Hessians recalculated every five steps. Because millions of gradients and Hessian evaluations were required, the level of theory used for trajectories was necessarily modest. On the basis of the overall level of agreement with experimental and/or high level benchmark results and computational speed, B3LYP/4-31G(d) level of theory was chosen for calculating trajectories. Trajectory integrations were performed with a step size of 0.25 amu$^{1/2}$Bohr (corresponding to a step size of ~0.5 fsec in trajectory time), which conserved total energy to better than 10^{-4} Hartree. The SCF = XQC option was adopted during trajectory integration so that a quadratically convergent Hartree-Fock (QC-SCF) method[40, 44] was used in case the usual, but much faster, first-order SCF method failed to converge within the allotted number of cycles.

The purpose of the trajectory simulations was to probe the gross features of the collisions between $[\text{Cys-H}]^{-}$ and $^{1}O_2$. Particularly, simulations were used to help discover the reaction mechanism, and locate key transition states for reactions when the standard TS-searching methods failed. Thus all 100 trajectories were calculated at an impact parameter b of 0.1 Å, rather than sampling the b distribution. E_{col} was set at 0.2 eV for simulations. The initial conditions of the reactants were chosen to mimic my experimental conditions. Because [Cys-H]$^-$ ions were thermalized in the experiment, their initial vibrational and rotational energies in trajectories were sampled from Boltzmann distributions at 300 K. Similarly, $^1O_2$ in the experiment was close to room temperature, so 300 K was used for both rotational and vibrational temperature for $^1O_2$. The quasi-classical initial vibrational state was simulated by giving each reactant atom displacement from equilibrium and momentum appropriate to the initial rovibrational state, with random phases for different modes. Both [Cys-H]$^-$ and $^1O_2$ have ZPE in all vibrational modes. Randomly oriented [Cys-H]$^-$ and $^1O_2$ were given relative velocities corresponding to the simulated E_{col}. All trajectories started with an initial center-of-mass reactant separation of 7.0 Å, and were terminated either when the distance between products exceeded 7.2 Å, or after 3000 steps. The attractive energy between reactants at the separation of 7.0 Å is no more than 11 meV, most of which was determined to come from basis set superposition error (BSSE).[45] Trajectories were calculated on an Intel core 2 quad (3.0 GHz) and core i7 6-core (3.2 GHz)-based 64 bit Linux computational cluster, and each trajectory took 150 – 250 CPU hours. gOpenMol[46] was used for trajectory visualization. Analysis of individual trajectories and statistical analysis of the trajectory ensemble were done with programs written for this purpose.

6.3 Results and discussion

6.3.1 Gas-phase structures of [Cys-H]$^-$

One issue for interpretation of [Cys-H]$^-$ chemistry is that Cys has two deprotonation sites leading to two different anionic structures, *i.e.*, the carboxylate anion $HSCH_2CH(NH_2)CO_2^-$ due to the deprotonation of the backbone carboxylic acid group, and the thiolate anion $^-SCH_2CH(NH_2)CO_2H$ due to the deprotonation of the thiol group in the side chain. Both $HSCH_2CH(NH_2)CO_2^-$ and $^-SCH_2CH(NH_2)CO_2H$ have various conformations resulting from their structure flexibility. A grid search method[45] was used to find local minimums in their conformational landscape. Each of the torsional angles of the amino acid was rotated systematically through 360° at 60° increments to generate possible conformations of $HSCH_2CH(NH_2)CO_2^-$ and $^-SCH_2CH(NH_2)CO_2H$, the so-called rotamers. Every conformation so generated was subjected to geometry optimization at B3LYP/6-31+G(d) to derive associated local minimum conformation. Many of the initial conformations were optimized to the same local minimum conformations. These conformations were then optimized at B3LYP/6-311++G(d, p). Their structures and relative energies with respect to $^-SCH_2CH(NH_2)CO_2H\_1$, the lowest energy conformation of $[Cys\text{-}H]^-$, are summarized in Figure 6.1.

The conformations in the top portion of Figure 6.1 belong to the $^-SCH_2CH(NH_2)CO_2H$ structure, differing by the *cis-/trans-*configuration of -COOH, the orientation of the -COOH group with respect to the $-NH_2$ group and that of the thiolate group to the backbone. All conformations are stabilized by intramolecular hydrogen bonds except $^-SCH_2CH(NH_2)CO_2H\_11$ and 13. Particularly, strong hydrogen bonds via proton-sharing between the carboxylic acid and thiolate groups occur in the first three low-lying conformers, with the distance of S···HOOC being 1.94 – 1.98 Å. Shared proton binding motifs also occur to some extent in the fourth and fifth conformers, between the carboxylic acid and amino groups with a distance of 1.80 – 1.84 Å from the N atom to the H atom of -COOH. The energies of the first five $^-SCH_2CH(NH_2)CO_2H$ conformers differ by a maximum of 0.32 eV, and the remaining conformers lie 0.53 – 0.86 eV higher in energy with respect to $^-SCH_2CH(NH_2)CO_2H\_1$.

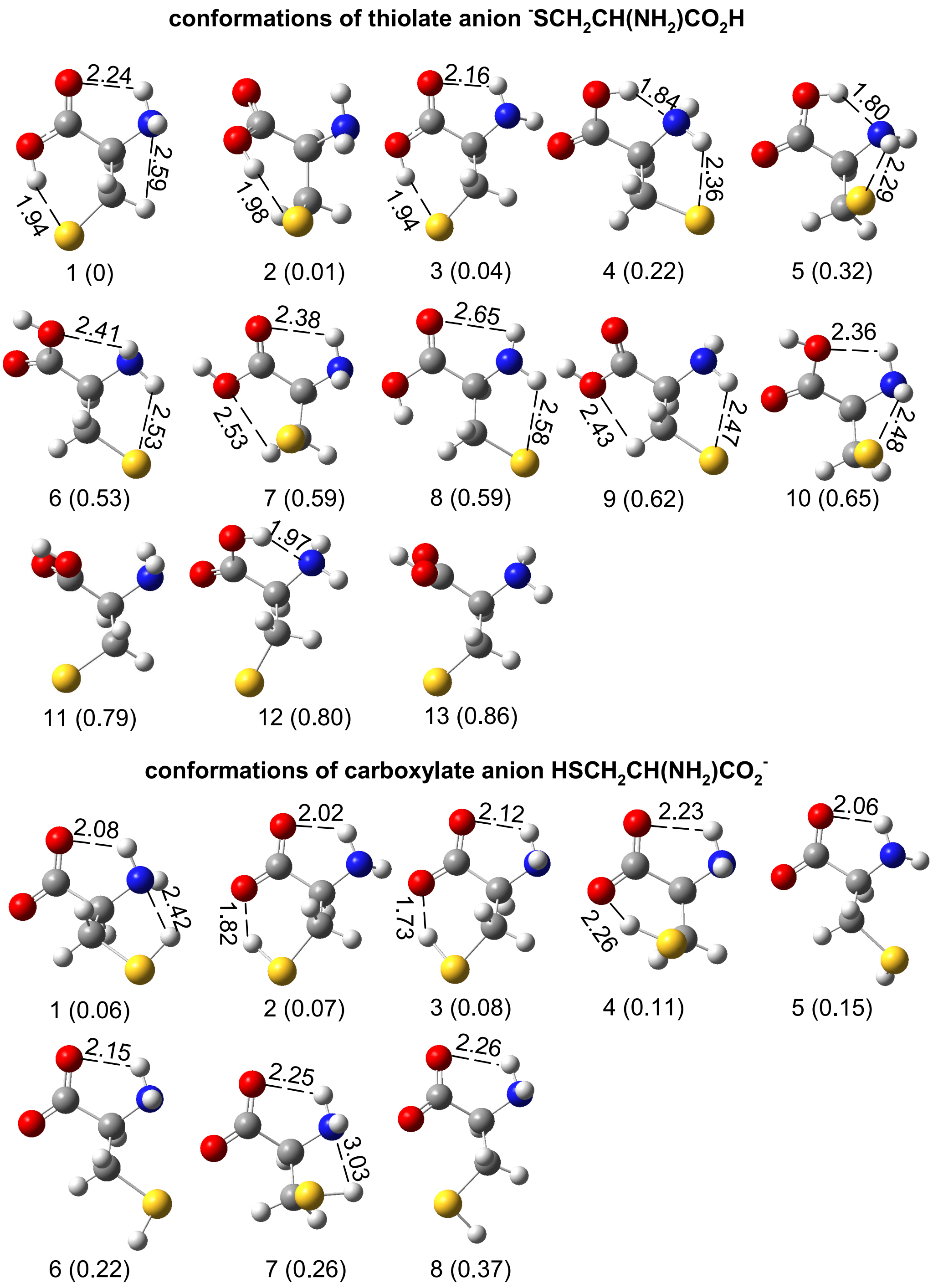

conformations of thiolate anion $^{-}SCH_2CH(NH_2)CO_2H$

conformations of carboxylate anion $HSCH_2CH(NH_2)CO_2^{-}$

Figure 6.1 Low-lying conformations of deprotonated Cys calculated at B3LYP/6-311++G(d,p), including thiolate and carboxylate anionic structures. Their relative energies at 0 K (eV, including ZPE) are indicated below each structure.

$HSCH_2CH(NH_2)CO_2^-$ conformers are found to be 0.06 – 0.37 eV higher in energy than the lowest energy thiolate conformer. Each of these conformers features an intramolecular hydrogen bond between one of the H atoms of the N-terminus and the deprotonated C-terminus with a HNH···COO distance of 2.02 – 2.26 Å. $HSCH_2CH(NH_2)CO_2^-$_1 and 7 each has a second hydrogen bond of $SH\cdots NH_2$ with a distance of 2.42 – 3.03 Å, while $HSCH_2CH(NH_2)CO_2^-$_2, 3 and 4 each has a second hydrogen bond of SH···OOC with a distance of 1.73 – 2.26 Å. The stable conformations found for the thiolate and carboxylate structures are consistent with previous reports.[47-50]

The p*K*a of the carboxylic acid group (2.0) is 6.2 units smaller than that of the thiol group (8.2) in Cys,[51] indicating that $[Cys-H]^-$ should be a carboxylate but not a thiolate in solution. However, disputes arise regarding the structure of $[Cys-H]^-$ in the gas phase. My DFT calculation results at B3LYP/6-311++G(d,p), as well as other calculations performed at B3LYP/6-311++G(d,p)//B3LYP/6-31+G(d),[49] B3LYP/aug-cc-pVDZ, and G3B3 levels of theory,[50] reveal that the thiol group of Cys is slightly more acidic than the carboxylic acid group, albeit by a very small margin. Experimentally, Woo *et al.* claimed that ESI of Cys in 3:1 (v:v) methanol/water solution produced a thiolate in the gas phase according to photoelectron spectroscopy measurements.[48] Tian *et al.* found that the preferred deprotonation site for gaseous Cys is the thiol side chain rather than the backbone carboxylic acid based on H/D exchange reactions of $[Cys-H]^-$ with various deuterated alcohols in the gas phase.[50]

On the other hand, Oomens *et al.*[52] reported gas-phase infrared multiple photon dissociation (IRMPD) spectrum of $[Cys-H]^-$ which was generated by ESI of a mixture of Cys and NaOH in methanol/water. In contrast to PES and H/D exchange studies, the conformation-specific IRMPD spectrum identified a carboxylate structure only for gaseous

$[Cys\text{-}H]^-$. It therefore seems that the structures of $[Cys\text{-}H]^-$ present in the gas phase depend on experimental conditions,[52] given for instance a similar finding was reported for the carboxylate *vs.* phenoxide structures of deprotonated Tyr in the gas phase.[38, 52-54] In my CID experiment of $[Cys\text{-}H]^-$ with Ar and $^3O_2$(*vide infra*), overwhelmingly dominant product ions are those of *m/z* 33, corresponding to the formation of HS^- anions. HS^- is a characteristic fragment of the carboxylate structure, as reported in IRMPD.[52] This evidence leads us to conclude that our ESI source produced dominantly carboxylate anions for the reaction with $^1O_2$. In the following calculations and discussion, the most stable $HSCH_2CH(NH_2)CO_2^-$ conformation in Figure 6.1 was used as the reactant ion structure. It is certainly possible that interconversion between different rotamers of $HSCH_2CH(NH_2)CO_2^-$ may occur during collisions. However, it seems less likely that different rotamers would significantly alter reaction coordinate, as confirmed by the trajectory simulations of $HSCH_2CH(NH_2)CO_2^-$ + $^1O_2$(*vide infra*), as well as $CysH^+$ + $^1O_2$,[22] $TyrH^+$ + $^1O_2$,[27] $[Tyr\text{-}H]^-$ + $^1O_2$,[38] and $MetH^+$ + $^1O_2$.[30]

6.3.2 Reaction cross sections of $HSCH_2CH(NH_2)CO_2^-$ + $^1O_2$

For the reaction of $HSCH_2CH(NH_2)CO_2^-$ (*m/z* 120) + $^1O_2$, product ions were observed at *m/z* 74, 118 and 135 over the collision energy range of 0.1 – 1.0 eV. At higher collision energies, product ions were also observed at *m/z* 33, 76, 87, and 102, of which *m/z* 33 is largely dominant. The latter four product ions correspond to the formation of HS^-,[52] and elimination of CO_2,[55], HS, and H_2O,[56] respectively, from CID of $HSCH_2CH(NH_2)CO_2^-$. They were also observed upon collisions of $HSCH_2CH(NH_2)CO_2^-$ with $^3O_2$ and Ar (*i.e.*, when the O_2 microwave discharge was off), and therefore could be excluded from $^1O_2$-specific reactions. Product ions of *m/z* 74, 118 and 135, on the other hand, were not observed with $^3O_2$ and Ar, and cannot be attributed to CID products.

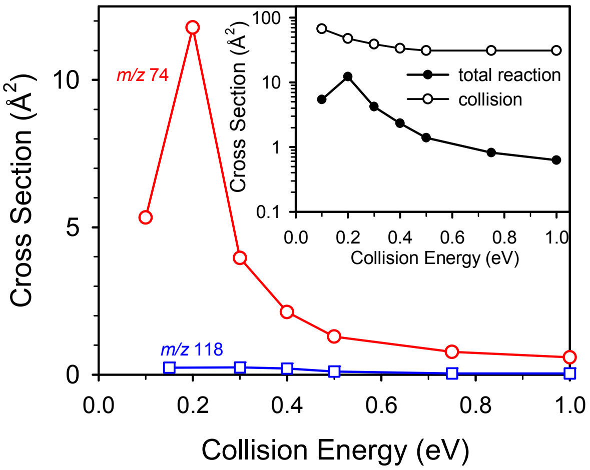

Figure 6.2 Product cross sections for the reaction of $HSCH_2CH(NH_2)CO_2^-$ with $^1O_2$, as a function of center-of-mass collision energy. The estimated collision cross section and the total reaction cross sections are shown in the inset.

Product cross sections of *m/z* 74 and 118 are shown in Figure 6.2, as a function of the center-of-mass E_{col}. Note that the cross section for product ions of *m/z* 135 is too small to allow for a meaningful measurement of its E_{col} dependence. Also shown in the insert of Figure 6.2 are the experimental total reaction cross section (σ_{total} = sum of individual cross sections) and the estimated collision cross section $\sigma_{collision}$. It is to be noted that the absolute uncertainty in the cross section measurements, mostly arising from uncertainty in the $^1O_2$ concentration, could be large. This source of uncertainty, however, does not affect the relative cross sections, *i.e.*, the E_{col} dependence of cross sections, which is the primary interest in the study. In the present ion-molecule scattering experiments, an uncertainty of 25% was quoted for relative cross sections.[22, 27, 30, 38] Both product channels have significant cross sections only at the lowest energies, and are strongly inhibited by E_{col}. The overall reaction efficiency, estimated as $\sigma_{total}/\sigma_{collision}$, is ~25% at low collision energies, dropping to 7% at E_{col} = 0.4 eV and 4% at E_{col} = 0.5eV, and becoming negligible at E_{col} > 0.75 eV. On the other hand, the collision energy dependence of reaction cross sections indicates that both reactions could proceed without significant energy barriers in excess of reactants.

Note that the electron detachment energy for $HSCH_2CH(NH_2)CO_2^-$ is calculated to be 2.64 eV at B3LYP/6-31+G(d), which is beyond the E_{col} range of 0.1 to 1.0 eV used in the present experiment. Consequently, the detachment of the excess electron from $HSCH_2CH(NH_2)CO_2^-$ could be disregarded during the collision with target gases. In addition, assuming the excitation energy (0.98 eV)[39] and electron affinity (0.45 eV)[57] of $^1O_2$ can all be used to drive reaction, the electron transfer between $HSCH_2CH(NH_2)CO_2^-$ and $^1O_2$ is endothermic by 1.21 eV, and thus cannot occur in our E_{col} range, either.

6.3.3 Reaction mechanism

A. Product ion of *m/z* 74

Complex-mediated dissociative excitation transfer The product ion channel of *m/z* 74 has the largest cross sections over the entire E_{col} range. There are two possible reaction pathways leading to the dissociation of an intermediate complex to a product ion of *m/z* 74, as outlined below:

$$HSCH_2CH(NH_2)CO_2^- + {}^1O_2 \rightarrow NH_2CH_2CO_2^- + CH_2SO_2 \qquad \Delta H_{rxn} = 0.7\ \text{eV} \qquad (1)$$

$$[NH_2CHCO_2H]^- + CH_2SO_2 \qquad \Delta H_{rxn} = 2.1\ \text{eV} \qquad (2)$$

However, both reaction pathways could be discounted based on their reaction heat of formation (ΔH_{rxn}) calculated at B3LYP/6-31+G(d). If *m/z* of 74 was produced from unimolecular dissociation of $HSCH_2CH(NH_2)CO_2^-$, the lowest dissociation energy pathway corresponds to

$$HSCH_2CH(NH_2)CO_2^- \rightarrow NH_2CH_2CO_2^- + CH_2S \qquad \Delta H_{rxn} = 1.2\ \text{eV} \qquad (3)$$

This dissociation energy was calculated at B3LYP/aug-cc-pV5Z. The reaction involves intramolecular transfer of a H atom from the thiol group to C^α, prior to (or concurring with)

C^{α}-C^{β} bond cleavage of $HSC^{\beta}H_2C^{\alpha}H(NH_2)CO_2^-$. Obviously, reaction (3) could not occur at E_{col} well below the dissociation threshold (instead the cross section would rise from zero at an appearance energy near the dissociation threshold and increase with E_{col}), unless this dissociation is prompted by the excitation energy of $^1O_2$.

Viggiano *et al.* reported several examples in which the electronic excitation energy of $^1O_2$ was utilized for driving endothermic reactions, such as electron transfer between $^1O_2$ and O_2^-, SO_2^-, and HO_2^-,[58, 59] and dissociation of $OH^-(H_2O)_{1,2}$ by the excitation energy of $^1O_2$ — the so-called dissociative excitation transfer.[26] Recently, my colleague and I reported the gas-phase reaction of $CysH^+$ with $^1O_2$ and proposed a mechanism based on the similar idea.[22] The reaction of $CysH^+$ + $^1O_2$ proceeds via C^{α}-C^{β} bond rupture of a hydroperoxide intermediate $CysOOH^+$ accompanied by intramolecular H atom transfer. All of the $^1O_2$ excitation energy was used to drive the dissociation of $CysOOH^+$, yielding $H_2NCHCO_2H^+$, CH_3SH, and $^3O_2$. Note that, to realize excitation energy transfer in these systems, a strong reactant interaction must be warranted to affect the electronic property of $^1O_2$ and hence break the spin conservation propensity rule.

If a similar scenario occurs for $HSCH_2CH(NH_2)CO_2^-$ + $^1O_2$, the formation of $NH_2CH_2CO_2^-$ would become energetically feasible at low E_{col}. However, a related question arises to the nature of energy transfer from $^1O_2$. Two mechanisms may be imaged for dissociation of $HSCH_2CH(NH_2)CO_2^-$ to $H_2NCH_2CO_2^-$ + CH_2S. The reaction could proceed in a direct sequential mechanism as invoked in conventional CID, *i.e.*, an activating collision where the excitation energy of $^1O_2$ and a fraction of E_{col} are converted to the internal energy (E_{int}) of $HSCH_2CH(NH_2)CO_2^-$, followed by unimolecular decomposition of excited $HSCH_2CH(NH_2)CO_2^-$ after O_2 has recoiled. However, such direct sequential mechanism could be ruled out for two reasons. First, a direct collision would likely show E_{col}

enhancement rather than inhibition for an endoergic dissociative reaction, since kinetic energy to E_{int} conversion is helpful for overcoming the reaction threshold as observed in typical CID reactions.[60, 61] Secondly, based on DFT calculations the triplet excited state of $HSCH_2CH(NH_2)CO_2^-$ would pre-dissociate to $[H_2NCHCH_2 + SH + CO_2]^-$, rendering the energy transfer via intersystem crossing of $HSCH_2CH(NH_2)CO_2^- + {}^1O_2 \rightarrow {}^3HSCH_2CH(NH_2)CO_2^{-*} + {}^3O_2$ impossible.

An alternative reaction mechanism relies on the formation of a complex between $HSCH_2CH(NH_2)CO_2^-$ and $^1O_2$, and the electronic energy of $^1O_2$ converts into whatever form of E_{int} needed for dissociating the complex. The dissociation must be concerted, *i.e.*, O_2 must remain in close proximity to $HSCH_2CH(NH_2)CO_2^-$ as $HSCH_2CH(NH_2)CO_2^-$ dissociates; in the meantime, strong spin-orbital coupling within the complex could "catalyze" access to the triplet channel with no activation energy in excess of the asymptotic energy for the products. A similar concerted mechanism has been reported for spin-forbidden reactions of $NO_2^+ (^1\Sigma_g^+) + Xe \rightarrow NO^+(^1\Sigma_g) + O(^3P) + Xe$,[60] and $CysH^+ + {}^1O_2 \rightarrow H_3NCHCO_2H^+ + CH_3SH + {}^3O_2$.[22] A complex-mediated mechanism is reasonable for a system like $HSCH_2CH(NH_2)CO_2^- + {}^1O_2$, since the number of degrees of freedom is large for efficient $E_{ele} \rightarrow E_{int}$ transfer.

A complex-mediated mechanism is also consistent with the observed E_{col} dependence of reaction cross section. Production of $H_2NCH_2CO_2^- + CH_2S$ requires intramolecular H atom transfer – a rearrangement needs to be mediated by a long-lived complex. The efficiency of complex formation decreases with increasing E_{col}, which explains the decreasing of reaction cross section at high E_{col}.

Reaction coordinate Potential energy surface (PES) associated with possible low energy reaction pathways for $HSCH_2CH(NH_2)CO_2^- + {}^1O_2$ is presented in Figure 6.3. The reactants are shown near the center at zero energy, and the complex-mediated dissociative excitation transfer between $^1O_2$ and $HSCH_2CH(NH_2)CO_2^-$ is shown in the right portion of the figure. Energetics are derived from a combination of B3LYP/6-31+G(d) and B3LYP/aug-cc-pV5Z results and the experimental value of $^1O_2$ excitation energy. Four weakly bound complex (RC1 and RC2, and PC1 and PC2) and two covalently bound complexes (a persulfoxide and a hydroperoxide) were identified. The transition states (TSs) connecting the complexes to each other and to the reactants and products are indicated in the figure. Complexes RC1 and RC2 can be characterized as reactant-like complexes, formed by electrostatic interaction and ionic hydrogen bonds. Complex RC1 has the O_2 moiety sandwiched between the thiol and amino groups of $HSCH_2CH(NH_2)CO_2^-$, with distances of 2.15 and 2.35 Å for SH···O-O and O-O···HNH, respectively. RC2 is a hydrogen-bonded complex, with both $-C^{\alpha}H$ and $-NH_2$ hydrogen bonded to the O_2 moiety with H···O distances of 1.67 – 1.98 Å. The binding energies of RC1 and RC2 are 0.75 eV and 0.62 eV, respectively, with respect to the reactants. Because no rearrangement is needed to form reactant-like complexes from the reactants, it is less likely to have significant barriers inhibiting the formation of these two complexes. This was verified by direct dynamics trajectory simulations to be discussed below. Because of a lack of directional covalent bonds between $HSCH_2CH(NH_2)CO_2^-$ and O_2 moieties, complexes RC1 and RC2 do not have a well-defined geometry at the energies available in the present experiment, and are rather floppy with a large amplitude of intermolecular motion. The point is that they allow repeated encounters between reactants, increasing reaction probability for collisions not initially in the correct geometry and enhancing the reaction cross section.

RC1 may eventually lead to the formation of a persulfoxide through TS1. Persulfoxide is a covalently bound intermediate, with a binding energy of 1.17 eV relative to the reactants. In the persulfoxide, a H atom is transferred from the thiol group to the amino group. Based on relaxed PES scan, persulfoxide may facilely undergo intramolecular H atom transfer from -NH_3 to the peroxide group and converge to a more stable hydroperoxide intermediate. I propose that the persulfoxide and/or hydroperoxide may undergo three-body dissociation to $H_2NCH_2CO_2^-$, CH_2S, and $^3O_2$. Intramolecular H atom transfer occurs simultaneously with the dissociation of the persulfoxide or hydroperoxide, transferring a H atom from -NH_3 or -SOOH to the C^α atom. Assuming all of the $^1O_2$ excitation energy is contributed to the dissociation of the persulfoxide and/or hydroperoxide, the calculated ΔH_{rx} is ~0.2 eV, as indicated by the heavy green line in Figure 6.3.

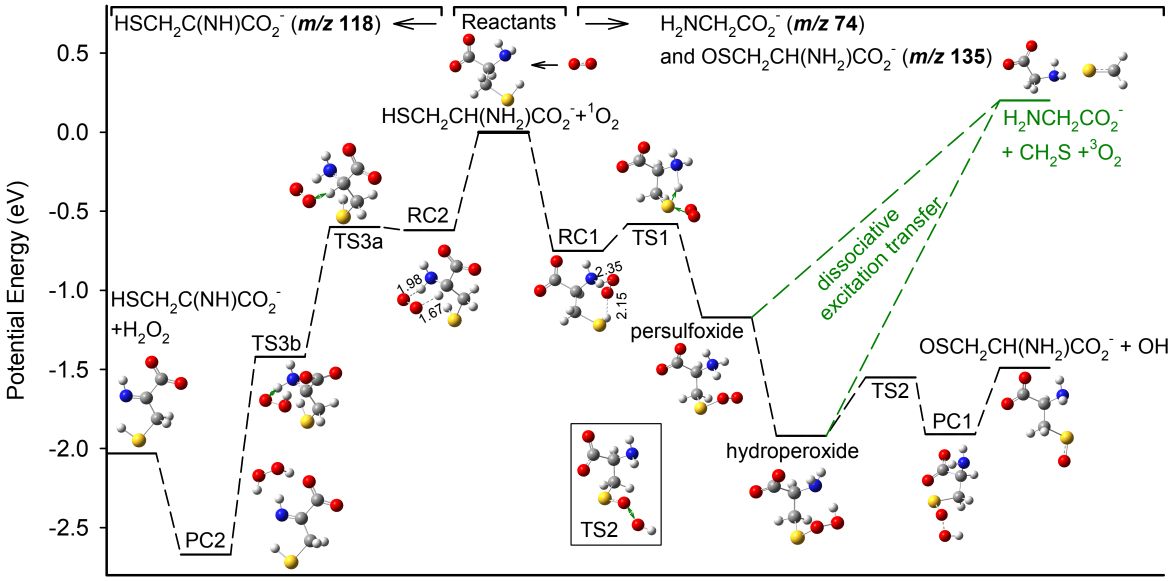

Figure 6.3 Schematic reaction coordinate for $HSCH_2CH(NH_2)CO_2^-$ + $^1O_2$. Energies of complexes, TSs, and products, relative to reactants, are derived from a combination of B3LYP/6-31+G(d) and B3LYP/aug-cc-pV5Z results, including ZPE. The bond distances are shown in angstroms. For TSs, vibrational modes corresponding to the imaginary frequencies are indicated by displacement vectors.

The calculated ΔH_{rx} is consistent with my experimental observation. As shown in Figure 6.2, the cross section of $H_2NCH_2CO_2^-$ generally increases with decreasing E_{col}, but dips at the lowest E_{col}. A dip of this sort is typical for channels that are endoergic, but with endoergicity comparable to the E_{col} broadening resulting from the distributions of ion beam and target molecule velocities in the experiment. It is also worth noting that the reaction endoergicity of 0.2 eV was calculated based on the most stable carboxylate conformer of deprotonated Cys, *i.e.* $HSCH_2CH(NH_2)CO_2^-$_1 in Figure 6.1. Other conformers such as $HSCH_2CH(NH_2)CO_2^-$_2, 3 and 4 with energy within ~0.1 eV of $HSCH_2CH(NH_2)CO_2^-$_1 may form in our ESI source and participate in the reaction. Consequently, at the lowest nominal E_{col} (*i.e.* 0.1 eV) a large fraction of collisions have energy more than the threshold energy, and can react. As a result, the product cross section generally increases with decreasing E_{col}, presenting an "exothermic" reaction pattern. Similar E_{col} dependence has been reported for an endothermic reaction of $H_2CO^+ + OCS \rightarrow OCSH^+ + HCO$, with a threshold energy between 0.04 to 0.22 eV.[62]

B. Product ions of *m/z* 135 and 118

Product ion of *m/z* 135 corresponds to the elimination of a OH radical from a reaction intermediate complex. DFT calculations suggest a possible pathway for OH elimination, and its energetics is given as

$$HSCH_2CH(NH_2)CO_2^- + {}^1O_2 \rightarrow OSCH_2CH(NH_2)CO_2^- + OH \quad \Delta H_{rxn} = -1.49 \text{ eV} \qquad (4)$$

This reaction follows the same route as that for the formation of $H_2NCH_2CO_2^-$, *i.e.*, $HSCH_2CH(NH_2)CO_2^- + {}^1O_2 \rightarrow RC1 \rightarrow TS1 \rightarrow$ persulfoxide $\rightarrow$ hydroperoxide, except for the last step at which the hydroperoxide dissociates into a product-like complex PC1 by breaking the peroxide bond. A transition state TS2 has been located between the hydroperoxide and PC1 with an energy barrier of 0.37 eV above the hydroperoxide (see Figure 6.3). PC1 is bound by 0.42 eV with respect to the dissociation products, and no reverse barrier separates this product-like complex from $OSCH_2CH(NH_2)CO_2^- + OH$. Based on the reaction coordinate, $H_2NCH_2CO_2^-$ and $OSCH_2CH(NH_2)CO_2^-$ are simply two competing channels originating from the decay of the same set of intermediate complexes, *i.e.* persulfoxide and/or hydroperoxide. However, despite the fact that the product channel of $OSCH_2CH(NH_2)CO_2^-$ is considerably more energetically favorable than that of $H_2NCH_2CO_2^-$, this channel is insignificant over all collision energies. This discrepancy is not surprising, considering that my calculated PES follows an adiabatic process and is restricted to the singlet state. In reality, two electronic states contribute to the PES, *i.e.*, the system goes from a singlet to a triplet state as the products $H_2NCH_2CO_2^- + CH_2S + {}^3O_2$ separate after dissociative excitation transfer.

Product ion of *m/z* 118 is another interesting channel, corresponding to the abstraction of two H atoms from $HSCH_2CH(NH_2)CO_2^-$ by ${}^1O_2$ to form hydrogen peroxide, and is therefore referred to as **H2T** reaction. Based on H2T reactions of other amino acids,[27] there might exist concerted H2T mechanisms that are difficult to predict using chemical intuitions only. I thus chose to treat the system using quasi-classical, direct dynamics trajectory simulations, where the motion of molecules is followed, allowing the molecules to show us what the preferred reaction pathways are. Trajectory results are discussed in the last section. By following the variations of chemical bonds and potential energies during trajectories, I was able to identify a lower energy pathway for H2T which corresponds to

$$HSCH_2CH(NH_2)CO_2^- + {}^1O_2 \rightarrow HSCH_2C(NH)CO_2^- + H_2O_2 \qquad \Delta H_{rxn} = -2.03\ \text{eV} \qquad (5)$$

As indicated in the left portion of Figure 6.3, complex RC2 goes through two consecutive TSs (TS3a and TS3b). At TS3a, which corresponds to a barrier slightly above RC2, the H atom of $-C^{\alpha}H$ is transferred to the O_2 moiety. The path from TS3a leads to TS3b, in which the second H atom is transferred from $-NH_2$ to the other end of the O_2 moiety, leading to a product-like complex PC2 of which two O-H bonds of hydrogen peroxide are fully formed. The calculated reaction coordinate reflects a mainly sequential mechanism, and the ratelimiting step is clearly the transfer of the first H atom as the path from TS3a to TS3b is downhill. But this mechanism has some character of a concerted reaction since there is no complex located between two TSs, which has been verified by my trajectories.

6.3.4 Direct dynamics trajectory simulations

A total of 100 trajectories were completed at E_{col} = 0.2 eV and b = 0.1 Å using the B3LYP/4-31G(d) level of theory. Nearly 10% of collisions either form a persulfoxide and/or hydroperoxide, or eliminate H_2O_2. Remaining trajectories belong to nonreactive collisions, *i.e.*, fly by without forming long-lasting complexes within the simulation time (~3 ps).

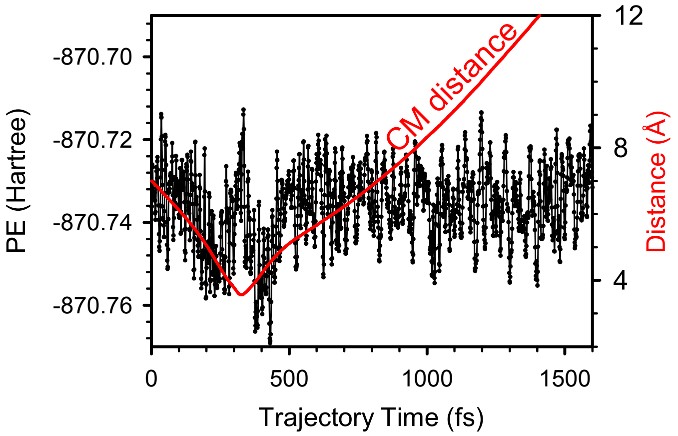

Figure 6.4 A representative plot of nonreactive trajectories at E_{col} = 0.2 eV, showing the variations of potential energy and center-of-mass distance between $HSCH_2CH(NH_2)CO_2^-$ and $^1O_2$ moieties during the trajectory.

Figures 6.4, 6.5 and 6.6 demonstrate trajectories representative of nonreactive and reactive collisions of $HSCH_2CH(NH_2)CO_2^-$ + $^1O_2$, respectively. The plots show the changes of CM distances and potential energy (PE) along the trajectory simulation time. The CM distance is the distance between the centers of mass of the collision partners. Figure 6.4 shows a direct, nonreactive scattering, with only one turning point in the relative motion of the reactant centers of mass, *i.e.*, there is no sign of mediation by a complex in this collision. The time scale of the collision is somewhat arbitrary, but three numbers are relevant. The time between the start of trajectory and the onset of strong interaction, which depends on reactant orientation, is around 200 fs. The time for reactant approach within 5 Å of CM distance is around 300 fs. More importantly, the time period during which $HSCH_2CH(NH_2)CO_2^-$ and $^1O_2$ interact strongly is around 100 fs, as shown by a potential energy spike beginning at t ≈ 300 fs. During the trajectory, potential energy fluctuates due to the vibrational motions of reactants.

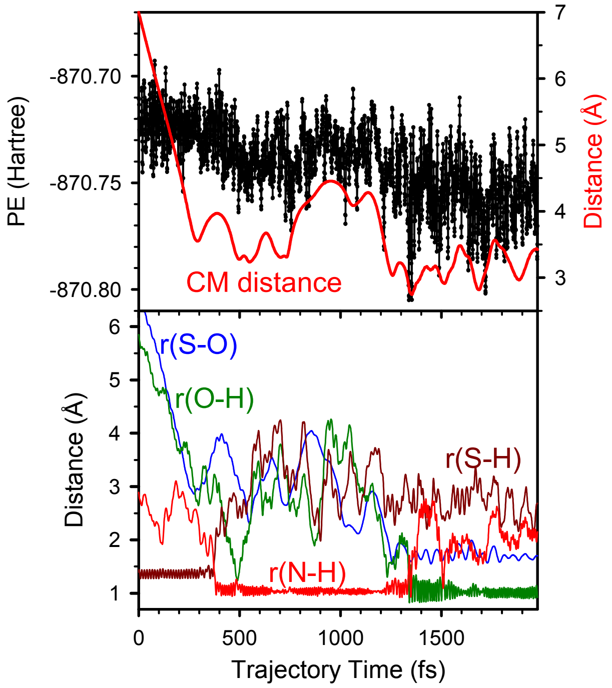

Figure 6.5 A representative plot of complex-forming trajectories at E_{col} = 0.2 eV, (top) the variations of potential energy and center-of-mass distance between $HSCH_2CH(NH_2)CO_2^-$ and $^1O_2$ moieties, and (bottom) the variations of various bond lengths during the trajectory.

Figure 6.5 illustrates a complex-forming trajectory, with the similar reactant approach time as that for the nonreactive trajectory shown in Figure 6.4. The top frame of Figure 6.5 shows the changes of CM distance and potential energy, and the bottom frame shows the r(S-O), r(O-H), r(S-H) and r(N-H) bond lengths forming or breaking in the reaction. The high frequency oscillations of r(S-O), r(O-H), r(S-H) and r(N-H) reflect the vibrations of the reactants or products. This trajectory initially forms a loosely bound complex as shown by the decrease of the CM distance to less than 4.5 Å staring at 215 fs. This is followed by the formation of a persulfoxide via transfer of a H atom from the S atom to the N atom, as illustrated by the abrupt increase of r(S-H) and decrease of r(N-H) at 350 fs. The large-amplitude, low frequency oscillations of r(S-O) reflects the interconversion between the weakly bound complex RC and covalently bound persulfoxide. At 1,350 fs, the persulfoxide converges to a hydroperoxide as the H atom travels again from the N atom to the peroxide group, as indicated by the simultaneous breaking of r(N-H) and forming of r(O-H) at that time point. The trajectory follows the reaction coordinate described in the right portion of Figure 6.3 until the formation of persulfoxide and hydroperoxide. In agreement with the PES in Figure 6.3, no obvious potential barrier was observed during the formation of these complexes.

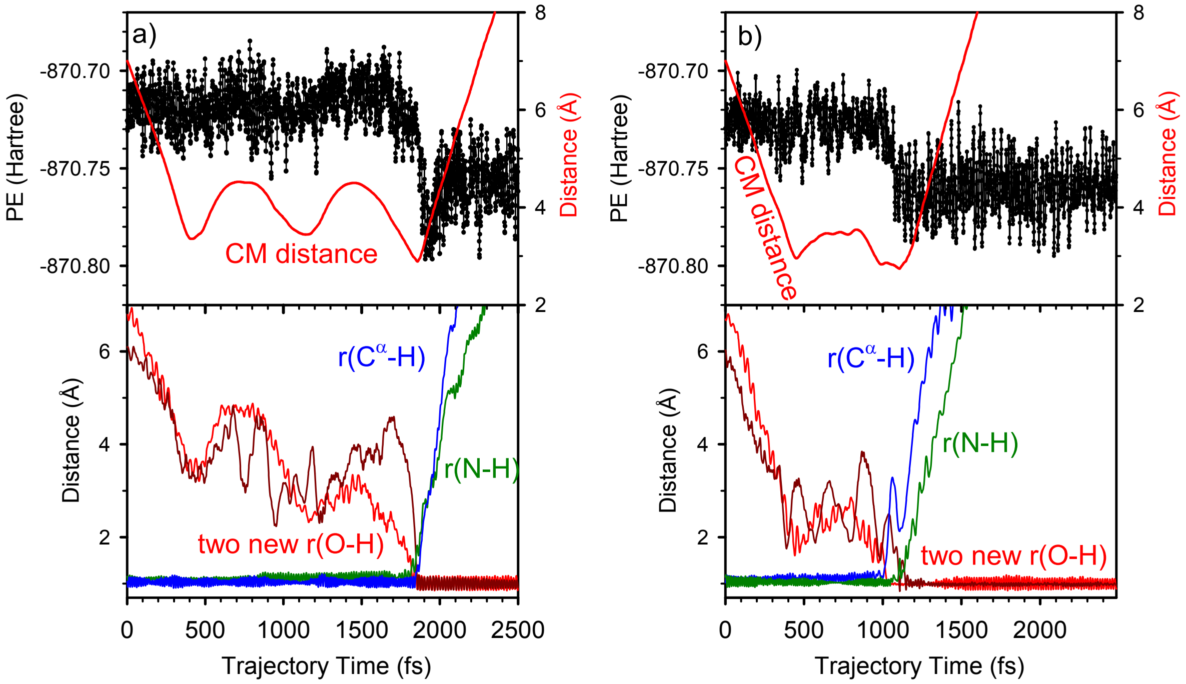

Figure 6.6 Representative plots of H2T trajectories at E_{col} = 0.2 eV, (top) the variations of potential energy and center-of-mass distance between reactants or products, and (bottom) the variations of various bond lengths during the trajectory. Fig. a) shows a concerted mechanism for abstraction of two H atoms, while b) shows a sequential mechanism for abstraction of two H atoms.

It was found that all persulfoxide/hydroperoxide complexes formed in trajectories did not decay back to the reactants before the termination of the trajectories (typically 2 – 3 ps). This suggests that the lifetime of the complex is at least no less than the trajectory time. For comparison, the classical rotational period of a complex estimated using the average angular momentum is 2.9 ps at $E_{\mathrm{col}} = 0.2$ eV. The fly-by time, taken as the time required for 5 Å motion at the relative speed of reactants, is 0.4 ps at $E_{\mathrm{col}} = 0.2$ eV. The fly-by time gives a measure of how long a direct collision would last at the same collision energy. Clearly, the complex lifetime is significantly longer than the fly-by time, and comparable to the complex rotational period. Note that the quasi-classical trajectory method used is not applicable to nonadiabatic collisions, *i.e.*, it does not allow transitions from a singlet to a triplet state. Therefore, trajectories cannot reproduce the "spin-forbidden" dissociative excitation transfer. But trajectories provide information concerning the early time dynamics where the electron spin of the reactants remains conserved, and more importantly, confirming the complex mediation in the reaction.

Finally, two H2T trajectories are illustrated in Figure 6.6. The r(C^{α}-H), r(N-H) and two r(O-H) plotted in the figure correspond to the C^{α}-H and N-H bonds being broken in $HSCH_2C^{\alpha}H(NH_2)CO_2^-$, and the two new O-H bonds being formed in the product H_2O_2. Figure 6.6a shows a concerted H2T trajectory, where the C^{α}-H and N-H bonds break simultaneously and the two new O-H bonds form at the same time. Figure 6.6b shows a sequential H2T trajectory, where the first H atom is transferred from C^{α} to O_2 and around 100 fs later the second H is transferred from N to O_2. These two trajectories together demonstrate the partial concerted nature of the H2T mechanism proposed in Figure 6.3. For both H2T trajectories, the reactants have repeated encounters after their initial collisions and remain close to each other. Actual abstraction of two H atoms occurs around

500 to 1,500 fs after initial collisions. This implies that a complex-mediated mechanism is necessary for H2T, as described in the H2T reaction coordinate (see Figure 6.3).

Note that H2T reactions are only observed in trajectories where the collision geometry allows simultaneous rupture of C^{α}-H and N-H bonds in the backbone of cysteine while forming the two O-H bonds in H_2O_2. Such a complicated process could occur only in collisions with "O_2 in parallel to the two H atoms being abstracted", *i.e.*, O_2 in close proximity and in parallel to $C^{\alpha}H^{*}$-NH^{*}. This restricted confinement may explain that few collisions could ultimately lead to H2T. On the other hand, the thiol group of cysteine locates at the end of the molecule, leaving more space for O_2 attack. This rationalizes that the trajectory calculated probability for complex-forming reaction is a factor of 5 higher than that of H2T at $b = 0.1$ Å.

6.4 Conclusion

In the present study, guided-ion-beam tandem mass spectrometry was employed to determine the reaction products, cross sections and collision energy dependence for the reaction of carboxylate anion of deprotonated Cys with $O_2(a^1\Delta_g)$. DFT calculations were carried out to identify the reaction coordinate (including reactants, intermediate complexes, transition states, and products), investigate thermodynamics and energy barriers. Quasi-classical, direct dynamics trajectory simulations were performed for collisions at E_{col} of 0.2 eV and b of 0.1 Å. Trajectories demonstrate the importance of complex-mediated mechanism for this system, and reveal a number of interesting dynamics features including orientation dependence for various product channels and a partial concerted mechanism for abstraction of two H atoms from cysteine by $^1O_2$. By combining direct dynamics trajectory simulations and reaction coordinate modeling, the reaction mechanism for this complicated system is revealed. One interesting result is that the electronic excitation energy of $^1O_2$ can be used to drive the dissociation of deprotonated Cys, yielding major product ion of $NH_2CH_2CO_2^-$, and the dissociative excitation energy transfer has to be mediated by intermediate complexes.

It is interesting to note that at the early stage of the reaction, $HSCH_2CH(NH_2)CO_2^-$ + $^1O_2$ shows identical behavior as that of $CysH^+$ + $^1O_2$.[22] Both protonated and deprotonated Cys form precursor complexes upon collisions with $^1O_2$, and subsequently interconvert to covalently bound persulfoxide and hydroperoxide complexes. The dissociation of intermediate complex by excitation energy of $^1O_2$ accounts for the major product channel for both systems, albeit deprotonated Cys has slightly higher reaction efficiency with $^1O_2$ compared to its protonated analogue. Resemblances also exist between trajectories results calculated at the same E_{col} for these two systems, as both show the importance of complex-mediation for reactive collisions.

References

1 A. A. Frimer, *Singlet O_2, Vol I, Physical-Chemical Aspects.* (Boca Raton, FL: CRC Press, 1985).
2 A. A. Frimer, *Singlet O_2, Vol II, Reaction Modes and Products, Part 1* (Boca Raton, FL: CRC Press, 1985).
3 A. A. Frimer, *Singlet O_2, Vol III, Reaction Modes and Products, Part 2* (Boca Raton, FL: CRC Press, 1985).
4 A. A. Frimer, *Singlet O_2, Vol IV, Polymers and Biomolecules* (Boca Raton, FL: CRC Press, 1985).
5 P. R. Ogilby, *Chem. Soc. Rev.,* 2010, 39, 3181-3209.
6 C. S. Foote, *Science,* 1968, 162, 963-970.
7 M. J. Davies, *Biochem. Biophys. Res. Commun.,* 2003, 305, 761-770.
8 P. E. Morgan, R. T. Dean, and M. J. Davies, *Free Radical Biol. Med.,* 2004, 36, 484-496.
9 M. J. Davies, *Biochim. Biophys. Acta,* 2005, 1703, 93-109.
10 G. Palumbo, *Expert Opin. Drug Delivery,* 2007, 4, 131-148.
11 M. J. Davies, *Photochem. Photobiol. Sci.,* 2004, 3, 17-25.
12 E. M. K. Hedin, S. A. Patkar, J. Vind, A. Svendsen, K. Hult, and P. Berglund, *Can. J. Chem.,* 2002, 80, 529-539.
13 M. Gracanin, C. L. Hawkins, D. I. Pattison, and M. J. Davies, *Free Radical Biol. Med.,* 2009, 47, 92-102.
14 P. J. Hogg, *Trends Biochem. Sci.,* 2004, 28, 210-214.
15 P. H. Fishman, J. W. Kusiak, and J. M. Bailey, *Biochem.,* 1973, 12, 2540-2544.
16 G. Gennari, G. Cauzzo, and G. Jori, *Photochem. Photobiol.,* 1974, 20, 497-500.
17 S. Cannistraro, G. Jori, and A. van der Vorst, *Photochem. Photobiol.,* 1978, 27, 517-521.
18 R. C. Straight, and J. D. Spikes, 'Photosensitized oxidation of biomolecules', in *Singlet O_2*, ed. by Aryeh A. Frimer (Boca Raton, Florida: CRC Press, 1985), pp. 91-143.
19 W. Ando, and T. Takata, 'Photooxidation of sulfur compounds', in *Singlet O_2*, ed. by A. A. Frimer (Boca Raton: CRC Press, 1985), pp. 1-117.
20 M. Rougee, R. V. Bensasson, E. J. Land, and R. Pariente, *Photochem. Photobiol.,* 1988, 47, 485-489.
21 G. Z. Justo, F. A. Camargo, M. Haun, A. Faljoni-Alario, and N. Duran, *Physiol. Chem. Phys. Med. NMR,* 2000, 32, 145-154.
22 F. Liu, Y. Fang, Y. Chen, and J. Liu, *J. Phys. Chem. B,* 2011, 115, 9898-9909.
23 M. Yamashita, and J. B. Fenn, *J. Phys. Chem.,* 1984, 88, 4451-4459.
24 J. B. Fenn, M. Mann, C. K. Meng, S. F. Wong, and C. M. Whitehouse, *Science,* 1989, 246, 64-71.
25 D. Gerlich, 'Inhomogeneous RF fields: A versatile tool for the study of processes with slow ions', in *State-Selected and State-to-State Ion-Molecule Reaction Dynamics. Part I. Experiment*, ed. by C. Y. Ng and M. Baer (New York: John Wiley & Sons, Inc., 1992), pp. 1-176.
26 A. A. Viggiano, A. Midey, N. Eyet, V. M. Bierbaum, and J. Troe, *J. Chem. Phys.,* 2009, 131, 094303.
27 Y. Fang, and J. Liu, *J. Phys. Chem. A,* 2009, 113, 11250-11261.
28 Y. Fang, A. Bennett, and J. Liu, *Int. J. Mass Spectrom.,* 2010, 293, 12-22.
29 Y. Fang, A. Bennett, and J. Liu, *Phys. Chem. Chem. Phys.,* 2011, 13, 1466-1478.
30 Y. Fang, F. Liu, A. Bennett, S. Ara, and J. Liu, *J. Phys. Chem. B,* 2011, 115, 2671-2682.
31 F. Liu, Y. Fang, and J. Liu, *J. Phys. Chem. B,* 2012, to be submitted.

32 P. B. Armentrout, *J. Anal. At. Spectrom.,* 2004, 19, 571-580.

33 E. A. Ogryzlo, 'Gaseous Singlet Oxygen', in *Singlet Oxygen*, ed. by Harry H. Wasserman and Robert W. Murray (New York: Academic Press, Inc., 1979), pp. 35-58.

34 Y. V. Savin, L. V. Goryachev, Y. A. Adamenkov, T. V. Rakhimova, Y. A. Mankelevich, N. A. Popov, A. A. Adamenkov, V. V. Egorov, S. P. Ilyin, Y. V. Kolobyanin, E. A. Kudryashov, G. S. Rogozhnikov, and B. A. Vyskubenko, *J. Phys. D: Appl. Phys.,* 2004, 37, 3121-3128.

35 S. Popović, M. Rašković, S. P. Kuo, and L. Vušković, *J. Phys.: Conf. Ser.,* 2007, 86, 012013.

36 F. C. Fehsenfeld, K. M. Evenson, and H. P. Broida, *Rev. Sci. Instrum.,* 1965, 36, 294-298.

37 J. Troe, *Chem. Phys. Lett.,* 1985, 122, 425 -430.

38 F. Liu, Y. Fang, Y. Chen, and J. Liu, *J. Phys. Chem. B,* 2012, 116, 6369-6379.

39 W. J. Lafferty, A. M. Solodov, C. L. Lugez, and G. T. Fraser, *Appl. Opt.,* 1998, 37, 2264-2270.

40 M. J. Frisch, G. W. Trucks, H. B. Schlegel, G. E. Scuseria, M. A. Robb, J. R. Cheeseman, G. Scalmani, V. Barone, B. Mennucci, G. A. Petersson, H. Nakatsuji, M. Caricato, X. Li, H. P. Hratchian, A. F. Izmaylov, J. Bloino, G. Zheng, J. L. Sonnenberg, M. Hada, M. Ehara, K. Toyota, R. Fukuda, J. Hasegawa, M. Ishida, T. Nakajima, Y. Honda, O. Kitao, H. Nakai, T. Vreven, J. J. A. Montgomery, J. E. Peralta, F. Ogliaro, M. Bearpark, J. J. Heyd, E. Brothers, K. N. Kudin, V. N. Staroverov, T. Keith, R. Kobayashi, J. Normand, K. Raghavachari, A. Rendell, J. C. Burant, S. S. Iyengar, J. Tomasi, M. Cossi, N. Rega, J. M. Millam, M. Klene, J. E. Knox, J. B. Cross, V. Bakken, C. Adamo, J. Jaramillo, R. Gomperts, R. E. Stratmann, O. Yazyev, A. J. Austin, R. Cammi, C. Pomelli, J. W. Ochterski, R. L. Martin, K. Morokuma, V. G. Zakrzewski, G. A. Voth, P. Salvador, J. J. Dannenberg, S. Dapprich, A. D. Daniels, O. Farkas, J. B. Foresman, J. V. Ortiz, J. Cioslowski, and D. J. Fox, Gaussian 09, Rev. B. 01, Wallingford CT: Gaussian, Inc., 2009.

41 J. Zheng, I. M. Alecu, B. J. Lynch, Y. Zhao, and D. G. Truhlar, Database of Frequency Scale Factors for Electronic Model Chemistries, Version 2, http://comp.chem.umn.edu/freqscale/version2.htm, 2010.

42 W. L. Hase, K. Bolton, P. de Sainte Claire, R. J. Duchovic, X. Hu, A. Komornicki, G. Li, K. Lim, D. Lu, G. H. Peslherbe, K. Song, K. N. Swamy, S. R. Vande Linde, A. Varandas, H. Wang, and R. J. Wolf, VENUS99: A general chemical dynamics computer program, Lubbock, TX: Texas Tech Univeristy 1999.

43 V. Bakken, J. M. Millam, and H. B. Schlegel, *J. Chem. Phys.,* 1999, 111, 8773-8777.

44 G. B. Bacskay, *Chem. Phys.,* 1981, 61, 385-404.

45 A. R. Leach, *Molecular modeling: Principles and applications* (Harlow, England: Pearson, Prentice Hall, 2001).

46 L. Laaksonen, gOpenMol, Espoo, Finland: Center for Scientific Computing, 2005, p. available at www.csc.fi/gopenmol/.

47 R. A. J. O'Hair, J. H. Bowie, and S. Gronert, *Int. J. Mass Spectrom. Ion Proc.,* 1992, 117, 23-36.

48 H.-K. Woo, K.-C. Lau, X.-B. Wang, and L.-S. Wang, *J. Phys. Chem. A,* 2006, 110, 12603-12606.

49 C. M. Jones, M. Bernier, E. Carson, K. E. Colyer, R. Metz, A. Pawlow, E. D. Wischow, I. Webb, E. J. Andriole, and J. C. Poutsma, *Int. J. Mass Spectrom.,* 2007, 267, 54-62.

50 Z. Tian, A. Pawlow, J. C. Poutsma, and S. R. Kass, *J. Am. Chem. Soc.,* 2007, 129, 5403-5407.

51 P. Vollhardt, and N. Schore, *Organic Chemistry*. 6th edn. 1270 vols (New York: W. H. Freeman and Company, 2009).
52 J. Oomens, J. D. Steill, and B. Redlich, *J. Am. Chem. Soc.,* 2009, 131, 4310-4319.
53 Z. Tian, and S. R. Kass, *J. Am. Chem. Soc.,* 2008, 130, 10842-10843.
54 Z. Tian, X.-B. Wang, L.-S. Wang, and S. R. Kass, *J. Am. Chem. Soc.,* 2009, 131, 1174-1181.
55 M. Eckersley, J. H. Bowie, and R. N. Hayes, *Int. J. Mass Spectrom.,* 1989, 93, 199-213.
56 W. Kulik, and W. Heerma, *Biomed. Environ. Mass Spectrom.,* 1988, 15, 419-427.
57 K. M. Ervin, I. Anusiewicz, P. Skurski, J. Simons, and W. C. Lineberger, *J. Phys. Chem. A,* 2003, 107, 8521-8529.
58 A. Midey, I. Dotan, and A. A. Viggiano, *J. Phys. Chem. A,* 2008, 112, 3040-3045.
59 A. Midey, I. Dotan, J. V. Seeley, and A. A. Viggiano, *Int. J. Mass Spectrom.,* 2009, 280, 6-11.
60 J. Liu, B. Uselman, J. Boyle, and S. L. Anderson, *J. Chem. Phys.,* 2006, 125, 133115.
61 J. Liu, B. van Devener, and S. L. Anderson, *J. Chem. Phys.,* 2002, 116, 5530-5543.
62 J. Liu, B. van Devener, and S. L. Anderson, *J. Chem. Phys.,* 2002, 117, 8292-8307.

Appendices

Appendix A

Standard Operating Procedure for the vacuum system of our mass spectrometer

Figure A.1 Front panel of interlock system

A1. To pump down the mass spectrometer, follow these procedures.

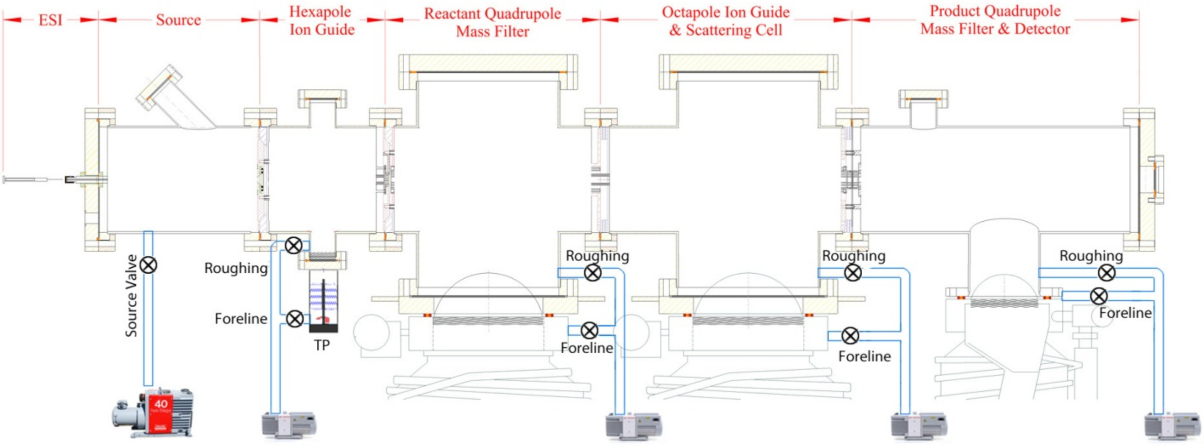

Figure A.2 Vacuum status of mass spectrometer – Off

- Make sure cooling water is on and its pressure is ≥ 35 psi.
- Make sure compressed air is on and its pressure is ≥ 80 psi.
- Make sure chamber vent valve is closed.
- Turn on *Safety Override*.
- Push *Start*.
- Turn on all 5 mechanical pumps (MPs). Wait until the mechanical pump line pressures drop below 30 mTorr, as indicated by five Granville-Phillips thermo pressure gauges.
- Turn on all 4 *Forelines*. Make sure the vent valve of the turbo pump is closed. Turn on *Turbo Pump* and all 3 *diffusion pumps* (DPs).
- Wait 1 hour for the DPs to heat up.

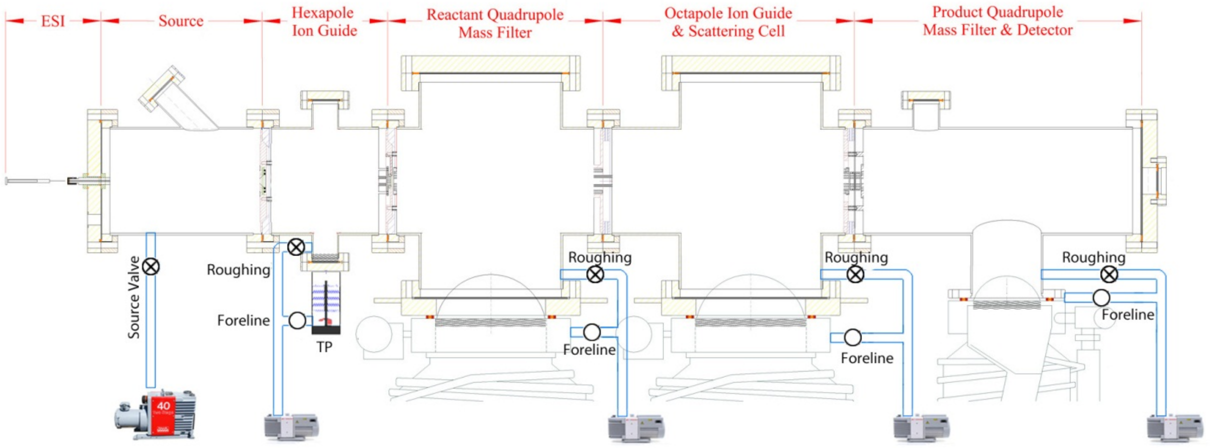

Figure A.3 Vacuum status of mass spectrometer – during heating up of DPs

- * Turn off all 4 *Forelines*. Turn on *Roughing* and *Source Valve* simultaneously to let MPs rough down the chambers to below 30 mTorr. Then open the valve between the Baratron capacitance manometer and chamber.

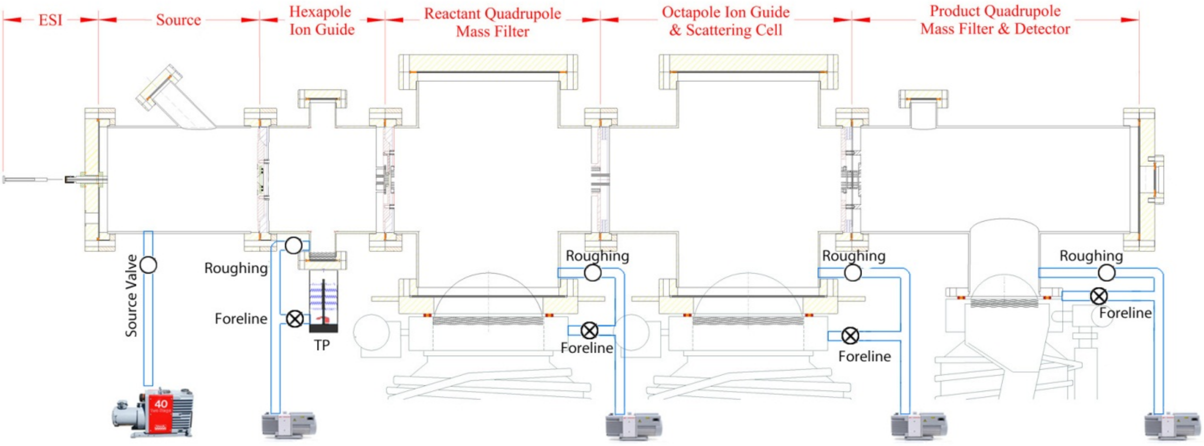

Figure A.4 Vacuum status of mass spectrometer – rough down the chambers using MPs

- Turn off *Roughing*, but leave *Source Valve* on.
- Turn on all 4 *Forelines* again.

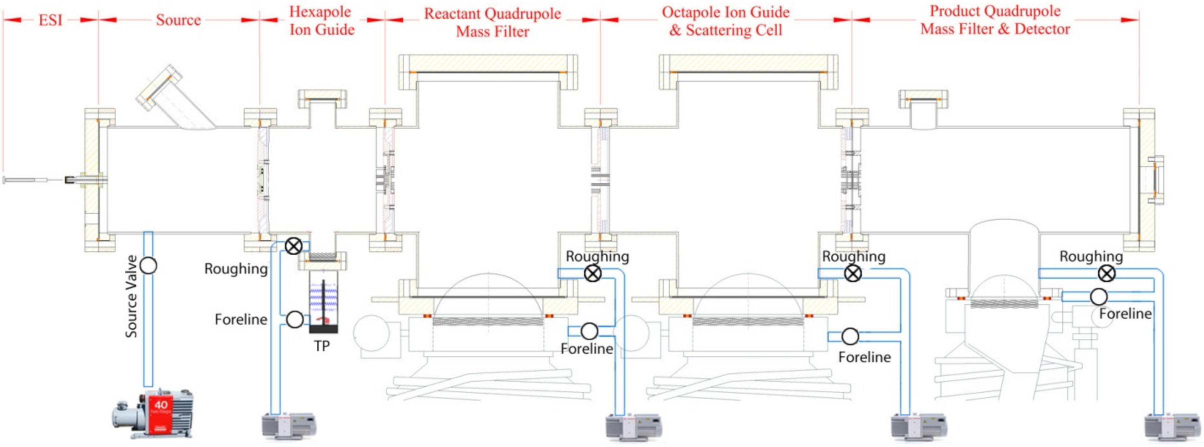

Figure A.5 Vacuum status of mass spectrometer – just before gates are open

- Make sure all foreline pressures are below 30 mTorr. Then turn on 4 *Gates*.
- Turn off *Safety Override*.
- Turn on all ion gauges and Baratron manometer controller.

- When the source chamber pressure drops below 50 mTorr, close the source valve and turn off MP1 during standby mode. The source chamber can be differentially pumped by the turbo pump through chamber #2, and maintains a pressure below 10 mTorr.
- Before experiments, turn on MP1 and the source valve.

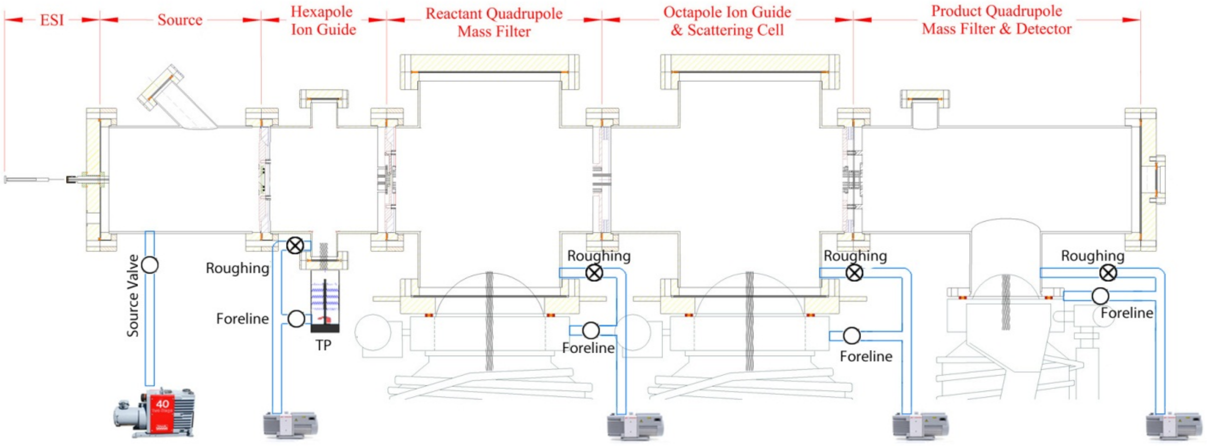

Figure A.6 Vacuum status of mass spectrometer – during experiments

Caution! Never operate the chamber vent valve during working condition.

A2. To shut down vacuum pumping system and vent the mass spectrometer, follow these procedures.

- Turn off all high voltage devices. Turn off *MS Power*.
- Turn off EyeSys gauge and 3 ion gauges.
- Close Baratron valve, and turn off Baratron manometer controller.
- Turn on *Safety Override*.
- Turn off all 4 *Gates*. Turn off *Source Valve*.

- Turn off *Turbo* and *Foreline* #2 simultaneously.

  Turn off all 3 *DPs*, but leave *Forelines #3/#4/#5* on.
- Wait 1 hour for DPs to cool down.
- Turn off *Forelines* 3/4/5 and all 5 *MPs*.
- Push *Kill* button.
- Turn off *Safety Override*.
- Open the vent valve located on top flange of chamber 4, vent the chambers with nitrogen gas.

In case alarm beeps, immediately turn off MS Power, all Gates and 3 ion gauges, and call supervisor.

In an emergency, push KILL button with no hesitation and call supervisor.

A3. In need of venting chambers without turning off pumps, follow these procedures.

- Turn off all ion gauges, Baratron valve and Baratron manometer controller.
- Check all high voltages are off. Turn off *MS Power*.
- Turn on *Safety Override*.
- Turn off all *Gates*.
- Turn off *Source Valve*.
- Vent the chamber with N_2.
- To pump down, start from the step marked with an asterisk in starting up procedure.

Appendix B

Standard experimental procedure of mass spectrometer

1. Turn on MP1 and open the source valve.
2. Turn off Ion Gauge 3, 4, 5.
3. Clean the nozzle to be used with anhydrous ethanol, and dry it with compressed air.
4. <u>Turn on Safety Override.</u> Replace entrance cap with the nozzle.

   Change set point 1 of convectron gauge #1 (-100 mTorr ➔ -3 Torr)

   and convectron gauge #2 (-30 mTorr ➔ -300 mTorr)

   <u>Turn off Safety Override.</u> The interlock system takes effect!
5. Turn on power supply of capillary heating wire.

   Turn on temperature meter and press MIN/MAX button to monitor the temperature continuously.
6. Turn on MS Power. Turn on MS Ctrl Boxes 1 & 2.

   Switch "Mass Command" to manual mode (i.e., downside) on the two MS Ctrl Boxes.

   Turn on both MS filter RF/DC power supplies, and warm up for 1 hour before experiments.
7. While warming up the MS RF/DC power supplies, prepare ESI sample solutions. Refill syringe with sample solution. Mount syringe to the syringe infusion pump, set the flow rate to 0.03 – 0.06 ml/h, then press RUN.
8. Wait the capillary temperature rises to ~150 ℃.
9. Replace the ESI needle in position. The distance between needle and nozzle is 0.5 – 1.0 cm.

   Turn on monitor, camera, and luminator for monitoring ESI (~50% lumens).

   Turn on ESI high voltage. **Gradually** tune up high voltage (2 – 3 kV) to obtain a stable electrospray.

If ESI spray is unstable, turn ESI high voltage off, and replace a new ESI needle/sleeve.

10. Turn on Hex RF oscillator, Hex HV, Oct RF oscillator, Oct HV, Rack Power for all electronic optical lenses, Detector HV & Deflector.
11. Run LabVIEW program (MassScan.vi or IMR.vi), and toggle “mass command” switches on the MS Ctrl Boxes to computer mode (i.e. upper side).
12. Perform experiments.

Appendix C

Chemicals and gases

Name	Molar mass (g•mol^{-1})	Purity	Manufacturer
L-arginine	174.2	>98.5%	Sigma Aldrich
L-aspartic acid	133.1	>99%	Sigma Aldrich
L-cysteine	121.2	100.1%	EMD Chemicals
L-cysteine hydrochloride	157.7	≥99.0%	Fluka
Dioctyl sodium sulfosuccinate (NaAOT, $C_{20}H_{37}NaO_7S$)	444.56	>99.0%	Fluka
Glycine	75.1	≥99%	Sigma Aldrich
Anhydrous hexane	86.2	95%	Sigma-Aldrich
Methanol	32.0	HPLC grade	Fisher Chemicals
β-naphthol	144.2	99%	Sigma Aldrich
Phenol	94.1	99%	Alfa Aesar
Phloretic acid	166.2	98%	Sigma Aldrich
L-proline	115.1	≥99.5%	Sigma Aldrich
Sodium hydroxide	40.0	>97%	Fisher Chemicals
L-tryptophan	204.2	99%	Sigma Aldrich
L-tyrosine	181.2	≥99%	Sigma Aldrich
Water	18.0	HPLC grade	Fisher Chemicals
Argon gas	39.9	99.99%	T. W. Smith
Oxygen gas	16.0	99.99%	T. W. Smith
Xenon gas	131.3	99.995%	Spectra Gases

BIBLIOGRAPHY

References for chapter 1

1 D. Gerlich, 'Inhomogeneous RF fields: A versatile tool for the study of processes with slow ions', in *State-Selected and State-to-State Ion-Molecule Reaction Dynamics. Part I. Experiment*, ed. by C. Y. Ng and M. Baer (New York: John Wiley & Sons, Inc., 1992), pp. 1-176.

2 P. Kebarle, and L. Tang, *Analytical Chemistry,* 1993, 65, 972A-986A.

3 J. S. Klassen, Y. Ho, A. T. Blades, and P. Kebarle, *Adv. Gas-Phase Ion Chem.,* 1998, 3, 255-318.

4 R. M. Moision, and P. B. Armentrout, *J. Am. Soc. Mass Spectrom. ,* 2007, 18, 1124-1134.

5 S. K. Chowdhury, V. Katta, and B. T. Chait, *Rapid Commun. Mass Spectrom.,* 1990, 4, 81-87.

6 T. Kim, K. Tang, H. R. Udseth, and R. D. Smith, *Anal. Chem.,* 2001, 73, 4162-4170.

7 K. Tang, A. V. Tolmachev, E. Nikolaev, R. Zhang, M. E. Belov, H. R. Udseth, and R. D. Smith, *Anal. Chem.,* 2002, 74, 5431-5437.

8 R. M. Jones, and S. L. Anderson, *Rev. Sci. Instru.,* 2000, 71, 4335-4337.

9 D. J. Douglas, and J. B. French, *J. Am. Mass Spectrom.,* 1992, 3, 398-408.

10 A. N. Krutchinsky, I. V. Chernushevich, V. L. Spicer, W. Ens, and K. G. Standing, *J. Am. Soc. Mass Spectrom.,* 1998, 9, 569-579.

11 'Manual for 150-QC quadrupole power supply', ABB Extrel, 1997).

12 K. M. Ervin, and P. B. Armentrout, *J. Chem. Phys.,* 1985, 83, 166-189.

13 'DeTech Inc. Technical Notes', <http://www.detechinc.com/technotes.html> [Accessed 10.3 2012].

14 *Basic Vacuum Practice*. 3rd ednVarian Associates, Inc., 1992).

15 Y.-H. Chiu, H. Fu, J.-T. Huang, and S. L. Anderson, *J. Chem. Phys.,* 1995, 102, 1199 - 1216.

16 R. M. Moision, and P. B. Armentrout, *J. Phys. Chem. A,* 2006, 110, 3933-3946.

17 J. Liu, B. Van Devener, and S. L. Anderson, *J. Chem. Phys.,* 2002, 116, 5530-5543.

18 P. B. Armentrout, *Int. J. Mass Spectrom.,* 2000, 200, 219-241.

19 M. B. Sowa-Resat, P. A. Hintz, and S. L. Anderson, *J. Phys. Chem.,* 1995, 99, 10736-10741.

20 R. D. Levine, and R. B. Bernstein, *Molecular Reaction Dynamics and Chemical Reactivity* (New York: Oxford University Press, 1987).

21 J. B. Foresman, and A. Frisch, *Exploring Chemistry with Electronic Structure Methods.* 2nd edn (Pittsburgh, PA: Gaussian, Inc, 2000).

22 M. T. Rodgers, K. M. Ervin, and P. B. Armentrout, *J. Chem. Phys.,* 1997, 106, 4499-4508.

23 L. Zhu, and W. L. Hase, 'A General RRKM Program(QCPE 644), Quantum Chemistry Program Exchange', (Bloomington: Chemistry Department, University of Indiana, 1993).

References for chapter 2

1 National Instruments, 2012 <http://www.ni.com/>.

2 NI M-series DAQmx manual , National Instruments, <http://www.ni.com/pdf/manuals/371022k.pdf>.

3 Manual for 150-QC quadrupole power supply, ABB Extrel, 1997.

References for chapter 3

1 P. L. Luisi, M. Giomini, M. P. Pileni, and B. H. Robinson, *Biochim. Biophys. Acta,* 1988, 947, 209-246.

2 K. Kon-no, *Surface Colloid Sci.,* 1993, 15, 125-151.

3 M.-P. Pileni, *Natural Materials,* 2003, 2, 145-150.

4 Y. Fang, A. Bennett, and J. Liu, *Int. J. Mass Spectrom.,* 2010, 293, 12-22.

5 Y. Fang, A. Bennett, and J. Liu, *Phys. Chem. Chem. Phys.,* 2011, 13, 1466-1478.

6 D. Bongiorno, L. Ceraulo, A. Ruggirello, V. T. Liveri, E. Basso, R. Seraglia, and P. Traldi, *J. Mass Spectrom.,* 2005, 40, 1618-1625.

7 G. Giorgi, L. Ceraulo, and V. T. Liveri, *J. Phys. Chem. B,* 2008, 112, 1376-1382.

8 G. Giorgi, E. Giocaliere, L. Ceraulo, A. Ruggirello, and V. T. Liveri, *Rapid Comm. Mass Spectrom.,* 2009, 23, 2206-2212.

9 G. Giorgi, L. Ceraulo, G. Berden, J. Oomens, and V. T. Liveri, *J. Phys. Chem. B,* 2011, 115, 2282-2286.

10 D. Bongiorno, L. Ceraulo, G. Giorgi, S. Indelicato, and V. T. Liveri, *J. Mass. Spectrom.,* 2011, 46, 1263-1268.

11 L. Ceraulo, G. Giorgi, V. T. Liveri, D. Bongiorno, S. Indelicato, F. Di Gaudio, and S. Indelicato, *European Journal of Mass Spectrometry,* 2011, 17, 525-541.

12 S. A. Burns, P. L. Valint, Jr., and J. A. Gardella, Jr., *Langmuir,* 2009, 25, 11244-11249.

13 A. I. Bulavchenko, A. F. Batishchev, E. K. Batishcheva, and V. G. Torgov, *J. Phys. Chem. B,* 2002, 106, 6381-6389.

14 G. Longhi, S. L. Fornili, V. T. Liveri, S. Abbate, D. Rebeccani, L. Ceraulоe, and F. Gangem, *Phys. Chem. Chem. Phys.,* 2010, 12, 4694-4703.

15 G. Longhi, S. Abbate, L. Ceraulo, A. Ceselli, S. L. Fornili, and V. T. Liveri, *Phys. Chem. Chem. Phys.,* 2011, 13, 21423-21431.

16 N. P. Barrera, N. D. Bartolo, P. J. Booth, and C. V. Robinson1, *Science,* 2008, 321, 243-246.

17 R. Allen, S. Bandyopadhyay, and M. L. Klein, *Langmuir,* 2000, 16, 10547-10552.

18 R. Neutze, R. Wouts, D. v. d. Spoe, E. Weckert, and J. Hajdu, *Nature,* 2000, 406, 752-757.

19 K. Mukherjee, S. P. Moulik, and D. C. Mukherjee, *Langmuir,* 1993, 9, 1727-1730.

20 J. F. D. L. Mora, *J. Fluid Mech.,* 1992, 243, 561-574.

21 J. S. Klassen, Y. Ho, A. T. Blades, and P. Kebarle, *Adv. Gas-Phase Ion Chem.,* 1998, 3, 255-318.

22 P. Kebarle, *J. Mass Spectrom.,* 2000, 35, 804-817.

23 S. E. Rodriguez-Cruz, J. T. Khoury, and J. H. Parks, *J. Am. Soc. Mass Spectrom.,* 2001, 12, 716-725.

24 R. M. Moision, and P. B. Armentrout, *J. Am. Soc. Mass Spectrom. ,* 2007, 18, 1124-1134.

25 A. N. Krutchinsky, I. V. Chernushevich, V. L. Spicer, W. Ens, and K. G. Standing, *J. Am. Soc. Mass Spectrom.,* 1998, 9, 569-579.

26 D. J. Douglas, and J. B. French, *J. Am. Mass Spectrom.,* 1992, 3, 398-408.

27 S. A. McLuckey, G. L. Glish, and G. J. V. Berkel, *Anal. Chem.,* 1991, 63, 1971-1978.

28 J. James L. Stephenson, and S. A. McLuckey, *Anal. Chem.,* 1998, 70, 3533-3544.

29 D. Gerlich, 'Inhomogeneous RF fields: A versatile tool for the study of processes with slow ions', in *State-Selected and State-to-State Ion-Molecule Reaction Dynamics. Part I. Experiment*, ed. by C. Y. Ng and M. Baer (New York: John Wiley & Sons, Inc., 1992), pp. 1-176.

30 G. Wang, and R. B. Cole, 'Solution, gas-phase, and instrumental parameter influences on charge-state distributions in electrospray ionization mass spectrometry', in *Electrospray Ionization Mass Spectrometry: Fundamentals, Instrumentation, and Applications*, ed. by Richard B. Cole (New York: John Wiley & Sons, Inc, 1997), pp. 137-174.

31 M. Ueda, and Z. A. Schelly, *J. Colloid Interface Sci.,* 1988, 124, 673-676.

32 M. Ueda, and Z. A. Schelly, *Langmuir,* 1988, 4, 653-655.

33 M. E. Leser, and P. L. Luisi, *Chimia,* 1990, 44, 270-282.

34 A. M. Maitra, and P. K. Patanjali, in *Surfactants in Solution*, ed. by K. L. Mittal and P. Bothorel (New York: Plenum Press, 1986), p. 581.

35 R. M. Lemert, R. A. Fuller, and K. P. Johnston, *J. Phys. Chem.,* 1990, 94, 6021-6028.

36 R. M. Moision, and P. B. Armentrout, *J. Phys. Chem. A,* 2002, 106, 10350-10351-10362.

37 S. J. Ye, R. M. Moision, and P. B. Armentrout, *Int. J. Mass Spectrom.,* 2005, 240, 233-248.

38 J. Liu, B. Van Devener, and S. L. Anderson, *J. Chem. Phys.,* 2002, 116, 5530-5543.

39 J. Faeder, and B. M. Ladanyi, *J. Phys. Chem. B,* 2000, 104, 1033-1046.

40 J. Chowdhary, and B. M. Ladanyi, *J. Phys. Chem. B,* 2009, 113, 15029-15039.

41 M. J. Frisch, G. W. Trucks, H. B. Schlegel, G. E. Scuseria, M. A. Robb, J. R. Cheeseman, J. J. A. Montgomery, T. Vreven, K. N. Kudin, J. C. Burant, J. M. Millam, S. S. Iyengar, J. Tomasi, V. Barone, B. Mennucci, M. Cossi, G. Scalmani, N. Rega, G. A. Petersson, H. Nakatsuji, M. Hada, M. Ehara, K. Toyota, R. Fukuda, J. Hasegawa, M. Ishida, T. Nakajima, Y. Honda, O. Kitao, H. Nakai, M. Klene, X. Li, J. E. Knox, H. P. Hratchian, J. B. Cross, V. Bakken, C. Adamo, J. Jaramillo, R. Gomperts, R. E. Stratmann, O. Yazyev, A. J. Austin, R. Cammi, C. Pomelli, J. W. Ochterski, P. Y. Ayala, K. Morokuma, G. A. Voth, P. Salvador, J. J. Dannenberg, V. G. Zakrzewski, S. Dapprich, A. D. Daniels, M. C. Strain, O. Farkas, D. K. Malick, A. D. Rabuck, K. Raghavachari, J. B. Foresman, J. V. Ortiz, Q. Cui, A. G. Baboul, S. Clifford, J. Cioslowski, B. B. Stefanov, G. Liu, A. Liashenko, P. Piskorz, I. Komaromi, R. L. Martin, D. J. Fox, T. Keith, M. A. Al-Laham, C. Y. Peng, A. Nanayakkara, M. Challacombe, P. M. W. Gill, B. Johnson, W. Chen, M. W. Wong, C. Gonzalez, and J. A. Pople, Gaussian 03, Rev. E.01, Wallingford CT: Gaussian, Inc, 2004.

42 M. Wong, J. K. Thomas, and T. Nowak, *J. Am. Chem. Soc.,* 1977, 99, 4730-4736.

43 H.-S. Tan, I. R. Piletic, and M. D. Fayer, *J. Chem. Phys.,* 2005, 122, 174501.

44 M. R. Harpham, B. M. Ladanyi, and N. E. Levinger, *J. Phys. Chem. B,* 2005, 109, 16891-16900.

45 P. A. Pieniazek, Y.-S. Lin, J. Chowdhary, B. M. Ladanyi, and J. L. Skinner, *J. Phys. Chem. B,* 2009, 113, 15017-15028.

46 Y. Wang, D. S. D. Larsson, and D. v. d. Spoel, *Biochem.,* 2009, 48, 1006-1015.

47 M. Sharon, L. L. Ilag, and C. V. Robinson, *J. Am. Chem. Soc.,* 2007, 129, 8740-8746.

48 S.-W. Lee, P. Freivogel, T. Schindler, and J. L. Beauchamp, *JACS,* 1998, 120, 11758-11765.
49 W. D. V. Horn, A. K. Simorellis, and P. F. Flynn, *J. Am. Chem. Soc.,* 2005, 127, 13553-13660.
50 A. K. Simorellis, W. D. V. Horn, and P. F. Flynn, *J. Am. Chem. Soc.,* 2006, 128, 5082-5090.
51 A. D'Aprano, A. Lizzio, and V. T. Liveri, *J. Phys. Chem.,* 1987, 91, 4749-4751.
52 S. P. Moulik, and S. Ray, *Pure Appl. Chem.,* 1994, 66, 521-525.

References for chapter 4

1 E. B. Leodidis, and T. A. Hatton, *J. Phys. Chem.,* 1990, 94, 6400-6411.
2 E. B. Leodidis, and T. A. Hatton, *J. Phys. Chem.,* 1990, 94, 6411-6420.
3 E. B. Leodidis, A. S. Bommarius, and T. A. Hatton, *J. Phys. Chem. ,* 1991, 95, 5943-5956.
4 E. B. Leodidis, and T. A. Hatton, *J. Phys. Chem.,* 1991, 95, 5957-5965.
5 E. B. Leodidis, and T. A. Hatton, *J. Colloid Interface Sci.,* 1991, 147, 163-177.
6 R. M. Lemert, R. A. Fuller, and K. P. Johnston, *J. Phys. Chem.,* 1990, 94, 6021-6028.
7 M. Adachi, M. Harada, A. Shioi, and Y. Sato, *J. Phys. Chem.,* 1991, 95, 7925-7931.
8 M. M. Cardoso, M. J. Barradas, M. T. Carrondo, K. H. Kroner, and J. G. Crespo, *Bioseparation,* 1998, 7, 65-78.
9 M. M. Cardoso, M. J. Barradas, K. H. Kroner, and J. G. Crespo, *Journal of Chemical Technology and Biotechnology,* 1999, 74, 801-811.
10 X. Fu, J. Li, Y. Ma, L. Zhang, D. Wang, and Z. Hu, *Colloids and Surfaces A: Physicochemical and Engineering Aspects,* 2001, 179, 1-10.
11 R. Rinaldi, P. L. O. Volpe, and I. L. Torriani, *J. Colloid Interface Sci.,* 2008, 318, 59-67.
12 P. Vollhardt, and N. Schore, *Organic Chemistry*. 6th edn. 1270 vols (New York: W. H. Freeman and Company, 2009).
13 Y. Nozaki, and C. Tanford, *J. Bio. Chem.,* 1971, 246, 2211-2217.
14 W. C. Wimley, T. P. Creamer, and S. H. White, *Biochemistry,* 1996, 35, 5109-5124.
15 W. C. Wimley, and S. H. White, *Nature Structure Biology,* 1996, 3, 842-848.
16 K. Mukherjee, S. P. Moulik, and D. C. Mukherjee, *Langmuir,* 1993, 9, 1727-1730.
17 D. Bongiorno, L. Ceraulo, A. Ruggirello, V. T. Liveri, E. Basso, R. Seraglia, and P. Traldi, *J. Mass Spectrom.,* 2005, 40, 1618-1625.
18 Y. Fang, A. Bennett, and J. Liu, *Int. J. Mass Spectrom.,* 2010, 293, 12-22.
19 F. M. Menger, and G. Saito, *J. Am. Chem. Soc.,* 1978, 100, 4376-4379.
20 P. L. Luisi, M. Giomini, M. P. Pileni, and B. H. Robinson, *Biochim. Biophys. Acta,* 1988, 947, 209-246.
21 A. M. Maitra, and P. K. Patanjali, in *Surfactants in Solution*, ed. by K. L. Mittal and P. Bothorel (New York: Plenum Press, 1986), p. 581.
22 L. J. Magld, K. Kon-no, and C. A. Martin, *J. Phys. Chem.,* 1981, 85, 1434-1439.
23 E. Bardez, E. Monnier, and B. Valeur, *J. Phys. Chem.,* 1985, 89, 5031-5036.
24 R. M. Moision, and P. B. Armentrout, *J. Phys. Chem. A,* 2002, 106, 10350-10351-10362.
25 S. J. Ye, R. M. Moision, and P. B. Armentrout, *Int. J. Mass Spectrom.,* 2005, 240, 233-248.
26 M. J. Locke, and R. T. McIver, Jr. , *J. Am. Chem. Soc.,* 1983, 105, 4226-4232.
27 J. Faeder, and B. M. Ladanyi, *J. Phys. Chem. B,* 2005, 109, 6732-6740.

28 M. Hebrant, and C. Tondre, *Analytical Sciences,* 1998, 14, 109-115.

References for chapter 5

1 K. Mukherjee, S. P. Moulik, and D. C. Mukherjee, *Langmuir,* 1993, 9, 1727-1730.
2 P. L. Luisi, M. Giomini, M. P. Pileni, and B. H. Robinson, *Biochim. Biophys. Acta,* 1988, 947, 209-246.
3 R. W. Gale, J. L. Fulton, and R. D. Smith, *J. Am. Chem. Soc.,* 1987, 109, 920-921.
4 M.-P. Pileni, *Natural Materials,* 2003, 2, 145-150.
5 E. F. Williams, N. T. Woodbery, and J. K. Dixon, *J. Colloid Interface Sci.,* 1957, 12, 452-459.
6 P. Mukerjee, and K. J. Mysels, *Critical Micelle Concentration of Aqueous Surfactant Systems* (Washington, DC: NSRDC-NBS 36, 1971).
7 Y. Fang, A. Bennett, and J. Liu, *Int. J. Mass Spectrom.,* 2010, 293, 12-22.
8 Y. Fang, F. Liu, and J. Liu, *Journal of The American Society for Mass Spectrometry,* 2012, submitted.
9 D. Bongiorno, L. Ceraulo, G. Giorgi, S. Indelicato, and V. T. Liveri, *J. Mass. Spectrom.,* 2011, 46, 1263-1268.
10 D. Bongiorno, L. Ceraulo, A. Ruggirello, V. T. Liveri, E. Basso, R. Seraglia, and P. Traldi, *J. Mass Spectrom.,* 2005, 40, 1618-1625.
11 G. Giorgi, E. Giocaliere, L. Ceraulo, A. Ruggirello, and V. T. Liveri, *Rapid Comm. Mass Spectrom.,* 2009, 23, 2206-2212.
12 L. Ceraulo, G. Giorgi, V. T. Liveri, D. Bongiorno, S. Indelicato, F. Di Gaudio, and S. Indelicato, *European Journal of Mass Spectrometry,* 2011, 17, 525-541.
13 G. Giorgi, I. Pini, L. Ceraulo, and V. T. Liveri, *J. Mass Spectrom.,* 2011, 46, 925-932.
14 Y. Nozaki, and C. Tanford, *J. Bio. Chem.,* 1971, 246, 2211-2217.
15 W. C. Wimley, and S. H. White, *Nature Structure Biology,* 1996, 3, 842-848.
16 E. B. Leodidis, and T. A. Hatton, *J. Phys. Chem.,* 1990, 94, 6400-6411.
17 E. B. Leodidis, and T. A. Hatton, *J. Phys. Chem.,* 1990, 94, 6411-6420.
18 E. B. Leodidis, A. S. Bommarius, and T. A. Hatton, *J. Phys. Chem. ,* 1991, 95, 5943-5956.
19 E. B. Leodidis, and T. A. Hatton, *J. Phys. Chem.,* 1991, 95, 5957-5965.
20 P. Vollhardt, and N. Schore, *Organic Chemistry.* 6th edn. 1270 vols (New York: W. H. Freeman and Company, 2009).
21 Y. Fang, A. Bennett, and J. Liu, *Phys. Chem. Chem. Phys.,* 2011, 13, 1466-1478.
22 D. J. Donaldson, A. F. Tuck, and V. Vaida, *Phys. Chem. Chem. Phys.,* 2001, 3, 5270-5273.
23 D. Bongiorno, L. Ceraulo, G. Giorgi, S. Indelicato, M. Ferrugia, A. Ruggirello, and V. T. Liveri, *J. Mass Spectrom.,* 2011, 46, 195-201.
24 G. Longhi, S. L. Fornili, V. T. Liveri, S. Abbate, D. Rebeccani, L. Cerauloe, and F. Gangem, *Phys. Chem. Chem. Phys.,* 2010, 12, 4694-4703.
25 A. I. Bulavchenko, A. F. Batishchev, E. K. Batishcheva, and V. G. Torgov, *J. Phys. Chem. B,* 2002, 106, 6381-6389.
26 J. Faeder, and B. M. Ladanyi, *J. Phys. Chem. B,* 2000, 104, 1033-1046.
27 J. Chowdhary, and B. M. Ladanyi, *J. Phys. Chem. B,* 2009, 113, 15029-15039.
28 M. Sharon, L. L. Ilag, and C. V. Robinson, *J. Am. Chem. Soc.,* 2007, 129, 8740-8746.
29 G. Siuzdak, and B. Bothner, *Angew. Chem. Int. Ed.,* 1995, 34, 2053-2055.

30 F. Cacace, G. de Petris, E. Giglio, F. Punzo, and A. Troiani, *Chem. Eur. J.,* 2002, 8, 1925-1933.
31 D. Nohara, and M. Bitoh, *J. Mass Spectrom.,* 2000, 35, 1434-1437.
32 J. P. Wilcoxon, and P. P. Provencio, *J. Phys. Chem. B,* 1999, 103, 9809-9812.

References for chapter 6

1 A. A. Frimer, *Singlet O_2, Vol I, Physical-Chemical Aspects.* (Boca Raton, FL: CRC Press, 1985).
2 A. A. Frimer, *Singlet O_2, Vol II, Reaction Modes and Products, Part 1* (Boca Raton, FL: CRC Press, 1985).
3 A. A. Frimer, *Singlet O_2, Vol III, Reaction Modes and Products, Part 2* (Boca Raton, FL: CRC Press, 1985).
4 A. A. Frimer, *Singlet O_2, Vol IV, Polymers and Biomolecules* (Boca Raton, FL: CRC Press, 1985).
5 P. R. Ogilby, *Chem. Soc. Rev.,* 2010, 39, 3181-3209.
6 C. S. Foote, *Science,* 1968, 162, 963-970.
7 M. J. Davies, *Biochem. Biophys. Res. Commun.,* 2003, 305, 761-770.
8 P. E. Morgan, R. T. Dean, and M. J. Davies, *Free Radical Biol. Med.,* 2004, 36, 484-496.
9 M. J. Davies, *Biochim. Biophys. Acta,* 2005, 1703, 93-109.
10 G. Palumbo, *Expert Opin. Drug Delivery,* 2007, 4, 131-148.
11 M. J. Davies, *Photochem. Photobiol. Sci.,* 2004, 3, 17-25.
12 E. M. K. Hedin, S. A. Patkar, J. Vind, A. Svendsen, K. Hult, and P. Berglund, *Can. J. Chem.,* 2002, 80, 529-539.
13 M. Gracanin, C. L. Hawkins, D. I. Pattison, and M. J. Davies, *Free Radical Biol. Med.,* 2009, 47, 92-102.
14 P. J. Hogg, *Trends Biochem. Sci.,* 2004, 28, 210-214.
15 P. H. Fishman, J. W. Kusiak, and J. M. Bailey, *Biochem.,* 1973, 12, 2540-2544.
16 G. Gennari, G. Cauzzo, and G. Jori, *Photochem. Photobiol.,* 1974, 20, 497-500.
17 S. Cannistraro, G. Jori, and A. van der Vorst, *Photochem. Photobiol.,* 1978, 27, 517-521.
18 R. C. Straight, and J. D. Spikes, 'Photosensitized oxidation of biomolecules', in *Singlet O_2*, ed. by Aryeh A. Frimer (Boca Raton, Florida: CRC Press, 1985), pp. 91-143.
19 W. Ando, and T. Takata, 'Photooxidation of sulfur compounds', in *Singlet O_2*, ed. by A. A. Frimer (Boca Raton: CRC Press, 1985), pp. 1-117.
20 M. Rougee, R. V. Bensasson, E. J. Land, and R. Pariente, *Photochem. Photobiol.,* 1988, 47, 485-489.
21 G. Z. Justo, F. A. Camargo, M. Haun, A. Faljoni-Alario, and N. Duran, *Physiol. Chem. Phys. Med. NMR,* 2000, 32, 145-154.
22 F. Liu, Y. Fang, Y. Chen, and J. Liu, *J. Phys. Chem. B,* 2011, 115, 9898-9909.
23 M. Yamashita, and J. B. Fenn, *J. Phys. Chem.,* 1984, 88, 4451-4459.
24 J. B. Fenn, M. Mann, C. K. Meng, S. F. Wong, and C. M. Whitehouse, *Science,* 1989, 246, 64-71.
25 D. Gerlich, 'Inhomogeneous RF fields: A versatile tool for the study of processes with slow ions', in *State-Selected and State-to-State Ion-Molecule Reaction Dynamics. Part I. Experiment*, ed. by C. Y. Ng and M. Baer (New York: John Wiley & Sons, Inc., 1992), pp. 1-176.

26 A. A. Viggiano, A. Midey, N. Eyet, V. M. Bierbaum, and J. Troe, *J. Chem. Phys.,* 2009, 131, 094303.
27 Y. Fang, and J. Liu, *J. Phys. Chem. A,* 2009, 113, 11250-11261.
28 Y. Fang, A. Bennett, and J. Liu, *Int. J. Mass Spectrom.,* 2010, 293, 12-22.
29 Y. Fang, A. Bennett, and J. Liu, *Phys. Chem. Chem. Phys.,* 2011, 13, 1466-1478.
30 Y. Fang, F. Liu, A. Bennett, S. Ara, and J. Liu, *J. Phys. Chem. B,* 2011, 115, 2671-2682.
31 F. Liu, Y. Fang, and J. Liu, *J. Phys. Chem. B,* 2012, to be submitted.
32 P. B. Armentrout, *J. Anal. At. Spectrom.,* 2004, 19, 571-580.
33 E. A. Ogryzlo, 'Gaseous Singlet Oxygen', in *Singlet Oxygen*, ed. by Harry H. Wasserman and Robert W. Murray (New York: Academic Press, Inc., 1979), pp. 35-58.
34 Y. V. Savin, L. V. Goryachev, Y. A. Adamenkov, T. V. Rakhimova, Y. A. Mankelevich, N. A. Popov, A. A. Adamenkov, V. V. Egorov, S. P. Ilyin, Y. V. Kolobyanin, E. A. Kudryashov, G. S. Rogozhnikov, and B. A. Vyskubenko, *J. Phys. D: Appl. Phys.,* 2004, 37, 3121-3128.
35 S. Popović, M. Rašković, S. P. Kuo, and L. Vušković, *J. Phys.: Conf. Ser.,* 2007, 86, 012013.
36 F. C. Fehsenfeld, K. M. Evenson, and H. P. Broida, *Rev. Sci. Instrum.,* 1965, 36, 294-298.
37 J. Troe, *Chem. Phys. Lett.,* 1985, 122, 425 -430.
38 F. Liu, Y. Fang, Y. Chen, and J. Liu, *J. Phys. Chem. B,* 2012, 116, 6369-6379.
39 W. J. Lafferty, A. M. Solodov, C. L. Lugez, and G. T. Fraser, *Appl. Opt.,* 1998, 37, 2264-2270.
40 M. J. Frisch, G. W. Trucks, H. B. Schlegel, G. E. Scuseria, M. A. Robb, J. R. Cheeseman, G. Scalmani, V. Barone, B. Mennucci, G. A. Petersson, H. Nakatsuji, M. Caricato, X. Li, H. P. Hratchian, A. F. Izmaylov, J. Bloino, G. Zheng, J. L. Sonnenberg, M. Hada, M. Ehara, K. Toyota, R. Fukuda, J. Hasegawa, M. Ishida, T. Nakajima, Y. Honda, O. Kitao, H. Nakai, T. Vreven, J. J. A. Montgomery, J. E. Peralta, F. Ogliaro, M. Bearpark, J. J. Heyd, E. Brothers, K. N. Kudin, V. N. Staroverov, T. Keith, R. Kobayashi, J. Normand, K. Raghavachari, A. Rendell, J. C. Burant, S. S. Iyengar, J. Tomasi, M. Cossi, N. Rega, J. M. Millam, M. Klene, J. E. Knox, J. B. Cross, V. Bakken, C. Adamo, J. Jaramillo, R. Gomperts, R. E. Stratmann, O. Yazyev, A. J. Austin, R. Cammi, C. Pomelli, J. W. Ochterski, R. L. Martin, K. Morokuma, V. G. Zakrzewski, G. A. Voth, P. Salvador, J. J. Dannenberg, S. Dapprich, A. D. Daniels, O. Farkas, J. B. Foresman, J. V. Ortiz, J. Cioslowski, and D. J. Fox, Gaussian 09, Rev. B. 01, Wallingford CT: Gaussian, Inc., 2009.
41 J. Zheng, I. M. Alecu, B. J. Lynch, Y. Zhao, and D. G. Truhlar, Database of Frequency Scale Factors for Electronic Model Chemistries, Version 2, http://comp.chem.umn.edu/freqscale/version2.htm, 2010.
42 W. L. Hase, K. Bolton, P. de Sainte Claire, R. J. Duchovic, X. Hu, A. Komornicki, G. Li, K. Lim, D. Lu, G. H. Peslherbe, K. Song, K. N. Swamy, S. R. Vande Linde, A. Varandas, H. Wang, and R. J. Wolf, VENUS99: A general chemical dynamics computer program, Lubbock, TX: Texas Tech Univeristy 1999.
43 V. Bakken, J. M. Millam, and H. B. Schlegel, *J. Chem. Phys.,* 1999, 111, 8773-8777.
44 G. B. Bacskay, *Chem. Phys.,* 1981, 61, 385-404.
45 A. R. Leach, *Molecular modeling: Principles and applications* (Harlow, England: Pearson, Prentice Hall, 2001).
46 L. Laaksonen, gOpenMol, Espoo, Finland: Center for Scientific Computing, 2005, p. available at www.csc.fi/gopenmol/.

47 R. A. J. O'Hair, J. H. Bowie, and S. Gronert, *Int. J. Mass Spectrom. Ion Proc.,* 1992, 117, 23-36.

48 H.-K. Woo, K.-C. Lau, X.-B. Wang, and L.-S. Wang, *J. Phys. Chem. A,* 2006, 110, 12603-12606.

49 C. M. Jones, M. Bernier, E. Carson, K. E. Colyer, R. Metz, A. Pawlow, E. D. Wischow, I. Webb, E. J. Andriole, and J. C. Poutsma, *Int. J. Mass Spectrom.,* 2007, 267, 54-62.

50 Z. Tian, A. Pawlow, J. C. Poutsma, and S. R. Kass, *J. Am. Chem. Soc.,* 2007, 129, 5403-5407.

51 P. Vollhardt, and N. Schore, *Organic Chemistry*. 6th edn. 1270 vols (New York: W. H. Freeman and Company, 2009).

52 J. Oomens, J. D. Steill, and B. Redlich, *J. Am. Chem. Soc.,* 2009, 131, 4310-4319.

53 Z. Tian, and S. R. Kass, *J. Am. Chem. Soc.,* 2008, 130, 10842-10843.

54 Z. Tian, X.-B. Wang, L.-S. Wang, and S. R. Kass, *J. Am. Chem. Soc.,* 2009, 131, 1174-1181.

55 M. Eckersley, J. H. Bowie, and R. N. Hayes, *Int. J. Mass Spectrom.,* 1989, 93, 199-213.

56 W. Kulik, and W. Heerma, *Biomed. Environ. Mass Spectrom.,* 1988, 15, 419-427.

57 K. M. Ervin, I. Anusiewicz, P. Skurski, J. Simons, and W. C. Lineberger, *J. Phys. Chem. A,* 2003, 107, 8521-8529.

58 A. Midey, I. Dotan, and A. A. Viggiano, *J. Phys. Chem. A,* 2008, 112, 3040-3045.

59 A. Midey, I. Dotan, J. V. Seeley, and A. A. Viggiano, *Int. J. Mass Spectrom.,* 2009, 280, 6-11.

60 J. Liu, B. Uselman, J. Boyle, and S. L. Anderson, *J. Chem. Phys.,* 2006, 125, 133115.

61 J. Liu, B. van Devener, and S. L. Anderson, *J. Chem. Phys.,* 2002, 116, 5530-5543.

62 J. Liu, B. van Devener, and S. L. Anderson, *J. Chem. Phys.,* 2002, 117, 8292-8307.